DISS. ETH NO. 25450

Garnet-based all Solid State Battery Design and Operation

A thesis submitted to attain the degree of
DOCTOR OF SCIENCES of ETH ZURICH
(Dr. sc. ETH Zurich)

presented by

RETO MAX PFENNINGER

MSc ETH Materials, ETH Zurich

born on 14.02.1989

citizen of Switzerland
place of origin: Hombrechtikon (ZH)

Accepted on the recommendation of:
Prof. Dr. Jennifer L.M. Rupp, examiner
Prof. Dr. Vanessa Wood, co-examiner
Dr. Kostiantyn Kravchyk, co-examiner

Zurich, 2018

Acknowledgements

MIT with Yuntong Zhu, Juan Carlos Gonzalez-Rosillo, Zachary Hood, Konjoong Kim, Philipp Simons, Priyanka Chaudhuri and particularly Thomas Defferriere, who was one of only few people in the US, who understood how swissness must feel. I wish you all the best for the exciting time to come! A special thanks to Julian Leonard and George de Bansa (aka "the Fungus") for the interesting discussions after work in cold and dark Boston.

Finally, everything I achieved so far in my life would not have been possible, without the great support of my family. All of my achievements are also yours and the endless support and love I got from Madeleine, Max and Grömi, have always been helping me in any situation I came across. My girlfriend Manuela always had a shoulder to lean on, whenever something was not working or I was desperate. You are always in my heart!

Finally, I would like to thank the committee of my thesis, Prof. Dr. Jennifer L.M. Rupp, Prof. Dr. Vanessa Wood, Dr. Kostiantyn Kravchyk and Prof. Dr. Ralph Spolenak for their valuable time and input in the evaluation of this thesis work.

Zürich, 2018

Summary

In the last years, all solid state batteries emerged from an increasing need for safe and high energy-dense storage systems. In the context of a growing demand for electric vehicles and all kinds of portable electronics, such as wearable microchips with sensing and measuring capabilities, soon the energy storage system was identified to bottleneck technological progress. Here, all solid state battery technology may address several key shortcomings, offering non-flammability, reduced packaging needs and potential compatibility with uncommon electrodes of high energy and power density.

The replacement of liquid or polymeric electrolytes, up to a point where no more carbon constituents are present, is highly desirable but – so far – broadly unexplored. The lack of experimental efforts towards all-ceramic battery architectures shall be addressed in the following thesis.

Specifically, the compatibility of lithium metal oxide anodes, in the form of thin films, have previously never been tested in combination with Li-garnet electrolytes. In a similar manner, it also remained unclear to the field, if Li-garnets are a viable option as an electrolyte for all thin film based microbatteries. Ultimately, the deposition of the highly conductive cubic phase of $Li_7La_3Zr_2O_{12}$ (LLZO) in the form of thin films was so far never achieved by pulsed laser deposition (PLD). Among aspects such as compatibility with different oxide and nitride electrode materials, structural dependence on ionic transport properties in thin film, and the influence of bulk to thin film transfer, motivated the work performed in the following thesis.

Part I, as the general introduction, will cover fundamentals of liquid-based batteries, their history, their working principle as well as current state-of-the-art benchmarks regarding energy and power density. Furthermore, we will review current all solid state battery cells for both, bulk and microbattery performance. Afterwards, main focus will be moved towards lithiated thin films and their application in memory, sensing and energy storage entities, with particular attention toward Li-garnets as a material class. Here, we summarize efforts made in structural phase stabilization and tuning of ionic transport properties by means of doping. To conclude, we will review current attempts on hybrid-based cell designs, and compare them to full ceramic all solid state battery concepts.

Part II will cover the first combination of a thin film anode material, namely $Li_4Ti_5O_{12}$ (LTO) with Li-garnet LLZO. Thin film deposition through pulsed laser deposition (PLD) will be introduced for the fabrication of thin films of $Li_4Ti_5O_{12}$, grown on oriented MgO substrates, as well as on bulk Li-garnet pellets. We extend the study towards structural phase evolution and assess the electrochemical potential in a half-cell pellet-based battery assembly. Galvanostatic cycling at various rates will be performed and capacity retention will be reported and discussed.

Following **Part III**, aspects of the influence of nitrides in combination with LLZO are further elaborated. Here, we investigate the phase evolution of multilayers consisting of Li_3N and LLZO deposited by pulsed laser deposition. Structural phase evolution as a function of temperature is measured in-situ as well as ex-situ and ionic transport properties in relation to crystallographic phase are assessed. As a necessity for high Li-ion conductivity, the stabilization of the highly conductive cubic phase of LLZO is required. Nevertheless, up to this date, it was proven to be vastly challenging to achieve the cubic phase and high Li-conductivity in thin films of LLZO, with no report on PLD-deposited thin films of the Li-garnet material class whatsoever.

Here, we contribute to the detailed understanding of thin film phase formation in $Li_{6.25}Al_{0.25}La_3Zr_2O_{12}$ by employing a novel strategy, embedding a sacrificial Li-reservoir in the form of thin layers of Li_3N, which upon a thermal post-annealing step, allows for diffusion into the garnet host material, therefore compensating the occurring Li-deficiency at elevated temperature. Ultimately, we assess ionic transport properties in thin films fabricated by this strategy via electrical impedance spectroscopy (EIS), and discuss the implication of highly lithiated garnet thin films on applications such as stationary or portable energy storage systems and microbattery, sensing and monitoring entities.

In **Part IV**, a thin film ceramic microbattery is constructed consisting of $LiNi_{0.8}Co_{0.15}Al_{0.05}O_2$ (NCA) thin film cathode, $Li_{6.25}Al_{0.25}La_3Zr_2O_{12}$ thin film electrolyte and Li_7MnN_4 (LMN) thin film anode. Particular focus is set on the growth and adhesion of the respective layers and their feasibility to operate as a full microbattery cell of less than 1 µm total thickness. Notably, thin films of Li_7MnN_4 anode have so far never been deposited or characterized in the form of thin films, neither were they combined with garnet electrolytes. The role of a nitride electrode in combination with an oxide electrolyte was of particular interest, leading over to the interesting role of nitrides in combination with Li-garnets, which were discussed in the previous chapter (Part III).

Part V will introduce efforts taken to experimentally gather data for microbattery testing at very low currents. Upon reviewing available commercial systems for battery testing at the time of the experimental process, no suitable systems for galvanostatic cycling at rates below 100 nA were commercially available. Since the testing protocol included pellet-based batteries with thin film anodes and microbatteries of less than 1 μm total thickness, it was necessary to cycle at rates below 1C. Here, we introduce own written software for the purpose of battery testing, memory logic testing as well as pulsed voltage cycling. Customized functions for autonomous cycling testing at different rates for microbattery application was released as an open source software publication, aiding future research on nanoscopic energy storage devices.

The thesis concludes with **Part VI**, in which an overview on achievements in this thesis is critically reflected towards the field, followed by a discussion on potential applications in energy storage devices and portable electronics. Short summaries on each chapter are given as well as a separate section on future challenges in the field of all-solid state batteries. In an outlook section, we propose further experiments and directions, towards which the following thesis could be expanded in a continuation of this work on Li-garnet and its applications.

Zusammenfassung

In den letzten Jahren bestand ein zunehmender Bedarf an sicheren und hoch energiedichten Energiespeichersystemen basierend auf Feststoff-Elektrolyten. Im Zusammenhang mit der wachsenden Nachfrage nach tragbaren Elektronikgeräten aller Art, wie zum Beispiel tragbaren Mikrochips mit Sensor- und Messmöglichkeiten, wurde der Energiespeicher bald als Engpass für den technologischen Fortschritt identifiziert. Hier konnten Feststoff-Batteriesysteme einige wichtige Mängel beheben, wie zum Beispiel Entflammbarkeit und den einhergehenden reduzierten Verpackungsbedarf, sowie eine mögliche Kompatibilität mit unerforschten Elektroden von hoher Energie- und Leistungsdichte.

Der Einsatz von flüssigen oder Polymer-basierten Elektrolyten, insbesondere von jenen ganz ohne Kohlenstoffbestandteile, ist sehr wünschenswert, aber bisher weitgehend unerforscht. Der Mangel an experimentellen Belegen für das Funktionieren von vollkeramischen Mikrobatterien soll in der folgenden Doktorarbeit thematisiert werden.

Die Verträglichkeit von Lithium-Metalloxid-Anoden in Form von dünnen Schichten steht im Fokus und wurde bisher nicht in Kombination mit Lithium-Granat-Elektrolyten getestet. In ähnlicher Weise blieb bisher auch offen, ob Lithium-Granate als Elektrolyt für vollkeramische Mikrobatterien überhaupt geeignet sind. Die Abscheidung der hochleitfähigen kubischen Phase von $Li_7La_3Zr_2O_{12}$ (LLZO) in Form von dünnen Schichten wurde bisher durch gepulste Laserabscheidung (PLD) nicht erreicht. Unter anderem die Kompatibilität mit verschiedenen Oxiden und Nitriden als Elektrodenmaterialien, deren strukturelle Abhängigkeit und ionische Transporteigenschaften im Dünnfilm, wie auch der Einfluss von makroskopischen Systemen und deren Transfer zu Dünnfilmen sind als zusätzliche Motivation für die folgende Arbeit zu verstehen.

Teil I, der als allgemeine Einführung verfasst ist, behandelt die Grundlagen zu Flüssig-Elektrolyt-Batterien, deren Herkunft und Geschichte, Funktionsprinzip sowie den aktuellen Stand der Technik in Bezug auf Energie und Leistungsdichte. Darüber hinaus werden aktuelle vollkeramische Batteriezellen mit makroskopischen Bauelementen, wie auch als Dünnschichtauftragung miteinander in Ihrer Leistung verglichen. Danach wird der Schwerpunkt auf lithiumhaltige Dünnschichten und deren Anwendung in Speicher-, Sensor- und Energiespeichereinheiten gelegt, mit besonderem Augenmerk auf Lithium-Granaten als

Materialklasse. Hier fassen wir die Bemühungen zur strukturellen Phasenstabilisierung und Abstimmung der ionischen Transporteigenschaften durch Dotierung zusammen. Abschliessend werden die aktuellen Versuche zu hybriden Zelldesigns gesammelt und mit vollkeramischen Festkörperbatteriekonzepten verglichen.

Teil II umfasst die Kombination eines Dünnschicht-Anoden-Materials, $Li_4Ti_5O_{12}$ (LTO), mit Lithium-Granat, LLZO. Für die Herstellung von Dünnschichten aus $Li_4Ti_5O_{12}$, aufgewachsen auf orientierten MgO-Substraten sowie auf Granatpellets, wird die Dünnschichtabscheidung durch gepulste Laserabscheidung (PLD) eingeführt. Wir erweitern die Studie auf die strukturelle Phasenentwicklung und bewerten das elektrochemische Potential in einer pellet-basierten Halbzelle. Galvanostatische Zyklen mit verschiedenen Geschwindigkeiten werden durchgeführt und die Kapazitätserhaltung wird berichtet und diskutiert.

Im nachfolgenden **Teil III** werden Aspekte des Einflusses von Nitriden in Kombination mit LLZO weiter ausgearbeitet. Hier untersuchen wir die Phasenentwicklung von Mehrschichten aus Li_3N und LLZO, die durch gepulste Laserabscheidung abgeschieden werden. Die strukturelle Phasenentwicklung in Abhängigkeit von der Temperatur wird sowohl in-situ wie auch ex-situ gemessen und ionische Transporteigenschaften werden in Bezug auf die kristallographische Phase, die sich bildet, gesetzt. Als Voraussetzung für eine hohe Lithium-Ionen-Leitfähigkeit ist die Stabilisierung der hochleitfähigen kubischen Phase von LLZO erforderlich. Dennoch erwies es sich – bis zu diesem Zeitpunkt – als grosse Herausforderung, die kubische Phase und deren hohe Lithium-Leitfähigkeit in dünnen Schichten von LLZO zu erreichen, ohne Berichte in der Literatur über PLD abgeschiedene dünne Schichten mit hoher Leitfähigkeit in der Lithium-Granat-Materialklasse.

Hier tragen wir zum detaillierten Verständnis der Dünnschicht-Phasenbildung in $Li_{6.25}Al_{0.25}La_3Zr_2O_{12}$ bei, indem wir eine neuartige Strategie anwenden und ein Li-Reservoir in Form von dünnen Li_3N-Schichten einbetten, das bei einem thermischen Nachglühschritt die Diffusion in das Granat-Material ermöglicht und somit den auftretenden Li-Mangel bei erhöhter Temperatur kompensiert. Schliesslich bewerten wir die ionischen Transporteigenschaften in dünnen Schichten, die mit dieser Strategie hergestellt wurden, mittels elektrischer Impedanzspektroskopie, und diskutieren die Auswirkungen von ausreichend lithierten Granat-Dünnschichten auf Anwendungen wie stationäre oder tragbare Energiespeichersysteme und Mikrobatterien, Sensoren und autonome Beobachtungssysteme.

In **Teil IV** wird zunächst eine Dünnschicht-Keramik-Mikrobatterie, bestehend aus $LiNi_{0.8}Co_{0.15}Al_{0.05}O_2$ (NCA) Dünnschicht-Kathode, $Li_{6.25}Al_{0.25}La_3Zr_2O_{12}$ Dünnschicht-Elektrolyt und Li_7MnN_4 (LMN) als Dünnschicht-Anode, aufgebaut. Besonderes Augenmerk wird auf das Wachstum und die Adhäsion der jeweiligen Schichten und deren Eignung unter Last als vollständige Mikrobatteriezelle mit einer Gesamtdicke von weniger als 1 μm gelegt. Vor allem dünne Schichten der Li_7MnN_4-Anode wurden bisher weder abgeschieden noch in Form von dünnen Schichten charakterisiert, noch wurden sie mit Granat-Elektrolyten kombiniert. Die Rolle der *Nitrid-Elektrode* in Kombination mit dem *Oxid-Elektrolyten* war von besonderem Interesse, was zu der spannenden Rolle der Nitride in Kombination mit Lithium-Granaten führte, die im vorhergehenden Kapitel (Teil III) diskutiert wurden.

In **Teil V** werden die Bemühungen zur experimentellen Erfassung von Daten für die Mikrobatterieprüfung bei sehr niedrigen Strömen vorgestellt. Nach Prüfung der zum Zeitpunkt der Experimente verfügbaren kommerziellen Systeme für die Batterieprüfung waren keine geeigneten Systeme für galvanostatische Zyklen mit Strömen unter 100 nA kommerziell verfügbar. Da das Testprotokoll jedoch makroskopische Pellet-basierte Batterien mit Dünnschicht-Anoden und Mikrobatterien von weniger als 1 μm Gesamtdicke enthielt, war es notwendig, mit Raten unter 1C zu arbeiten. Hier stellen wir eigene, selbst geschriebene Software zum Testen von Batterien, Speicherlogiken wie in Memristoren, sowie gepulste Spannungsprüfprotokolle vor. Eigens angepasste Funktionen für das autonome Testen von Mikrobatterien mit unterschiedlichen Raten für das Laden und Entladen wurde als Open-Source-Software-Publikation veröffentlicht, die zukünftige Forschung an nanoskopischen Energiespeichersystemen unterstützen soll.

Die Doktorarbeit schliesst mit **Teil VI**, in dem die Leistungen, die in dieser Arbeit erbracht wurden, zusammengefasst und kritisch reflektiert werden, gefolgt von einer Diskussion über mögliche Anwendungen in Energiespeichern und tragbaren Elektroniken. Kurze Zusammenfassungen zu den einzelnen Kapiteln, sowie ein separater Abschnitt über zukünftige Herausforderungen im Bereich der Feststoff-Elektrolyt-Batterien, runden dieses Kapitel ab. In einem separaten Abschnitt mit dem Titel „Ausblick" schlagen wir weitere Experimente und Richtungen vor, zu denen die folgende Doktorarbeit in einer Fortsetzung dieser Arbeit über Lithium-Granate und deren Anwendungen erweitert werden könnte.

Table of Contents

PART III: A Low Ride on Processing Temperature for a Fast Li Conduction in Garnet Solid State Battery Films 51

Table of Contents

PART I: General Introduction

1   Chemical Energy Storage Systems: Past and Present

Battery research already dates back to around 1800, where Alessandro Volta conducted first experiments on piles of copper and zinc, forming the first reported electrochemical cell of modern history.[1] Volta's invention soon after allowed for the first splitting of water by electrolysis as demonstrated in the invention by Carlisle & Nicholson,[2] which was revolutionary at that time.

Research on this young field went on, and primary batteries came to life. Due to the irreversible nature of the electrochemical reaction occurring upon discharge in primary cells, those are non-rechargeable. Broad adoption in all kinds of modern portable electronics soon followed, even though this first generation cell often contained toxic heavy metals and hazardous acids as common constituents. Unresolved waste issues and an increasing demand for rechargeable battery technology drove the development of secondary cells.

As a first rechargeable secondary battery, the lead-acid system was invented in 1859,[3] still offering a poor energy-to-weight ratio, but at low cost and sufficient power density to be used in automotive starters up to the present date. The next generation of secondary cells faced challenges with toxic ingredients such as cadmium as a constituent and was mostly nickel-based, such as nickel-cadmium, or of nickel-metal hydride type.

1.1   The Victory of the Lithium Ion

Current state-of-the-art battery system are based on rechargeable Li-ion technology, employing liquid or polymer-based electrolytes. However, lithium, as the mobile ion moving between the anode and cathode, is not the only choice to base energy storage devices on: Other ions, even multivalent ones, such as Na^{2+},[4] Mg^{2+}[5] and Al^{3+}[6] are viable alternatives, and focus of ongoing research efforts.[7–10] The development of "beyond-Lithium" energy storage systems is, however, still dealing with issues and obstacles such as poor mobility of larger ions in solids and the limited availability of high capacity electrodes.[8] Thus, Li^+ became the predominant ion in battery cells of today, due to its small size, and therefore high mobility in rigid crystal structures of electrodes, allowing for insertion and extraction at high rates.[11]

The relevance of battery research in a growing field of mobile and portable electronics cannot be underestimated. With the growing demand in off-grid storage for renewable energy production, battery research even grew into the role of a key enabler for a non-fossil energy economy.[12,13] With this transformative mission in mind, it became obvious that current batteries not yet have the maturity to fulfill this role.[14] Ever since batteries made their way into the mass market be it through smartphones and laptops or fully electric cars, their flaws, such as poor cycle life and flammability became apparent.

As a founding father of modern lithium-ion battery technology, John B. Goodenough, showed for the first time reversible cycling in $LiCoO_2$ in 1980, and therewith established the field of rechargeable Li-ion based electrochemical cells.[15] Impressive enough, born in 1922 and now at the age of 96, Goodenough is still an active researcher at the University of Texas, Austin and contributes to all modern approaches of novel electrolyte development, including garnet-type $Li_7La_3Zr_2O_{12}$, the main focus of the following chapters of this thesis.[16,17]

1.2   Different Types of Batteries: From Liquid to All-Solid

The general working principle of three different kinds of batteries relevant for this thesis are illustrated in Figure 1. All electrochemical cells are composed of a negative anode and a positive cathode and are separated by an electronically insulating but ionically conductive electrolyte. Upon discharge, the respective electrodes are connected to an external circuit driving a load, and the difference in voltage potential on either side allows for the conduction of ions through the electrolyte, inducing respective reduction and oxidation reactions at the cathode and anode side, respectively. Classical liquid-based cells are depicted in Figure 1a. Here, anode and cathode, the respective negative and positive electrodes of the electrochemical cell under discharge, are shown in red and green. In between, separated by an ion conductive barrier layer, a metal salt is dissolved in an organic solvent such as propylene carbonate (PC), dimethoxyethane (DME), ethylene carbonate (EC) or dimethyl carbonate (DC). Typical metal salts for liquid lithium ion batteries are $LiPF_6$ or $LiBF_4$. In those cells, the thermal stability window under which the cell can safely be operated is usually restricted to $< 100\ °C$ with severe danger for explosions and flammability upon violation.[18] Due to the liquid nature of the electrolyte, also substantial packaging is necessary, decreasing effective energy and power density. As an intermediate category towards all solid state battery cells, hybrid-based systems, as depicted in Figure 1b, can be considered. Here, still employing carbon constituents and/or organic solvents, an inorganic membrane separates both electrodes preventing short circuits upon direct contact. By this, safety is already vastly improved, however, at the cost of inherited flaws of liquid-based batteries such as restricted temperature operation windows and increased packaging needs. In the all solid state battery design shown in Figure 1c, only inorganic components are involved in the cell assembly.
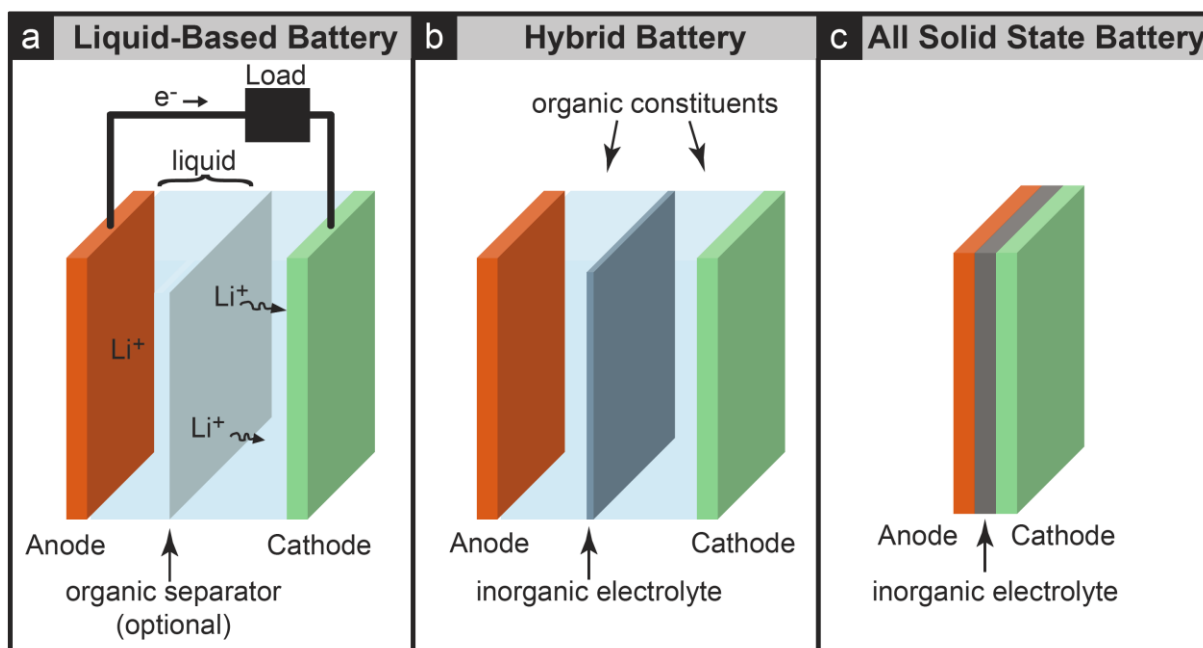
Figure 1 Schematic of the general working principle of secondary lithium ion batteries. Upon discharge, Li^+-ions move from the negative anode (red) towards the positive cathode (green) through the electronically insulating electrolyte (blue). To compensate the charge, electrons move through the attached load. Upon charging, the direction of movement is inversed. a) Liquid-based battery cell employ an ionically conductive separator membrane immersed in an organic solvent consisting a lithium metal salt. b) Hybrid lithium ion battery cells still contain carbon constituents, but employ an inorganic solid electrolyte separator, either in the form of a pellet, a tape or a membrane. c) All solid state Li^+-ion battery cells do not contain carbon constituents, therefore allowing for a higher thermal operation window, increased safety and higher energy density due to the reduced packaging needs.

Here, packaging can be reduced, while maximizing the volume of the electrodes therefore maximizing the active material in the cell, with great benefits towards high energy and power density. Such a cell design not only largely increases the usable temperature range for battery operation, it also allows for ongoing miniaturization of all active battery components, which are so far inaccessible with liquid-based technology. Thus, all ceramic, fully solid state batteries will be the focus of this thesis, together with an implementation of a ceramic solid state electrolyte into half- and full-cells with various electrode materials. Building on experience gained on liquid-based batteries from the past,[19] we try to apply usable voltage regimes, chemical stability, structural rigidity to novel types of solid state cells, without the use of carbon constituents.

1.3   Prerequisites for an "ideal" Solid Electrolyte

In this context, one may curiously ask, which requirements and prerequisites an inorganic electrolyte shall offer, to fulfill present and future needs in terms of device integrability? Here, Figure 2 offers a comprehensive summary: Fist of all, the final costs of a new solid state approach will strongly determine if a new technology will be broadly adopted. Since batteries are produced and sold in large quantity, both the raw material cost as well as the cost of fabrication will need to be competitive towards classical battery manufacturing,[13,20] which is mostly based on liquid slurry casting, spray drying and fabricated in cheap continuous processing.[21] Luckily, the cost of raw materials usually correlate with the abundance of the respective element in the earths' crust and a more abundant choice of raw materials will therefore be rewarded with lower cost of the components.[22] A solid electrolyte has to offer high ionic conductivity in combination with low or – in an ideal case – absent electronic contributions. In addition, the stability towards high voltage cathodes is of utter importance, if the electrolyte shall be integrated towards high power and energy density for the cell design. For this, an ideal interface compatibility is desired, also towards low voltage anodes and – ideally – even towards metallic lithium directly, which allows for the integration of the highest possible capacity anode with the lowest possible voltage in such a cell. Regarding lithium compatibility, particular attention also has to lay in the resistance of the electrolyte towards lithium dendrite propagation, a known phenomenon also in liquid-based batteries, often

reducing cycling life and capacity retention up to cell death from short circuiting issues.[23–25] Preventing short circuits in battery cells has recently been one of the major research foci to improve general safety of modern battery cells. Short circuits in batteries can quickly provoke thermal runaway with the risk of inflammation and uncontrolled burn-down,[18] especially with the flammable liquids used in classical cells. Here solid state has the clear advantage of higher mechanical rigidity and – in the case of metal oxide based electrolytes – even the advantage of a wide temperature window, under which a cell can safely be operated. Due to the reduced packaging needs of solid state technology, one may envision device integration of such solid state cells, which have been inaccessible so far by liquid-based systems, moving from wearable computing units, to microscopic sensing entities, down to nanoscopic implantable medical units directly operating in the blood stream.[26,27]

In summary, desired requirements of an "ideal electrolyte" have to range from wise choice on available raw materials, their electrochemical properties, their transport properties as well as their integration into suitable high energy and power density cells.
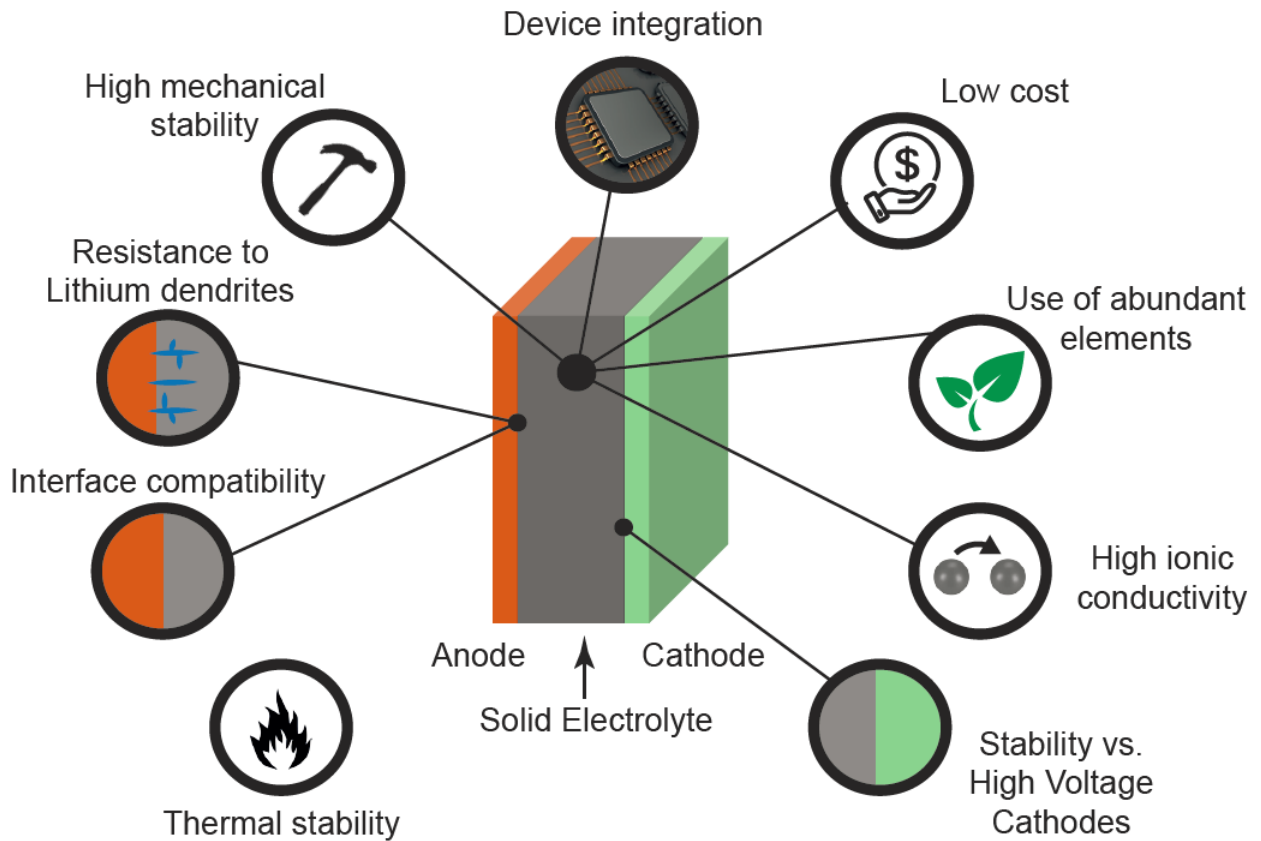
Figure 2 Summary of desired requirements for a solid electrolyte for energy storage applications. Not all of the desired properties are available for each material class of solid electrolytes; some are imposing constraints on others, such as the use of abundant elements, which can deteriorate high ionic conductivity. Others depend on each other, such as the interrelation between mechanical stability and resistance towards lithium dendrite propagation[23,28] or the necessity of low production cost and its dependence on whether device integration is economically feasible.

1. Review on Available Solid State Electrolyte Materials

With the knowledge about an "ideal electrolyte" in mind, we focus now on a comparison of available solid electrolytes and will elaborate advantages and disadvantages of each material class. In accordance, Table 1 summarizes most common solid electrolytes materials. In this context, LIPON (lithium phosphorus oxynitrides) can be regarded as the most mature of the listed solid electrolytes.[29] Broad application, also already in first commercial solid state batteries,[30] has driven an ongoing interest in this material. Offering an electrochemical stability window of 0-5.5 V vs. metallic lithium[29] combined with good stability in Li / LIPON / LiCoO$_2$ based cells,[31] allowed it to quickly emerge in small power portable applications. However, suffering from poor ionic conductivity[32] (1-2 μScm^{-1}) high power density remains inaccessible by this material. Even though apparent stability is observed in this material in contact with metallic lithium, Schwöbel et al.[33] pointed out that decomposition reactions of LIPON into Li$_3$PO$_4$, Li$_3$P, Li$_3$N and Li$_2$O form an inevitable self-passivation layer, which imposes kinetic limitations upon cycling. In addition, its fabrication in thin film form requires expensive and difficult processing steps,[29,34] preventing broad adaption to the battery market so far.

NASICON-type materials,[35,36] NaM$_2$(PO$_4$)$_3$ with M = Ge,Ti,Zr, were already discovered 50 years ago.[36–38] A transformation from a sodium ion conductor to a lithium ion conductor was achieved by substitution of M with a mixture of Aluminum and Titanium of which Li$_{1.3}$Al$_{0.3}$Ti$_{1.7}$(PO$_4$)$_3$ (LATP) offers appealing conductivity of 3×10^{-3} Scm^{-1}.[35,39] Similarly, the substitution of Titanium with Germanium leads to Li$_{1.5}$Al$_{0.5}$Ge$_{1.5}$(PO$_4$)$_3$ (LAGP) with conductivities of 5×10^{-4} Scm^{-1}.[40,41] However, due to the insufficient stability of the Ti^{4+} ion, poor stability in contact with metallic lithium has to be noted together with air sensitivity issues.[42–44]

LISICON (lithium super ionic conductor), discovered in 1978[45] and with stoichiometry (Li$_{14}$Zn(GeO$_4$)$_4$, forms another material class with typical ionic conductivity around 10^{-6} Scm^{-1}. However, it shows reported incompatibility vs. metallic lithium and degradation issues in the presence of CO$_2$ and decomposes above ~300 °C.[46–48] Progress on the stoichiometry, mostly owned to a substitution of the oxide ions with sulfide ones, introduced

the so called thio-LISICON material class,[49,50] with the advantage of a drastic increase in conductivity. A combination of silicon and phosphorous dopants forming $Li_{3.4}Si_{0.4}P_{0.6}S_4$ resulted in a high conductivity of 6.4×10^{-4} Scm^{-1} with stability vs metallic lithium up to 5 V.[51] More recently, the thio-LISICON family was extended by $Li_{10}GeP_2S_{12}$ (LGPS),[49,52,53] where conductivity could be improved even further, offering remarkable ionic conductivity of 12 mScm^{-1} at room temperature.[52] However, this was only achieved at the cost of incompatibility with metallic lithium.[53,54] Regarding the usable electrochemical stability window, a rather narrow 1.71-2.14 V vs. Li/Li$^+$ have to be noted,[53] which make it unpractical to combine with high voltage cathodes or low voltage anodes.

Li_2S-based glasses, most common are mixtures of Li_2S with P_2S_5 or GeS_2 offer conductivities around 10^{-3} Scm^{-1},[55,56] but tend to form H_2S in air due to chemical instability and high hygroscopicity of the compounds.[57,58] However, the amorphous nature of those glasses allows for a good protection against propagation of lithium dendrites, which prefer growth along defined crystallographic boundaries, and therefore good cycle life.[55,59,60]

From the perovskite type ion conductors with general formula ABO_3, the $Li_{3x}La_{2/3-x}TiO_3$ (LLTO) material class family achieved good conductivities of $> 10^{-3}$ Scm^{-1} for x = 0.11.[61,62] Due to the much higher grain boundary resistance (in comparison to bulk), a strong influence and dependence on the deposition method and substrate is expected for the total conductivity, which may vary by two orders of magnitude when deposited in thin film.[63,64] In addition, titaniums' Ti^{4+} facile reducibility – as for the case of LATP – prevents again stability in contact with metallic lithium for this material class.[65,66]

Lastly, the Garnet material class, with general structure type of $A_3B_2(XO_4)_3$ was firstly probed for its lithium conductivity by Weppner and Thanugudarai,[67,68] achieving 10^{-6} Scm^{-1} for $Li_5La_3X_2O_{12}$ with X = Nb or Ta. Soon after, compatibility with metallic lithium[69,70] as well as a wide electrochemical stability window for this material class could be reported, with a stability window of 0-9 Volts against Li/Li$^{+[71]}$ for a garnet with stoichiometry of $Li_{6.75}La_3Zr_{1.75}Nb_{0.25}O_{12}$. In LLZO with general formula $Li_7La_3Zr_2O_{12}$, two different crystallographic phases can be observed, a low conductive tetragonal phase (phase group *I4$_1$/acd*)[72] as a room temperature polymorph, and a highly conductive cubic phase (phase group *Ia3$\bar{}$d*[70] or the most recently described acentric cubic *I-43d*[73,74]) as firstly identified by Awaka et al.[75,76] as a high temperature polymorph. Since the tetragonal polymorph only achieved conductivities in the range of 10^{-5} Scm$^{-1[75]}$ (as opposed to the cubic phase with

10^{-3} Scm^{-1}[70,77]) the stabilization of the cubic phase of $Li_7La_3Zr_2O_{12}$ at room temperature gained particular attention: Though, it was found to be only accessible through doping the structure with several elements on either the Li-site (Al^{3+}, Fe^{3+} and Ga^{3+})[77–81], the La-site (Sr^{2+}, Nd^{3+})[82,83] or on the Zr-site (mainly Ta^{5+})[17,84]. It was found that > 0.2 mol of Al^{3+} as a substitute for Lithium is able to stabilize the cubic phase down to room temperature.[72,77,85] Similarly, the addition of Ta in a quantity of 0.25 mol, as a substitute for Zirconium, equally stabilized the cubic polymorph at room temperature.[84,86] In this study we focus on LLZO doped on the Li-site with Al^{3+}, which was reported to exhibit one of the highest Li-ion conductivities as well as the required phase stability.[87–89]

Table 1: Comparison of most common solid electrolytes, their room temperature conductivities as well as advantages and disadvantages for the use as energy storage electrolytes. The symbol (*) indicates that stability towards Li metal originates from the stability of decomposition products.

Solid Electrolyte	Conductivity [Scm^{-1}] At RT	Advantages	Disadvantages	Reference
LIPON	10^{-6}-10^{-8}	Stable with Li metal(*) Broad electrochemical stability window (0-5.5 V vs Li/Li$^+$) Already in use as for thin film batteries	Low conductivity Expensive in production Difficult processing	[31–33,90]
NASICON-type (LATP, LAGP)	10^{-4}-10^{-3}	Stability in air High temperature operation	Unstable with Li metal Sensitivity to moisture Brittleness	[35,42–44,91,92]
(Thio-)LISICON-type (Li$_{14}$ZnGe$_4$O$_{16}$, LGPS, Li$_{4-2x}$Zn$_x$GeS$_4$)	10^{-2}	Very high conductivities	Sensitivity to moisture and O$_2$ Narrow stability window High cost of germanium	[46–49,52–54]
Glassy sulfides (Binary Li$_2$S-P$_2$S$_5$ Ternary Li$_2$S-A$_x$B$_y$-P$_2$S$_5$)	10^{-4} to 10^{-2}	Stable with Li metal(*) High conductivity Mechanically tolerant	Hygroscopic sensitivity to moisture and O$_2$ H$_2$S formation	[55,58,59,93]
Perovskite LLTO (Li$_{3x}$La$_{2/3-x}$TiO$_3$)	10^{-6}-10^{-3}	High conductivity Good mechanical properties High oxidation voltage	Unstable with Li metal Titanium reactivity with electrode materials	[62,66]
Garnet LLZO	10^{-3}	Good conductivity Stable with Li metal Good mechanical properties Broad electrochemical stability window (0-9 V vs. Li/Li$^+$)	Sensitivity to moisture and CO$_2$ High cost High conduction in thin film hard to get.	[71,72,75,77,94,95]

1.4   Ionic Transport Properties of Common Solid Electrolytes

In terms of ionic transport properties of solid electrolytes, a comparison on Arrhenius type conductivity summarizes recent achievements, Figure 3. Here, the logarithmic representation of ionic conductivity is plotted against the reciprocal temperature in a temperature range of 200 °C to 600 °C, with room temperature operation marked in a grey line. Different solid electrolytes are compared to common liquid and polymer electrolytes. Notably, inorganic electrolytes such as glassy sulfide $Li_7P_3S_{11}$ or $Li_{10}GeP_2S_{12}$ (LGPS) – both of sulfide type – outperform liquid electrolytes[96] such as the common EC:PC:$LiPF_6$ or also the typical polymer electrolyte P(EO)$_{12}$-LiTFSI.[97] From the perspective of ionic transport properties, one may therefore at first see sulfides as the clear winner in terms of electrolyte choice for future solid state battery cells, leaving LIPON, garnet LLZO, as well as LISICON at least two orders of magnitude behind in ionic conductivity at room temperature.

Sufficient ionic conductivity, however, is not the only prerequisite for a successful implementation in an electrochemical cell: Equally important are the obtainable internal resistances of the entire system, which also depend on the average distance, by which the electrodes are separated. Here, a typical distance by which standard liquid-based battery electrodes are usually separated is 50 μm, resulting in a specific resistance of about 1 Ωcm^2.[98] If a respective solid electrolyte has the capability of being processed as a thin film, one may greatly reduce the separation distance to 100 nm or below, thereby achieving similar total specific resistance values as for the case of a liquid electrolyte. For the assumption of a garnet electrolyte with 1 $mScm^{-1}$ conductivity,[80] deposited at a thickness of 100 nm, the specific resistance becomes 0.01 Ωcm^2, thereby outperforming liquid-based cells.

In other words, to maintain the specific resistance of a liquid-based cell with ~1 Ωcm^2, a conductivity of 10^{-5} Scm^{-1} or higher in a thin film solid electrolyte of 100 nm thickness can still be tolerated, with equal performance in terms of transport properties.

The obtainable ionic conductivity of solid state electrolyte materials therefore does not determine alone their applicability in solid state electrochemical cells. In order for a satisfactory integration into electrochemical cells, aspects such as i) wide electrochemical stability window towards high capacity electrodes, ii) transferability to thin film form, iii) facile fabrication with tolerance towards exposure to environmental conditions, are equally important and shall be reviewed in detail in the following section.
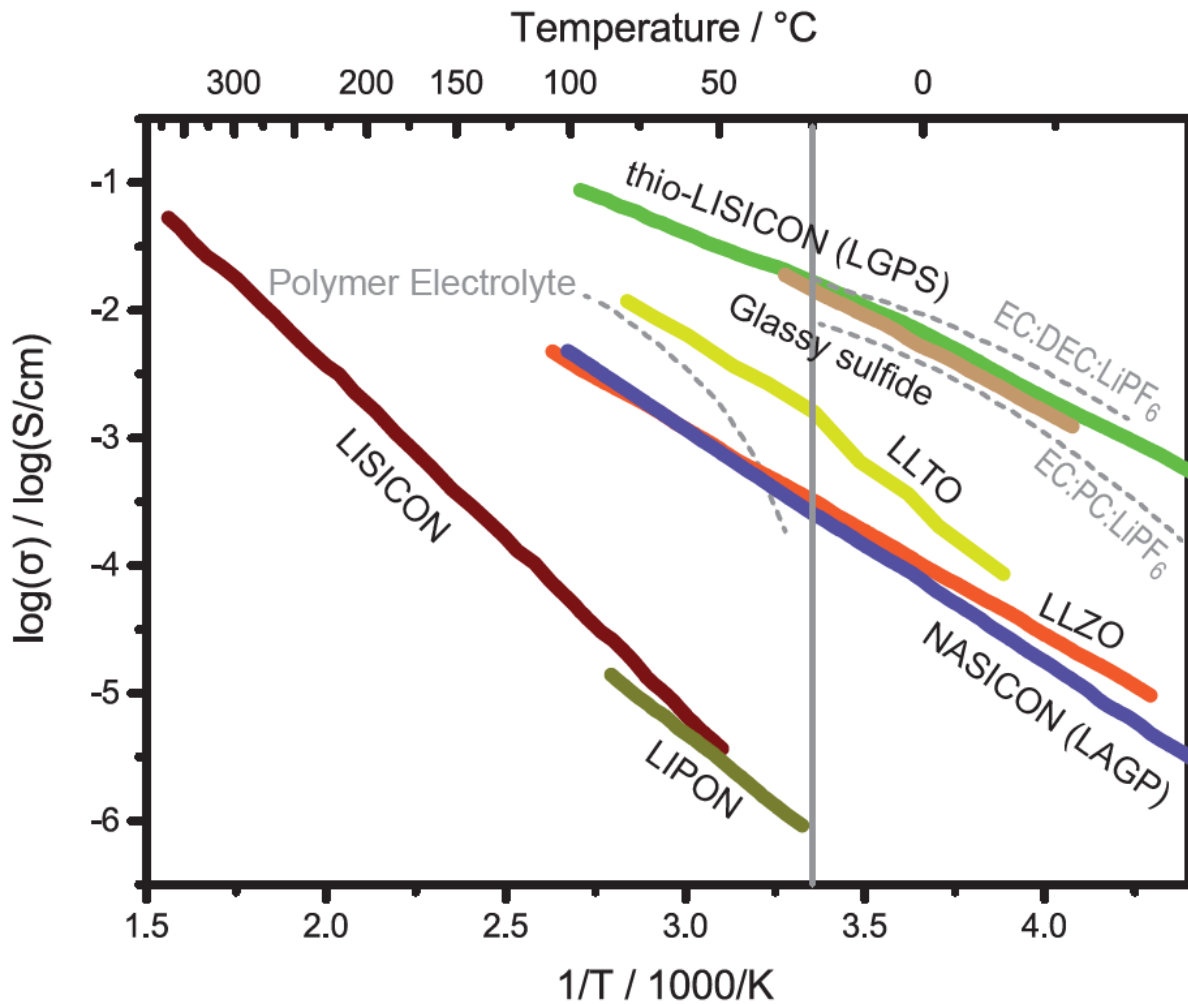
Figure 3 Arrhenius type conduction plot of selected solid state electrolyte materials in comparison to liquid and polymer electrolytes. The data summarizes LIPON,[29] LISICON-type $Li_{3.5}Zn_{0.25}GeO_4$,[46] NASICON-type $Li_{1.5}Al_{0.5}Ge_{1.5}(PO_4)_3$,[40,41] LLZO[89], LLTO[66], glassy sulfide-type $Li_7P_3S_{11}$,[99] thio-LISICON-type $Li_{10}GeP_2S_{12}$[52] together with EC:PC:LiPF$_6$ and EC:DEC:LiPF$_6$ as two typical liquid electrolytes[96] in lithium ion batteries. As a polymer electrolyte P(EO)$_{12}$-LiTFSI[97] was selected for comparison. Adopted from Zeier et al.[100]. The grey vertical line indicates room temperature.

1.5 Electrochemical Stability Window

In order to be of practical use as an electrolyte integrated in an electrochemical energy storage cell, a high voltage stability window in the electrolyte is desired. Since the operation window should cover high capacity anode electrodes such metallic lithium at 0 V, allowing its direct usage and offering the highest possible capacity anode (3860 mAh/g[60]), as well as also high voltage cathode electrodes operating close to 5 V vs. Li/Li$^+$, the stability window should ideally also cover 0 (metallic lithium) up to > 5 Volts. In accordance, we compare electrochemical stability windows obtained for different solid electrolytes in Figure 4. Here, one may note that the sulfur-based compounds with highest ionic conductivity such as $Li_{10}GeP_2S_{12}$ (see previous section) only allow for a relatively narrow stability window around 2 Volts vs Li/Li$^+$.[101] If a stable interface towards both, a low voltage anode and a high voltage cathode, is envisioned, a material choice with a broader stability window vs. Li metal is clearly preferred.

Importantly, one may note large discrepancies between experimental and predicted electrochemical stability windows in solid electrolytes: First principle calculations, as they were taken from Zhu et al.[102] for Figure 4, only attributed a stability window for LIPON between 0.68 V and 2.63 V, in contradiction to stable cycling with metallic lithium, as it has been reported by Bates et al.[31] in a Li metal / LIPON / $LiCoO_2$ electrochemical cell. The origin of this discrepancy – at least for the case of LIPON – could be explained by Schwöbel et al.[33] and originated from a self-passivation layer, consisting of decomposition products (Li_3N, Li_3P, Li_3PO_4, and Li_2O) which did build up in-situ upon contact with metallic lithium. For the case of Li_2S-glassy electrolytes, Wenzel et al.[93] obtained results from in-situ XPS that suggest the decomposition of $Li_7P_3S_{11}$ at the interface to metallic lithium forming Li_2S and Li_3P as passivation layers, leading to falsely attributed stability toward lithium at 0 V. Similar decomposition products were also found for LGPS-type electrolytes with stoichiometry $Li_{10}GeP_2S_{12}$ upon contact to metallic lithium.[54] However, garnet LLZO with its predicted stability window of 0.05 V to 2.91 V could successfully be integrated in an electrochemical cell cycled to 5.25 Volts employing metallic lithium.[103]

In essence, chemical instabilities at interfaces towards electrodes can be mitigated by the application of appropriate intrinsic or extrinsic passivation layers, therefore extending the stability window beyond thermodynamic predictions. We therefore extended the values taken from first principle calculations by extended ranges (light blue color), towards which the respective materials had experimentally proven chemical stability. In the case of LLZO,

interlayers deposited on the anode side, such as Al_2O_3 or silicon used as wetting agents decreasing contact resistance towards lithium,[103,104] as well as on the cathode side, where $LiNbO_3$ mitigated contact resistances,[105] have both been proven viable strategies.

In this regard, the garnet LLZO offers experimental compatibility with metallic lithium, and reported stability up to 9 Volts vs. Li/Li^+.[71] Notably, the high voltage window in solid state electrolyte materials surpasses, what can commonly be achieved with standard liquid electrolytes, and therefore allows for the integration of yet unexplored high voltage cathodes, which potentially showed poor stability or incompatibility with liquid-based electrolytes. To complete the picture on electrochemical stability, we also compared obtained predictions towards two representative liquid and polymer electrolytes.[106] Here, 1 M $LiPF_6$ dissolved in ethylene carbonate and ethyl methyl carbonate (EC:EMC) in the ratio 3:5 with 5 wt.-% of vinylene carbonate (VC) additive addition was chosen as a selected liquid electrolyte, showing a predicted stability window of 0.5 V to 4.9 V.[106] In the case of a polymer electrolyte, a comparison to poly(ethylene carbonate) (PEC) with lithiumbis(trifluoromethanesulfonimide) (LiTFSI, $LiN(CF_3SO_2)_2$) was chosen, with an onset for electrolyte decomposition at 4.5 Volts.[107]
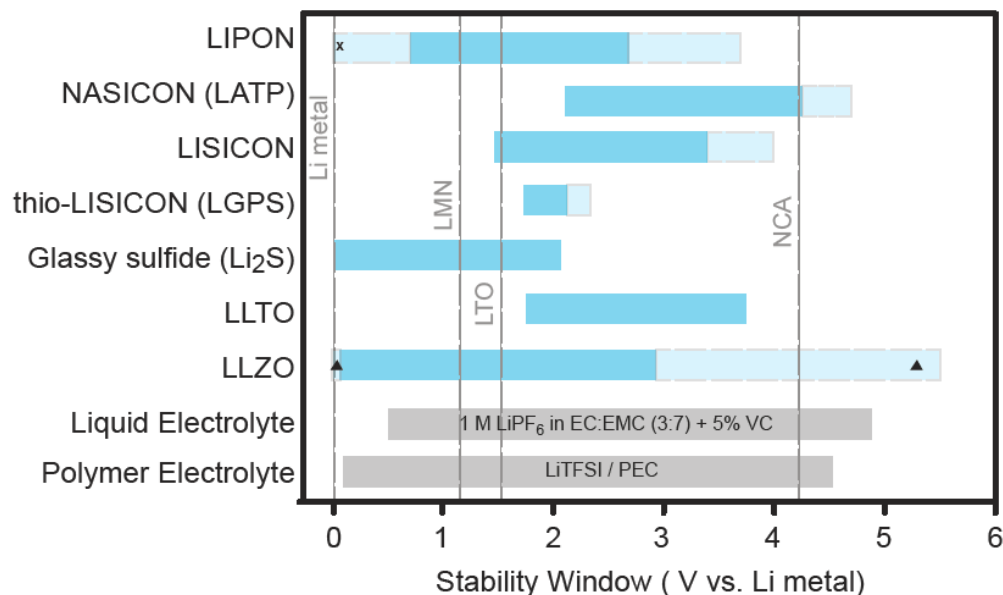
Figure 4 Comparison of electrochemical stability window vs Li/Li$^+$ from first principle calculation taken from Zhu et al[102]. of several solid electrolytes[101] in comparison to a common liquid[106] and polymer[107] electrolyte. The voltage regimes of electrodes relevant for this thesis are shown in grey lines, namely LiNi$_{0.8}$Co$_{0.15}$Al$_{0.05}$O$_2$ (NCA), Li$_4$Ti$_5$O$_{12}$ (LTO), Li$_7$MnN$_4$ (LMN) and metallic lithium. Experimentally determined extended stability windows are indicated for the case of LIPON[31] (x) and LLZO[103] (Δ).

1.6   Transferability to Thin Films

As a third focus for the selection of a solid electrolyte material, its processability as thin layers, either micron-sized tapes or vacuum-processed thin films, shall be evaluated. The quest for thin film processability should, however, not only be seen as a measure to countervail the lower conductivity obtained in comparison to liquid-based electrolytes. On the contrary, scale-down processing will allow to position solid electrolytes as promising candidates for future high energy-density battery systems, with less mass and volume dedicated to inactive packaging and electrolyte and inherent better safety. Their processing in small structures benefits from well-controlled recipes for deposition, allowing for pinhole-free CMOS scale-down processing. CMOS manufacturing, as a key field of ongoing innovation, already developed several profound processes for oxide deposition,[108,109] for which the transfer to the deposition of *lithium* metal oxides can benefit from the rich and profound knowledge, that has already been thoroughly studied with a variety of deposition techniques developed in the past decade (such as PVD[110] in the case of Li_2O ternary oxides or spray pyrolysis[111] in the case of lithium doped Nickel oxide).

In general, thin films of solid state battery electrolytes can be deposited as dense structures ranging from amorphous to crystalline in the hundreds of nanometers in thickness range for different material classes. One advantage is that by the thin film nature, a very short Li-ion pathway is employed between the electrodes, while maintaining there, rigid physical separation through the solid electrolyte film. Furthermore, the opportunity to free up space for larger volume of electrodes that can even be of too high voltage for compatibility with common liquid electrolytes, marks an opportunity that should not be missed out. Even the option of using metallic lithium as an anode to combine with thin layers of solid electrolytes is within reach.[112,113] This directly defines the strong interest for increased energy density in the field of battery research. A comprehensive summary about conductivities in thin films obtained for the most common solid electrolytes is provided in Table 2. Here, we list room temperature ionic conductivities and activation energies for ionic transport obtained by different deposition methods. Not all deposition methods are equally suited for a specific solid electrolyte. In the case of LIPON thin film deposition, RF-magnetron sputtering achieved the best overall electrochemical performance, however at the cost of a relatively low deposition rate of 2 nm/min,[114] whereas pulsed laser deposition achieved 40 nm/min but only with rough thin film

morphology[115] unsuitable for battery integration. In the case of e-beam deposition,[116,117] still moderate deposition rates of 8.3 nm/min are obtained at lowest ionic conductivity in comparison to other methods.

NASICON-type electrolytes have been explored by vacuum deposition techniques leading to thin films,[118] as well as with low-cost and industrial scalable tape-casting[119] mostly preserving the high ionic conductivity of 10^{-4} Scm^{-1} upon thin film transfer.

For Li$_2$S-glassy electrolytes as well as those of thio-LISICON-type, a transfer of the high Li-ion conductivity observed in bulk pellets and membranes remains challenging; Only few attempts on thin film vacuum deposition of those are available[120–124] – covering mostly deposition either by pulsed laser deposition or solution deposition – and generally a two to three order of magnitude decreased ionic conductivity as compared to dense ceramic bodies was obtained. Sulfides tend to decompose in ambient atmosphere, releasing H$_2$S, an effect, which could potentially be enhanced in thin films of this material, making its handling dependent on specialized inert-atmosphere vacuum deposition equipment and which could be an explanation why so few attempts on thin film transfer exist.

Perovskite LLTO and their transfer from bulk ceramics to thin films has also been explored by various deposition techniques ranging from PLD to RF-magnetron sputtering.[63,125] Here, a successful transfer of high conductivity was only observed upon high processing temperatures exceeding 900°C and oxidizing atmosphere. This clearly limits the commercial applicability of this electrolyte material class in later devices, due to a limited choice of applicable substrates and processing conditions.

Notably, for the Li-garnet material class, thin film conductivity data never exceeds a conductivity value of 1.6×10^{-5} Scm^{-1}[126] and most commonly around 10^{-6} Scm^{-1}, which is still two orders of magnitude below reports for bulk pellets,[70,127] indicating difficulties in successful transfer of high conduction in vacuum-based methods. Thus, we focus our attention in the following Chapter III of this thesis towards the understanding of structural and ionic transport properties of LLZO upon thin film transfer thereof.

Table 2 Thin film conductivities and activation energies for ionic transport of common solid state electrolyte materials, deposited by various thin film deposition methods including sputtering, sol-gel deposition and pulsed laser deposition.

Solid Electrolyte Material	Conductivity [Scm^{-1}] At RT	Deposition Method	E$_A$ [eV]	Ref.
LIPON				
	1.8×10^{-6}	RF magnetron sputtering	0.43	[114]
	1.6×10^{-6}	Pulsed Laser Deposition	0.58	[115]
	6×10^{-7}	E-beam Evaporation	0.57	[116,117]
	1.45×10^{-7}	Atomic Layer Deposition	N/A	[128]
NASICON-type				
LATP (Li$_{1.3}$Al$_{0.3}$Ti$_{1.7}$(PO$_4$)$_3$)	2.46×10^{-5}	RF magnetron sputtering	N/A	[118]
LATP	6.47×10^{-6}	RF magnetron sputtering	N/A	[129]
LATP	1.12×10^{-6}	Aerosol deposition	N/A	[130]
LATP	2.7×10^{-6}	Sol-gel deposition+ rapid thermal annealing	0.43	[131]
LAGP (Li$_{1.5}$Al$_{0.5}$Ge$_{1.5}$(PO$_4$)$_3$	5×10^{-4}	Sol-gel deposition	0.33	[41]
LAGP (Li$_{1.4}$Al$_{0.4}$Ge$_{1.6}$(PO$_4$)$_3$	3.38×10^{-4}	Tape-casting	0.32	[119]
LAGP (Li$_{1.5}$Al$_{0.5}$Ge$_{1.5}$(PO$_4$)$_3$	0.5×10^{-5}	Aerosol-Deposition	N/A	[132]
(Thio-)LISICON-type				
33Li$_4$GeS$_4$-67Li$_3$PS-4LPS	1.8×10^{-3}	Pulsed Laser Deposition	0.29	[120]
Li$_{3.25}$Ge$_{0.25}$P$_{0.75}$S$_4$	1.82×10^{-4}	Low-temperature solution deposition	0.42	[121]
Li$_{3.25}$Ge$_{0.25}$P$_{0.75}$S$_4$	1.7×10^{-4}	Pulsed Laser Deposition	0.38	[122]
Glassy sulfides				
80%Li$_2$S 20%P$_2$S$_5$	7.9×10^{-5}	Pulsed Laser Deposition	0.45	[123]
80%Li$_2$S 20%P$_2$S$_5$	2.8×10^{-4}	Pulsed Laser Deposition + Postanealed	0.39	[123]
80%Li$_2$S 20%P$_2$S$_5$	2.6×10^{-6}	Solution Deposition	0.44	[124]
Perovskite LLTO				
Li$_{0.392}$La$_{0.54}$TiO$_3$	1.92×10^{-5}	Pulsed Laser Deposition	0.3	[63]
Li$_{0.31}$La$_{0.41}$TiO$_3$	5.25×10^{-5}	RF magnetron sputtering	0.35	[125]
Li$_{0.45}$La$_{0.48}$TiO$_3$	8.75×10^{-4}	Pulsed Laser Deposition	0.35	[133]
Garnet LLZO				
Al-doped LLZO	1.61×10^{-6}	Pulsed Laser Deposition	0.35	[134]
Al-doped LLZO	2.4×10^{-6}	Sol-gel deposition	0.52	[135]
Ga-doped LLZO	1.6×10^{-5}	RF magnetron co-sputtering	0.66	[126]
Ta,Al-doped LLZO	2.4×10^{-8}	Pulsed Laser Deposition	0.61	[136]
Undoped LLZO	4.2×10^{-6}	CO$_2$-laser assisted CVD	0.5	[137]

1.7 Lithiated Thin Films and Their Application

Lithiated thin films are not only of utter importance in future energy storage devices: Processing of highly lithiated thin film solid state electrolytes is also of high interest for upcoming neuromorphic computing chips, as well as several other applications ranging from memristors[138,139] as a non-volatile and fast next-generation random access memory replacement and a building block of future computing architectures[140,141] closer to how biological brains compute and process. Despite the several key fields that could benefit from technical advancements in lithiated thin film solid state electrolyte development, their understanding and fabrication remains still a challenge in the community. Often Li-containing thin films do not reach the high lithiation degrees desired, as for vacuum processes under the exposure to high temperatures, where severe volatility of Li^+ has been reported.[136] Furthermore, wet chemical processing routes come at the disadvantage of poor growth control in nanoscale and limited downscaling capabilities. Lithiated thin films equally play a significant role in the field of energy storage systems. Not only in large scale battery assemblies, but also for future applications such as biosensors, wearable-computing devices as well as remote-sensing entities for the Internet-of-Things, where highly integrated microbattery designs will be demanded, combined with high energy and power-density electrodes.[142] A solid understanding on phase formation in thin films of lithiated metal oxides, their transport properties and how lithium can be kept in the structure upon the transfer to a thin film therefore are highly relevant. Only a successful transfer of several key properties of solid state electrolytes to the thin film form, such as: transfer of the right crystallographic phase and stoichiometry, preservation of high Li-ion conductivity, will unfold the full potential of lithiated thin films as a competitive electrolyte in future battery designs to free space for electrode volumes and also for all areas of CMOS chip integration such as for microbattery or memory components.

1. Review on All Solid State Batteries

In the context of electrochemical energy storage systems, we now turn into a comparison of performance in terms of gravimetric energy density and power density. For this, a double logarithmic Ragone-type plot is shown in Figure 5, where supercapacitors, different Li-ion based batteries such as Li-sulfur and Li-air are compared against solid state batteries.

In direct comparison to the performance values obtained for supercapacitors, achievable specific power densities are similar to solid state batteries, see Figure 5a-c. Here, asymmetric modified carbon supercapacitors achieve power densities close to 4×10^5 Wkg^{-1}, however at only moderate energy densities below 100 Whkg^{-1}[143] which is to be considered low, even towards classical liquid-based batteries to date.

Classical Li-Ion technology exemplified by a cell employing $Li_4Ti_5O_{12}$ and $LiNbO_3$-coated $LiCoO_2$ in a liquid electrolyte (Figure 5e) performing at 300 Whkg^{-1} is clearly left behind recent advances in a high temperature LGPS / LPS based solid state cell with the same electrodes,[144] as well as a graphite / LPS / LGPS system with the same cathode ($LiNbO_3$-coated $LiCoO_2$), Figure 5f-g, for the case of high temperature operation. Even electrodes with good rate capability at sufficient energy density such as modified $LiFePO_4$ in a liquid electrolyte did not exceed 10^4 Wkg^{-1} in power density.[145] In terms of specific energy density, one may note that values close to or greater than 10^3 Whkg^{-1} have been demonstrated by the use of sulfur-based cathodes[146] employing metal Lithium anode, Figure 5i-h.

Highest energy density, however at moderate power density of less than 10^4 Wkg^{-1}, could be achieved using lithium air cells, either employing a graphene structured electrode or carbon nanotubes, Figure 5j-k.[144]

In summary, solid state as a concept for future battery systems will allow for a further increase in both energy density and power density, exceeding and competing with most recent developments in Li-sulfur, Li-air and classical Li-ion technology. We therefore see a great need in a further investigation on structure-property-performance relationships of all solid state electrolytes, for which we review recent achievements on the combination with electrodes into full-cells and half-cells in the following section.
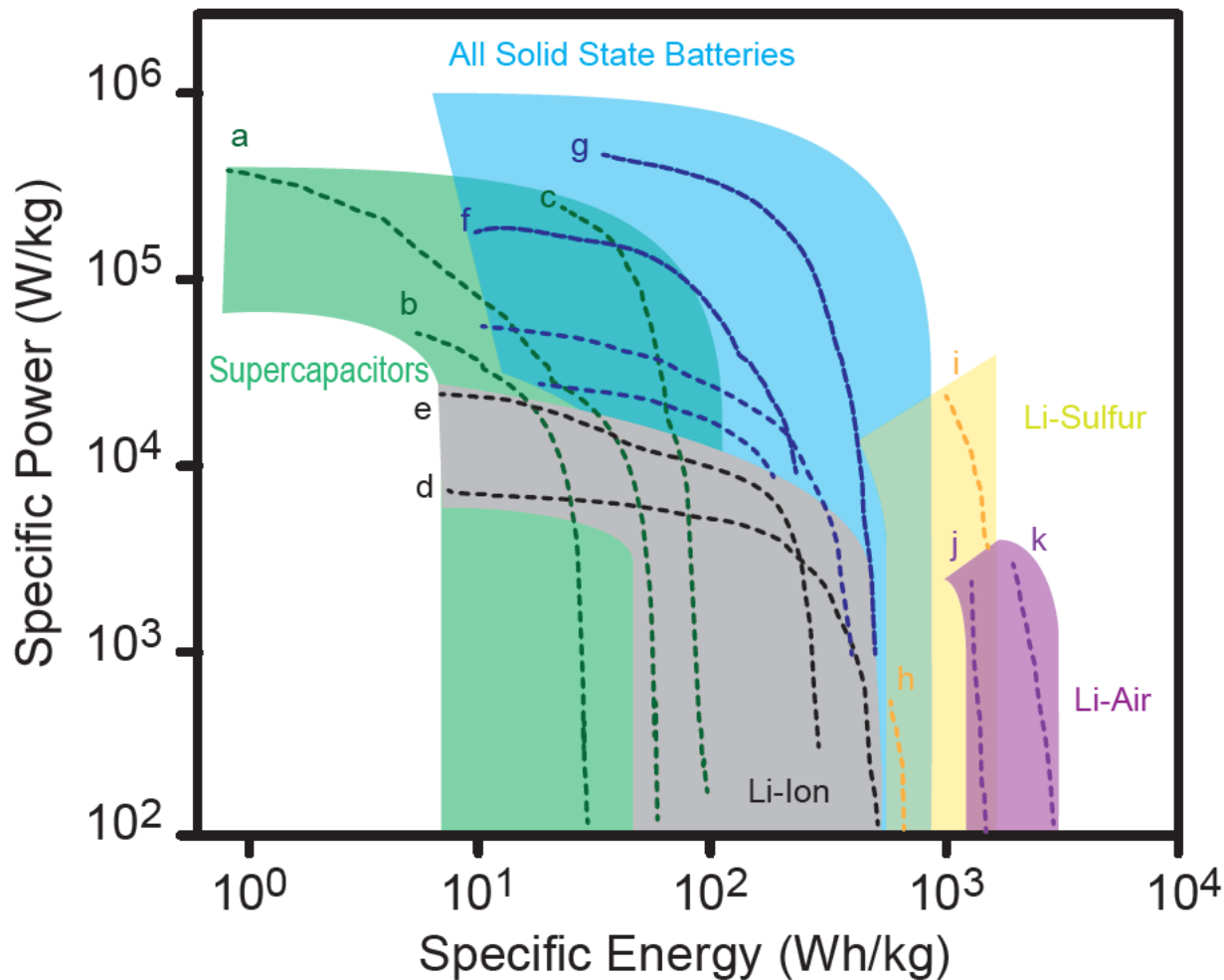
Figure 5 Ragone-type representation of specific energy vs. specific power of solid state Lithium-Ion batteries[144] (f and g) in comparison to supercapacitors,[143] (a,b and c) classical Li-ion batteries (d and e),[144,145] Li-sulfur batteries (h and i)[146] and Li-air batteries (j and k)[144] Adopted from Kato et al.[144] Short-dash lines represent room temperature operation, whereas long-dash lines were recorded at elevated temperature. Adopted from Kato et al.[144]

1.8   All Solid State Batteries based on Bulk and Thin Film Electrolytes

Batteries based on solid state electrolytes have already been combined and integrated with various low- and high-voltage electrodes. First attempts on the evaluation of compatibility usually include the application of electrode material, either as slurry, screen-printed or thin film, directly on dense, bulk ceramic bodies of electrolyte material. Half-cell testing is then usually conducted under inert atmosphere with a metallic lithium counter electrode, as far as compatibility with the latter is given.

Table 3 summarizes battery full-cells and half-cells from literature, employing the most common solid state electrolytes reviewed previously. Especially cells based on LIPON show cyclability over several thousand cycles[147,148] thereby marking the maturity of this electrolyte, which has already successfully been commercialized.[12] NASICON-type electrolytes also proofed successful transfer to microbattery architectures, achieving capacities around 100 mAh/g over several cycles.[149] Notably, Li_2S-glasses and thio-LISICON electrolytes so far only led to bulk-type reports on electrochemical cells, with no literature on microbattery integration. Here, the delicate handling of sulfur containing electrolytes due to their instability in ambient atmosphere may account for this matter. Also for perovskite-type LLTO, only few reports of actual usage in electrochemical cells have been reported. In one case, LLTO was only used as a thin coating layer, protecting a high voltage cathode in a liquid electrolyte[150] and in another report, amorphous LLTO was deposited together with $LiNi_{0.5}Mn_{1.5}O_4$ leading to a successful cycling up to 4.8 Volts.[151] In a most recent report, a $Li_{0.34}La_{0.51}TiO_3$ membrane was built with vertically aligned microchannels, leading to successful cycling at 65 °C employing a $LiFePO_4$ cathode.[152]

One may also note, that for the Li-garnet material class, no thin film based electrochemical cell was published to the best of our knowledge. The following chapter IV was motivated by that absence on a compelling strategy for electrode / electrolyte interface functionalization, for which we contribute with our own microbattery design approach.

Table 3 Review on half-cell and full-cell all solid state batteries employing the most common solid electrolyte materials.

Electrolyte	Anode	Cathode	Method	Capacity [mAh/g]	Cycles	Ref.
LIPON						
	Li metal	$LiCoO_2$	Thin film (RF-sputtering)	137	4'000	[147]
	Li metal	$LiNi_{0.5}Mn_{1.5}O_4$	Thin film (RF-sputtering)	120	10'000	[148]
NASICON-type $Li_{1.3}Al_{0.3}Ti_{1.7}(PO_4)_3$	Lithium + (LIPON buffer)	$LiCoO_2$	Thin film (RF-sputtering)	~100	50	[149]
$Li_{1.5}Al_{0.5}Ge_{1.5}(PO_4)_3$	Li metal	$LiMn_2O_4$	Thin film (RF-sputtering)	80	150	[153]
(Thio-)LISICON-type $Li_{10}GeP_2S_{12}$	Li-In	NCA	Bulk	115	100	[154]
Li_6PS_5Cl	LTO	$LiCoO_2$	Bulk	27	10	[155]
$Li_{10.05}Ge_{1.05}P_{1.95}S_{12}$	Li-In	C-sulfur	Bulk	~1500	50	[156]
Glassy sulfides $70\%Li_2S-29\%P_2S_5-1\%P_2S_3$	Li-In	$Li_4Ti_5O_{12}$ composite	Bulk	140	700	[157]
$Li_2S-P_2S_5$	Li-In	TiS_2	Bulk	~300	10	[158]
$95\%(0.6Li_2S\ 0.4SiS_2)-5\%Li_4SiO_4$	Indium	$LiCoO_2$ composite	Bulk	~70	20	[159]
$80\%Li_2S-20\%P_2S_5$	Indium	$LiCoO_2$ composite	Bulk	100	200	[160]
$75\%Li_2S$ $(25-x)P_2S_5\cdot xP_2O_5$	Li metal	$LiCoO_2$	Bulk (Mechanical milling)	109	30	[161]
$80\%Li_2S-20\%P_2S_5$	Indium	$LiMn_2O_4$		54	50	[162]
$78\%Li_2S-22\%P_2S_5$	Li-In	FeS_2	Bulk	535	50	[163]
Perovskite LLTO LLTO	Li-foil	$Li_{1.05}Ni_{0.1}Mn_{1.9}O_{3.98}F_{0.02}$	LLTO as coating	102	50	[150]
Amorphous LLTO	Li metal	$LiNi_{0.5}Mn_{1.5}O_4$	PLD thin film	N/A	50	[151]
LLTO membrane	Li/PEO	$LiFePO_4$	Slurry casting	127	50	[152]
Garnet LLZO $Li_5La_3Ta_2O_{12}$	Li metal	$LiCoO_2$	Bulk	83	N/A	[164]
Al-doped LLZO	Molten Li metal	$Cu_{0.1}V_2O_5$	Bulk	~10	5	[165]
$Li_{6.75}La_3Nb_{0.25}O_{12}$	Li metal	$LiCoO_2$	Bulk	129	100	[166]

1.9   All Solid State Batteries based on Garnet $Li_7La_3Zr_2O_{12}$

Li-garnet $Li_7La_3Zr_2O_{12}$-based structures[127] (LLZO) are of notable interest for the following chapters of this thesis. With up to 1.4×10^{-3} Scm^{-1} at room temperature Li$^+$-ion conduction for the case of iron-doped LLZO,[74] and experimental stability towards metallic lithium, Li-garnet electrolytes are one of the most promising inorganic Li$^+$ conductors at hand. As reviewed in the previous sections, a combination of several key properties such as sufficient ionic conductivity, a wide electrochemical stability window as well as suitable methods for bulk to thin film transfer are all within reach for this material.

LLZO in the form of powders as well as bulk pellets of high density seem fairly well understood nowadays. Several reports, such as sintering optimization studies on various dopants,[81,167] conductivity as well as density optimization as a function of dopant concentration,[168,169] reports on high Li-ion conductivity,[72,79,80,170] achieved through doping with Tantalum leading to 0.87 mScm^{-1}, viz. Gallium doping with 0.35 mScm^{-1} are accessible.

Despite those promising achievements in terms of cell performance reached for *bulk* LLZO as a solid state electrolyte, the transfer of the beneficial material properties (such as high Li-ion conductivity and crystallographic phase) to *thin films* have so far been challenging. Several attempts of thin film deposition, by either RF-sputtering,[171–173] CVD,[137,174] ALD,[175] sol-gel deposition[135,176] as well as PLD[134,136,177–179] have been conducted for LZZO so far. A majority of reported films show room temperature Li-ion conductivities in the order of 1×10^{-8} Scm^{-1} to 1×10^{-6} Scm^{-1}, remaining at least 3 to 5 orders of magnitude below the bulk pellet values and leaving those thin films far behind LZZO electrolytes processed through classic particle synthesis and sintering at higher temperatures and pressures. Notably, at around 600 °C LLZO thin films exhibit a phase change from amorphous to crystalline, however, with no clear trend on whether high crystallinity is also a necessity for high room temperature conductivity. One may also note that PLD deposition, followed by RF-sputtering so far achieved highest conductivity in thin film form of LLZO in the latter case reached by Li_2O / LLZO / Ga_2O_3 co-deposition by RF magnetron-sputtering reaching 1.6×10^{-5} Scm^{-1}, Rawlence et al.[126]. Methods that were sol-gel based, reached so far a maximum of 2.4×10^{-6} Scm^{-1} employing Aluminum-doped LLZO on MgO substrates.[135] In the case of CVD deposition, the highest report in terms of conductivity was reported by Loho et al.[137] with 4.2×10^{-6} Scm^{-1} employing a CO_2 laser

assisted growth method. Reports from Lobe et al.[173] regarding films prepared by RF-sputtering show also high conductivity of 1.2×10^{-4} Scm^{-1}. The use of an electronically conductive substrate in this work leaves, however, some questions on the interpretation of measured values for in-plane conductivity and for this reason this work has not been taken into account.

In conclusion, even though > 10 years of research have passed since the initial discovery of the high lithium conductivity in garnet LLZO, processing remains to be explored, turning from classic pellets or tapes of several mm to almost 100 microns in thickness down to hundreds of nanometer electrolyte thickness. In essence, the phase evolution and lithiation degree are affected by the processing choice and differ for film processing towards classic powder and sinter densification of macro-scaled functional LZZO ceramics. Analyzing the field, it is also evident that phase evolution studies for LLZO thin films are still scarce.[126] Vacuum based processing of LZZO thin films gives opportunity for substantially reduced final thicknesses; we see here value in PLD processing by acting as a model system for further thin film understanding of this material class. Till date, the stabilization of the highly conductive cubic phase of LLZO in thin film form by PLD remains unresolved and requires attention.

1. Aim and Outline of the Thesis

In the following chapters, we explore the different aspects of Li-garnet electrolyte, their compatibility with different electrode materials, as well as the stabilization of the highly conductive cubic phase in the form of thin films. We contribute with a work on a fully thin film based microbattery, employing garnet electrolytes, and show the feasibility of nanoscopic microbatteries for full CMOS-integration into future mobile sensing and measuring devices for portable electronics.

Part II aims at the compatibility of *thin film anodes* with Li-garnet electrolytes. For this, $Li_4Ti_5O_{12}$ was selected as a model anode, due to its favorable zero-strain characteristics upon lithiation / delithiation and its well-understood behavior in liquid-based cells. In a first step, 80 nm thin films of $Li_4Ti_5O_{12}$ were grown by pulsed laser deposition (PLD) and structurally and electrochemically characterized. In a second step, the same thin film was grown directly on top of a cubic garnet bulk pellet $Li_{6.25}Al_{0.25}La_3Zr_2O_{12}$ followed by structural and electrochemical characterization. Finally, a half-cell, combining a thin film of $Li_4Ti_5O_{12}$ and a metallic lithium reference electrode on the other side of the LLZO pellet, was assembled inside an Ar-filled glovebox, followed by galvanostatic cycling at room temperature. Notably, the presented work represents the first thin film anode combined with Li-garnets to the field, and also marks the first time, the $Li_4Ti_5O_{12}$ / $Li_{6.25}Al_{0.25}La_3Zr_2O_{12}$ system could be cycled at room temperature. Rate capability testing on the half-cell was performed at three different rates and capacity retention over 22 cycles was assessed.

Part III focuses on the effect of nitrides on the formation of the cubic phase for thin films of $Li_{6.25}Al_{0.25}La_3Zr_2O_{12}$. Inspired by successes, achieved with the nitride anode (see chapter IV), a multilayered system consisting of 9 repeating layers of Li_3N and $Li_{6.25}Al_{0.25}La_3Zr_2O_{12}$, deposited on MgO substrates, was chosen as a model system to investigate the effect of different thermal treatment on structure, phase and transport properties of thin film $Li_{6.25}Al_{0.25}La_3Zr_2O_{12}$. Here, two different strategies where established to form the cubic phase of $Li_{6.25}Al_{0.25}La_3Zr_2O_{12}$ in thin film form deposited by pulsed laser deposition. Firstly, by a deposition at 300 °C followed by an external post-annealing step, and secondly, by direct deposition under high vacuum at a temperature of 660 °C. Both strategies could be shown to lead to dense and crack-free thin film of cubic LLZO. Ex-situ as well as in-situ Raman

spectroscopy allowed to track the crystallographic phase evolution in the temperature range from 300 °C to 980 °C. Under optimal annealing conditions, world record room temperature Li-conductivity of $2.9(5) \times 10^{-5}$ Scm^{-1} could be achieved for films < 1 μm, contributing to the ongoing effort in downscaling of all solid state microbatteries and lithiated thin films, preserving high ionic conductivity.

In *Part IV*, we extend the knowledge gained on the electrode / garnet-electrolyte interface to construct a fully thin film microbattery. Here, we combined $LiNi_{0.8}Co_{0.15}Al_{0.05}O_2$ cathode, garnet $Li_{6.25}Al_{0.25}La_3Zr_2O_{12}$ electrolyte together with the uncommon anode Li_7MnN_4. Prior to assembly, all the thin film components were investigated separately by Raman spectroscopy, Scanning Electron Microscopy (SEM) as well as Electrical Impedance Spectroscopy (EIS). With a total cell thickness of less than 1 μm and a total area of ~0.01 cm^2, the microbattery presented in this chapter represents a first all thin film microbattery based on Li-garnets.

Part V can be regarded as a toolbox, a computer code developed to assist the novel type of measurements for microbatteries, for which commercial system did not offer appropriate resolution and accuracy. In this regard, a novel open source software kit with more than 10'000 lines of code was written from scratch during the course of this thesis, with extended testing functionality, ranging from memristor-testing in cyclic voltammetry (CV), chronoamperometry as well as pulsed logic testing. Microbattery cells and on-chip integrated energy storage components could be assessed in performance in a current range of down to 10 nA in galvanostatic mode, a range which was previously not accessible by commercial battery testing equipment. With this new toolkit, high accuracy cycling at low rates – even for thin film cells – could be achieved, helping the development and understanding of electrode / Li-garnet electrolyte compatibility. The software functionality extends also to testing of memristive devices including cyclic voltammetry (CV), chronoamperometry as well as pulsed transient measurements. In addition, various electrochemical experimental procedures were automatized. This includes the measurement of Arrhenius-type conductivity through electrochemical impedance spectroscopy, control of gas flows and temperature ramps as well as micropositioner maneuvering.

Part VI provides a summary and an overall conclusion on the following thesis, rounded off by an outlook section on follow up research directions one may consider for a successful continuation of this work.

PART II: Lithium Titanate Anode Thin Films for Li-Ion Solid State Battery based on Garnets

This thesis chapter was published as an original research paper entitled:

Lithium Titanate Anode Thin Films for Li-Ion Solid State Battery Based on Garnets

Pfenninger Reto, Afyon Semih, Garbayo Inigo, Struzik Michal, Rupp Jennifer .L.M.

2 Abstract

Solid state electrolytes, such as Li-Garnets, are fastest Li-ionic conductor materials that have attracted attention for safe hybrid and full solid state battery architectures. Turning to oxide based low voltage anodes gives opportunities to avoid Li-dendrite formation and also to reach full thin film microbattery architectures based on garnets as high energy density replacement for supercapacitors. Herein, we demonstrate that $Li_4Ti_5O_{12}$ thin films deposited by pulsed laser deposition can show stable structures and cycling kinetics reaching almost close to theoretical capacity of 175 mAh/g when combined to $Li_{6.25}Al_{0.25}La_3Zr_2O_{12}$ pellets. Stable operation at room temperature with 90 % of theoretical capacity retention at 2.5 mA/g over 22 cycles was achieved on bilayer half cell batteries. Rate capability studies show promising charge and discharge capacities and act as a case study for the well-known $Li_4Ti_5O_{12}$ thin film anode, demonstrating its good compatibility with the investigated solid garnet electrolyte. This gives new perspective on the use of oxide-based low voltage anodes for future strategies avoiding Li-dendrite formation or safe solid state microbattery thin film assemblies based on Li-garnets.

2   Introduction

Next generation energy storage technologies for stationary and mobile electronics rely on materials and devices with high gravimetric and volumetric capacity.[180] Safety aspects such as operation in rough environments and at a widened temperature window maintaining the device material structures are also equally important.[181] Here, all solid state batteries are promising, since they show superior chemical stability, better packaging[142,182] and improved safety (i.e. no inflammable liquids[18]). In addition, one may even use the opportunity to gain higher endurance during operation and option to work at high temperatures to further enhance its Li diffusion kinetics. Latter is attractive if we consider integrating solid state battery components as future integrated circuit components co-operating and managing waste heat for chip architectures[183] in the internet of things or simply for industrial large-scale power management.

Considering the scalability, ceramic all solid state battery constituents are easily transferrable to thin film microbattery architectures[184,185] for powering of portable electronics and chip units such as sensors or actuators. Recent reports show clear potential to surge forward to replace supercapacitor structures.[186] This is on the one hand due to the high inherent energy densities of solid microbatteries, which can omit by their nature classic packaging requirements and, also minimize electrode distances by the employment of thin film processing of the components by 2 to 3 orders of magnitude.[31,187,188] Comparing state-of-the-art performances, up to $7.4 \, mWcm^{-2}\mu m^{-1}$ can currently be reached as recently demonstrated by Lewis group for a $NiSn/LiMnO_2$-based hybrid microbattery showing high potential, but still including a liquid type electrolyte.[184,186] Now, using solid state thin film techniques classic liquid and polymer separators can be eliminated for a simplified structure, whereby high packaging density and safety are improved and Li diffusion length is shortened due to its tenth of nanometer in film thickness, as demonstrated by the Van Notten group.[142]

Looking at feasible all-solid state electrolytes, it becomes apparent that several requirements on such materials are desired, among which high lithium ionic conductivity, the temperature

and mechanical stability, and chemical stability vs. metallic Lithium are equally important. Among the different all-solid state electrolytes available today[48] (e.g. NASICON,[39,44,189] LISICON[45,50,190] or LIPON[191]) cubic garnet $Li_7La_3Zr_2O_{12}$-based structures[127] are of particular interest. Firstly reported by Weppner et al.,[70] $Li_7La_3Zr_2O_{12}$ (LLZO) with fast Li^+-conduction of up to 1 mScm^{-1} has been demonstrated at room temperature[127] that positions the garnets as one of the highest solid state inorganic Li^+ conductors available. $Li_7La_3Zr_2O_{12}$ exhibits two different crystallographic phases, a low conductive tetragonal phase and a high conductive cubic phase, as firstly described by Awaka et al.[75,76] However, the stabilization of the cubic $Li_7La_3Zr_2O_{12}$ phase at room temperature is challenging, as is its processing to dense ceramic pellets due to Li-losses at elevated temperatures.[168,192] Different attempts to stabilize these structures by doping on either the Li-site (Ga^{3+} and Al^{3+}),[78–80] the La-site (Nd^{3+}, Sr^{2+})[70,82,193] or the Zr-site (mainly Ta^{5+})[72,94] have been successful. Among the highest Li conductivities and stable structures have been achieved through, doping on the Li-site with Al^{3+},[80,88,194] which we will depict through this study as the solid state electrolyte material of choice. Furthermore, transferability to thin film form has been shown to be challenging and is not yet fully understood, leaving a lot of room for improvement to the field, thus giving reasons to the importance of understanding electrode interactions and battery performance starting from bulk pellet-based model systems first.

From an electrode perspective, all solid state batteries have the potential to integrate new and mostly unexplored high capacity and energy electrode materials such as vanadate-based[195] or sulfur[196]-based composites which show conventionally a low stability in standard liquid or polymer based Li-ion batteries for long term cycling. Despite the progress on LLZO as a solid state electrolyte, only a few systematic studies have been conducted on the combination of electrodes with garnet-type $Li_7La_3Zr_2O_{12}$ electrolytes, so far; viz. the chemical stability and operation conditions of full LLZO-based battery cells are still under discussion.[197] Previously, main focus in the field has been set on pulsed laser deposition (PLD) and investigation of *cathodes* for Li-garnet electrolytes: i.e. $LiCoO_2$ cathodes, see Asaoka group, reporting capacities of 130 mAh/g with cycling stability challenges.[71,166,198,199] Very recently, first oxide-based *anodes* of $Li_4Ti_5O_{12}$ were fused with Li-garnets and successfully cycled as stable solid state batteries based on cost-effective ceramic processing by Van den Broek et al.[169] Apart from this, there is only one additional literature report on Al-doped $Li_7La_3Zr_2O_{12}$ electrolyte in a battery assembly with $Li_4Ti_5O_{12}$ and $LiMn_2O_4$ by Jin and Mc Ginn.[200] In

general, the anode material $Li_4Ti_5O_{12}$ crystallizes with space group Fd-3m and was shown to be a mechanically very stable battery-anode material for tests upon standard liquid electrolytes. With 175 mAh/g theoretical capacity,[201] $Li_4Ti_5O_{12}$ remains moderate with an average voltage of ca. 1.5 V vs. Li when tested in liquid electrolyte-based Li-ion batteries.[202] However, fast discharge rates,[203] a flat voltage profile[204] at around 1.5 V and very similar lattice parameters of the fully delithiated phase $Li_4Ti_5O_{12}$ and the lithiated phase $Li_7Ti_5O_{12}$ give rise to very low lattice strain upon cycling which is attractive to manage the chemo-mechanics.[205] The latter is particularly important in the case of all solid state batteries, since induced strain due to large volume expansion during lithiation/delithiation is one of the main causes of cracks, delamination and poor battery performances potentially restricting lifetime for all-solid batteries. Here ceramic processing strategies to form strong interfacial bonds between the electrolyte and the electrode are needed, as is the electrochemical study of the material interface $Li_4Ti_5O_{12}$ anode / $Li_7La_3Zr_2O_{12}$ electrolyte. One challenge that needs to be addressed particularly for future microbattery integration of Li-garnets is the processing of $Li_4Ti_5O_{12}$ in the form of thin films. In this regard, several attempts have also been taken already to deposit $Li_4Ti_5O_{12}$ as thin films either by RF-sputtering,[206] sol-gel method[207] or pulsed laser deposition (PLD)[208–210] on classic Li-electrolytes such as quartz, oriented Al_2O_3, $MgAl_2O_4$ or coated silicon substrates. Testing in liquid-based electrolytes have usually shown capacities around 90 % of the theoretical maximum.[208] It remains open at this point whether nano-grained $Li_4Ti_5O_{12}$ films are electrochemically stable towards Li-garnets in terms of their interface. Recent progress of Van den Broek et al.[169] does confirm high stability for micron-sized thicknesses of ~40-50 μm slurry-coated layers when combined with Li-garnet bulk pellets. However, at the thin film level, the nanoscopic grain structures and high grain boundary volumes may lead to differed Li-ionic transfer and capacities,[211,212] which are to be explored, in particular in very low C-rate cycling with careful focus on the observable oxidation and reduction reactions. Besides, it is known that strain effects can strongly be imposed when turning to thin film, which can alter even the interfacial impedance characteristics towards a solid electrolyte and can vary the ionic transfer over orders of magnitude.[213,214] Despite the effort of the transfer, all-solid-batteries of Li-garnet structures with thin films of the anode material $Li_4Ti_5O_{12}$ still have to be constructed and tested thoroughly. It remains even unclear from previous reports, whether such interfaces of pellet-$Li_7La_3Zr_2O_{12}$ / anode-$Li_4Ti_5O_{12}$ electrode are stable, for which thin film structures are viable objects of study. The implication of these investigations would further allow to judge on the potential of $Li_4Ti_5O_{12}$ material as an alternative to pure Li anodes in safe and large-scale ceramic batteries with extended

temperature window, but also as thin-film anode material for future microbattery architectures. In addition, we rate the exploration of alternative anodes for Li-garnet solid state electrolytes as significant as also recent reports of Aguesse et al.[23] revealed that the employment of pure lithium may lead to short circuiting by Li dendritic growth upon prolonged cycling. From a general materials perspective, one may learn deeply from the anode-application use of $Li_4Ti_5O_{12}$ as it has been studied extensively in the field of liquid electrolyte-based batteries[204,215–217] and hybrid cell microbattery applications,[184] for example, where $Li_4Ti_5O_{12}$ has been 3D printed on a glassy substrate immersed in a liquid electrolyte. In essence, we see a huge prospect for integration and novel battery cells combining the $Li_4Ti_5O_{12}$ in the form of thin films to Li-garnets as model structures to understand the interface stability and electrochemistry for large-scale battery storage and particularly in the area of thin film microbatteries.

Through this work, we demonstrate the fabrication and investigate all solid state Li-ion batteries combining the anode material $Li_4Ti_5O_{12}$ in the form of thin films with the Li-garnet electrolyte c-$Li_{6.25}Al_{0.25}La_3Zr_2O_{12}$. We show composition control and deposition of dense and crack-free $Li_4Ti_5O_{12}$ thin films on Li-garnet pellets, as well as on single crystalline substrates such as MgO. We probe the near order vibrational characteristics and confirm their phase stability when deposited as thin films via Raman spectroscopy. Electrochemical impedance spectroscopic techniques were employed to investigate the impedances relative to the nanostructure and phase for the anode thin films of $Li_4Ti_5O_{12}$. Eventually, we probe the lithium dynamics in charging and discharging, as well as its incorporation to $Li_4Ti_5O_{12}$ electrodes in combination with the Li-garnet electrolyte, studying the development of cell potential and capacity with respect to (dis)charge rates towards Li counter electrode. Ultimately, we conclude on the potential of lithium titanate anodes as future electrodes for Li-garnet electrolytes, discuss their stability as solid-solid interfaces for large-scale storage and microbattery applications.

2   Experimental

2.1   Material Synthesis of the Li-Garnet Electrolyte Pellet Substrates

$Li_{6.25}Al_{0.25}La_3Zr_2O_{12}$ powder was synthesized and dense pellets were prepared from it based on the methods shown by Van den Broek et al. in Ref.[169] Stable sols were obtained by dissolving stoichiometric amounts of $LiNO_3$ (99.99 %, Merck), $La(NO_3)_3(H2O)_6$ (99.9 %, Alfa Aesar), and zirconium(IV) 2,4-pentanedionate (Alfa Aesar) in a water and ethanol mixture which were fired at 600-650 °C after drying. After uniaxial as well as isostatic pressing (440 bar for 3 min) sintering took place at 1050 °C for 12 hours. Sintered pellets of 11 mm in diameter were obtained and all showed > 85 % of theoretical density and initial thicknesses of around 1.2 mm. They were polished equally on both sides to < 600 μm.

The corresponding reference materials for Raman analysis $Li_4Ti_5O_{12}$ (> 99 % Aldrich) TiO_2 (rutile, 99.5 % Aldrich) as well as TiO_2 (anatase, 99.7 % Aldrich) were delivered from Aldrich and used as received.

2.2   Thin Film Processing of $Li_4Ti_5O_{12}$ Anodes

We first turn to the processing of a suitable target for $Li_4Ti_5O_{12}$ to deposit in Pulsed Laser Deposition eventually the films. For this, dense $Li_4Ti_5O_{12}$ pellets were sintered for their use as target in pulsed laser deposition (PLD). In accordance, $Li_4Ti_5O_{12}$ (Sigma Aldrich, > 99 % purity) and Li_2O (Alfa Aesar, 99.5 % purity) were used as initial precursors in the adequate amount to match a final nominal stoichiometry of $Li_{7.1}Ti_5O_{12}$. A solid state route was used for the synthesis, for which the powders were first mixed under inert atmosphere inside an Ar-filled glovebox and grounded in an agate mortar and then calcined at 850 °C for 12 hrs. Reground powder was pressed into pellets, then uniaxially pressed followed by cold isostatic pressing (440 bar for 2 min) and sintered in an alumina-tube-furnace under constant flow of 30 sccm O_2. The sintering was conducted at 1000 °C for 12 h with heating and cooling ramp

rates of 5 °C/min. With this, pellets with 82 % relative densities were achieved. Pellets were then stored in an argon-filled glovebox to avoid exposure to CO_2 and humidity and their surface polished thoroughly prior their use as targets for pulsed laser thin film deposition.

Eventually, we used the fabricated targets to deposit thin films of $Li_4Ti_5O_{12}$ by means of pulsed laser deposition. The deposition equipment (PLD, Surface, Germany) was equipped with a KrF excimer laser of 248 nm wavelength and films were deposited at a frequency of 10 Hz with a target to substrate distance of 70 mm and background pressures of 13 mTorr O_2. The temperature of the substrate was kept constant at 500 °C during thin film growth. Two different substrates were used for thin film deposition in this study: First, (001) oriented MgO substrates (Crystec, Germany) were used for thin film structural and electrochemical analysis. Then, $Li_4Ti_5O_{12}$ films were grown on top of the $Li_{6.25}Al_{0.25}La_3Zr_2O_{12}$ electrolyte pellets, for building and testing all solid state Li-ion cells. In all of the cases, the resulting thickness of the thin film was adjusted by the number of laser shots applied, extrapolating linearly from measured growth rates by profilometry (Bruker Dektak, USA).

2.3 Electrolyte $Li_{6.25}Al_{0.25}La_3Zr_2O_{12}$ Pellet and Anode $Li_4Ti_5O_{12}$ Thin Film Structural Characterization

$Li_{7.1}Ti_5O_{12}$ pellets as well as $Li_{6.25}Al_{0.25}La_3Zr_2O_{12}$ electrolyte pellets were characterized by X-Ray diffraction (XRD, Bruker D8, USA) with Cu K_α Microstructure of the deposited thin films were investigated by scanning electron microscopy (SEM, Leo 1530, Germany). Raman spectroscopy at 10 mW power and 532 nm wavelength to ensure low required penetration depth (WiTec, Germany, spectral resolution of 0.7 cm^{-1}) was used for near order structural analysis.

2.4 Electrochemical Characterization of Thin Films and All Solid State Cells

Electrical impedance spectroscopy was performed for electrochemical analysis of the fabricated thin films. An in-plane geometry was used, with 100 nm thick electron beam evaporated platinum electrodes of lateral dimensions of 3.25×0.5 mm, separated 0.25 mm (Plassys MEB 550, France) - see inset picture in Figure 6c. An impedance measurement device

(Zahner IM6, Germany) was attached to a heated Linkam stage (Linkam Scientific, UK) and the respective Nyquist data in the frequency range of 1 Hz to 1 MHz was analyzed with ZView 3.4f and OriginPro 9.1. In order to measure Arrhenius activation energies of thin films, samples were heated between 50 °C to 400 °C under synthetic air flow of 50 sccm. At each temperature, samples were stabilized for several minutes to assure an equilibrium was reached before any measurements took place.

Battery cells of the $Li_{6.25}Al_{0.25}La_3Zr_2O_{12}$ pellets with $Li_4Ti_5O_{12}$ thin films deposited on one side were then built. The complete cell was built by depositing 100 nm of copper (Plassys MEB 550, France) on top of the $Li_4Ti_5O_{12}$ thin film working electrode for current collection and pressing a Li-metal foil on the backside of the pellet acting as the reference and counter electrode. Prior to press-contacting of the Li-metal, both the pellet and the Li-foil were polished thoroughly to remove any resistive Li_2CO_3 (which is prone to form on $Li_{6.25}Al_{0.25}La_3Zr_2O_{12}$ pellets),[218] as well as traces on the surface of the Li-metal. All cell construction experiments were carried out inside an Ar-filled glovebox. In order to maintain good contact between the Li-foil and the pellet, a ceramic disc of 5 mm diameter has been used to firmly press the pellet to the Li-foil and ensure good contact. The cell geometry and design can be seen in Figure 8a. Electrical contacts were done through tungsten needle contacts placed directly on top of the Li-foil and the platinum or copper top contact, respectively.

Galvanostatic cycling was carried out inside the glovebox with a source measurement unit (Keithley 2602B, USA) with own written code (Python)[219] and took place between 1.0 V and 2.6 V. Measurements were carried out at room temperature. The applied current rate for the following galvanostatic cycling was calculated with the assumption of a dense, homogeneously flat thin film of constant thickness of 80 nm. Rates between 2.5 mA/g and 25 mA/g were applied. The effective area of active electrode which was broken away was kept minimal and the new geometry of the cell was measured by top view microscopy image and ImageJ was used to assess the new surface area with high accuracy.

2   Results and Discussion

2.5   Thin Films of $Li_4Ti_5O_{12}$ Anodes on MgO Substrates

We first turn to the investigation of the anode $Li_4Ti_5O_{12}$ thin film microstructure and its crystallinity after PLD deposition on MgO substrates. Figure 6a, displays the cross sectional SEM image of a thin film deposition of lithium titanate of roughly 80 nm ± 5 nm in thickness deposited on an electrolyte pellet. A continuous, flat and dense microstructure was observed for the $Li_4Ti_5O_{12}$ anode films forming a sharp interface after deposition towards the $Li_{6.25}Al_{0.25}La_3Zr_2O_{12}$ pellet electrolyte. (Lower magnification SEM images of the electrolyte pellet as well as the thin film grown on the electrolyte can be found in Supporting Figure S4 and Supporting Figure S5, respectively). Microstructure of the $Li_4Ti_5O_{12}$ films reveals tendency of slightly columnar grain growth. We use Raman spectroscopy as well as XRD (Supporting Figure S1) to analyze the phase constituents of the $Li_4Ti_5O_{12}$ film, Figure 6b. Herein, Raman spectrum of the thin film is compared versus the respective powder reference data for $Li_4Ti_5O_{12}$ powder and to the overlithiated $Li_{7.1}Ti_5O_{12}$ PLD target in use. In general, three main Raman active bands can be observed for pure $Li_4Ti_5O_{12}$ positioned at 671, 421 and 231 cm^{-1} corresponding to the symmetric stretching vibration mode A_{1g} of the Ti-O bond, the asymmetric stretching mode E_g of the Li-O bond and the bending vibration mode F_{2g} of the Ti-O, respectively. These are well distinguished in the deposited LTO films, whose spectra match perfectly with the reference powder, thus confirming the formation of the spinel $Li_4Ti_5O_{12}$ in the films as deposited from the overlithiated $Li_{7.1}Ti_5O_{12}$ target. We also note additional Raman vibrations at ~300 cm^{-1} and peak splitting are around 421 cm^{-1} which are ascribed to Li-vibrations occurring from the strong overlithiation for the pellet target, this is in line with previous pellet-based reports from literature.[220–222]
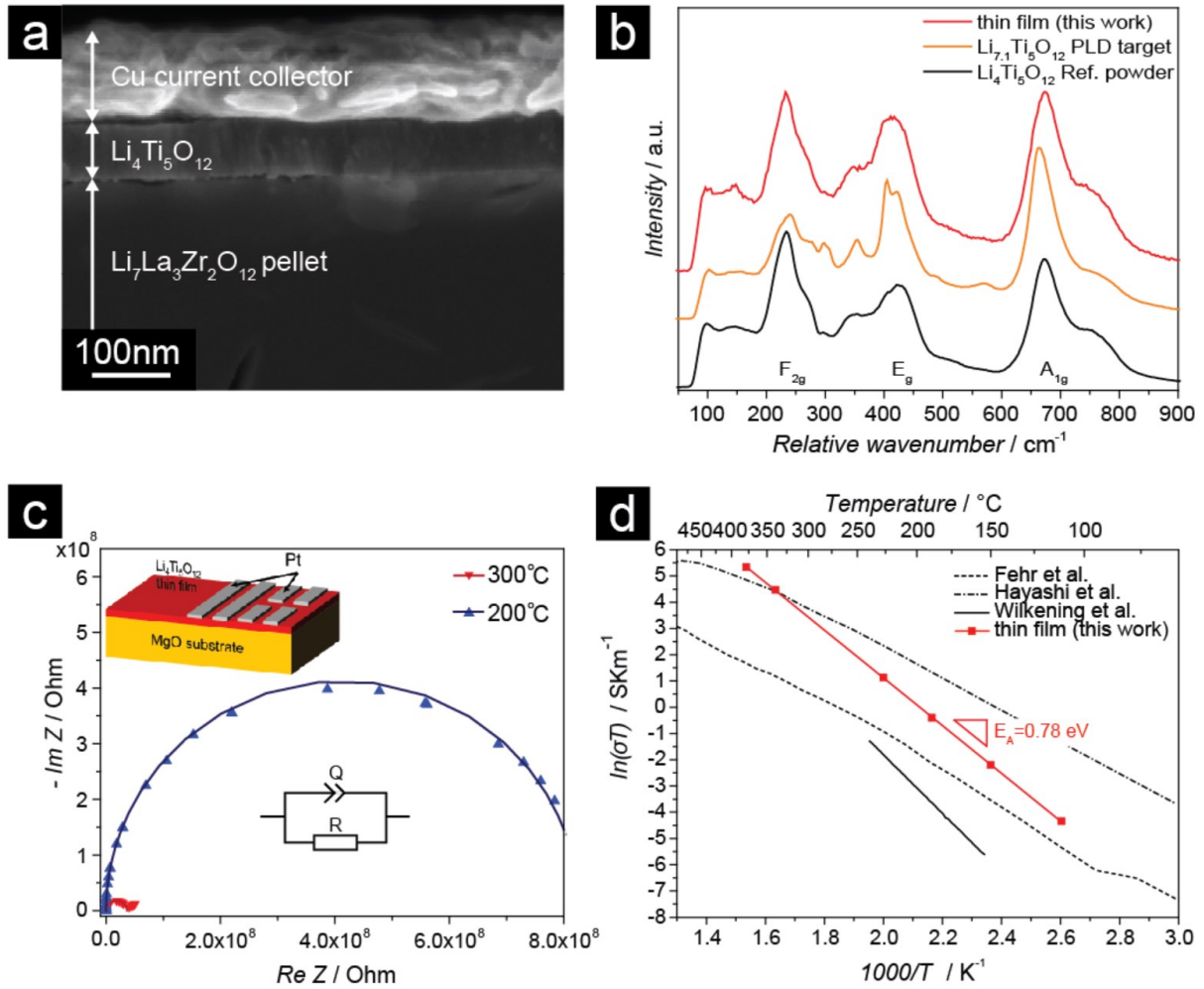
Figure 6 a) Cross-sectional SEM image of a Li₄Ti₅O₁₂ thin film deposited by pulsed laser deposition on an electrolyte substrate. b) Raman spectra of thin film of Li₄Ti₅O₁₂ deposited on MgO recorded with 10 mW power and 532 nm wavelength and comparison to powder reference patterns (Li₄Ti₅O₁₂) as well as overlithiated PLD target (Li₇.₁Ti₅O₁₂). c) Nyquist plot of impedance measured in in-plane geometry with platinum top contacts at 200 °C and 300 °C respectively (dots) and fitting according to a resistive element in parallel with a constant-phase-element. (lines) d) Arrhenius-Plot of Li₄Ti₅O₁₂ thin film on MgO. The thin film is compared towards literature references obtained from Li₄Ti₅O₁₂ pellets. The activation energy of 0.78 eV is in line with pellet dc-conductivity, as well as SAE-NMR reported in literature.[223–225]

To study the implication on the Li-transfer of the deposited film to the MgO substrate, we now turn to electrochemical impedance spectroscopy probing the Li-ionic transport kinetics. Figure 6c shows an example of two impedance spectra acquired in the deposited films with zero bias at two selected measuring temperatures, being 200 °C and 300 °C. The in-plane measuring configuration with top rectangular platinum electrodes is depicted as an inset of Fig 1c. Analyzing the Nyquist plot, we confirm a clear semicircle for the impedance at high frequencies with an additional tail attributed to the platinum blocking electrodes (see Supporting Figure S2) based on frequency comparison and literature. Impedance characteristics of the system shown in this geometry contain contributions from both majority ionic as well as potential minority electronic transport. The first semicircle was therefore attributed to the thin film and fitted to an equivalent circuit model of a resistor in parallel with a constant-phase-element. We employ the resistance fitted by the equivalent circuit model for the $Li_4Ti_5O_{12}$ thin film to study the Arrhenius behavior of conductivity. In Figure 6d, the thin film of $Li_4Ti_5O_{12}$ grown on (001) MgO is compared to literature of spinel $Li_4Ti_5O_{12}$ bulk pellet.[223,224] Both, the measured activation energy of 0.78 eV and the calculated conductivity are in agreement with values obtained in literature for $Li_4Ti_5O_{12}$ pellets such as of Wilkening et al., which also shows some spread.[223,224] We find a one to two orders of magnitude lowered conductivity measured for the nanocrystalline $Li_4Ti_5O_{12}$ thin films, when compared to the macrocrystalline bulk pellets. However, it is important to highlight here that transfer from microcrystalline pellets to nanocrystalline thin film often lowers conductivity due to the changed grain-to-grain boundary volume ratio, see i.e. Ref.[226] This is also a known phenomenon in other classes of oxides.[179,227,228]

Based on the results obtained from this thin film processing and structural analysis we confirm for $Li_4Ti_5O_{12}$ on MgO that dense $Li_4Ti_5O_{12}$ thin films can be deposited in the desired phase of spinel $Li_4Ti_5O_{12}$ and can now be grown on $Li_{6.25}Al_{0.25}La_3Zr_2O_{12}$ electrolyte ceramic pellets to be investigated as all solid state battery assembly in the following.

2.6 Thin Films of $Li_4Ti_5O_{12}$ on Li-Garnet $Li_{6.25}Al_{0.25}La_3Zr_2O_{12}$ Substrates for Pellet Based Battery Assemblies

We now turn to the battery assembly for which $Li_4Ti_5O_{12}$ films were grown by PLD on home-made dense $Li_{6.25}Al_{0.25}La_3Zr_2O_{12}$ pellets. The microstructure of $Li_4Ti_5O_{12}$ films deposited on the electrolyte pellets, Figure 7a, which was investigated by SEM and is displayed in Figure 7b-d. The top-view of the polished electrolyte pellet surface with PLD-deposited $Li_4Ti_5O_{12}$ thin film on top exhibits homogeneously flat and continuous microstructure for the thin film anode, Figure 7c, opposed to that of a fresh polished pellet surface without thin film, Figure 7b. It is assumed that the particle agglomerates in that image formed during exposure of the pellet to ambient atmosphere. Since $Li_7La_3Zr_2O_{12}$ is known for reacting with humidity and CO_2, to form Li_2CO_3[218,229] on the surface of the pellet without $Li_4Ti_5O_{12}$ coating, as observed also by other investigators[78]. In Figure 7d, cross-sectional SEM has been performed on the anode film/electrolyte pellet interface before battery cycling.
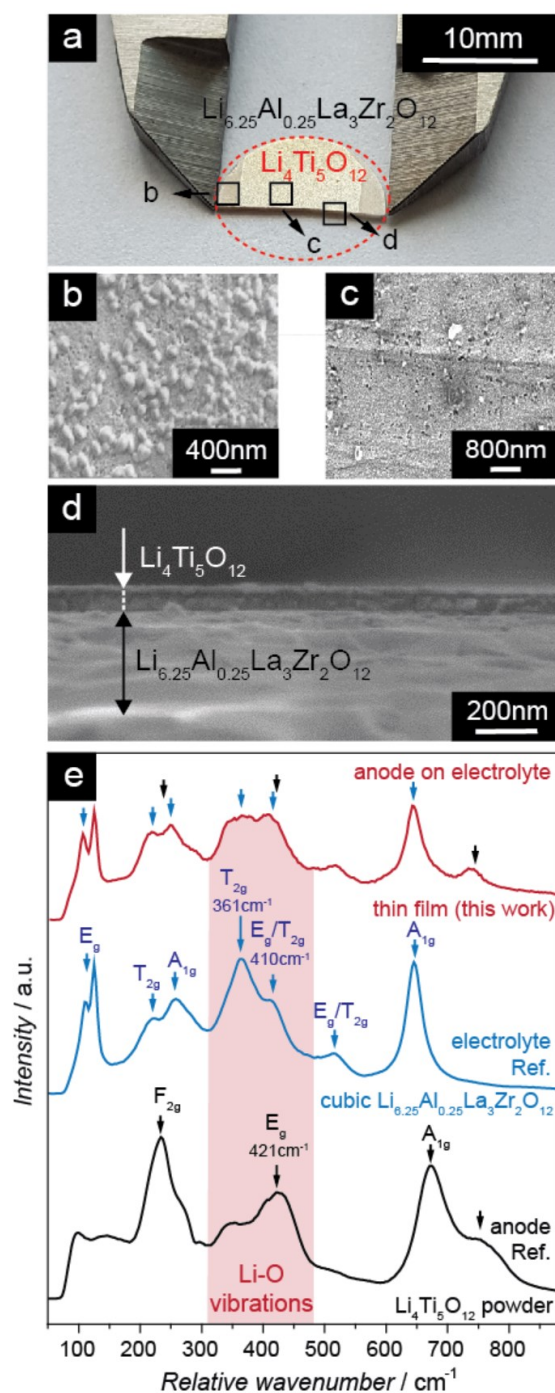
Figure 7 a) Optical image of $Li_{6.25}Al_{0.25}La_3Zr_2O_{12}$ pellet with thin film of $Li_4Ti_5O_{12}$ on top. b-c) SEM images of the surface morphologies at different magnifications. d) Cross-sectional SEM image of the $Li_{6.25}Al_{0.25}La_3Zr_2O_{12}$ / $Li_4Ti_5O_{12}$ heterostructure. e) Raman spectra recorded with 10 mW power and 532 nm wavelength of the respective thin film / target and comparison to powder reference patterns recorded in our lab ($Li_4Ti_5O_{12}$).

In Fig 2e, the Raman spectra of the battery half-cell comprised of $Li_4Ti_5O_{12}$ thin film deposited on the $Li_{6.25}Al_{0.25}La_3Zr_2O_{12}$ pellet is displayed and compared to an anode powder of $Li_4Ti_5O_{12}$ and an electrolyte $Li_{6.25}Al_{0.25}La_3Zr_2O_{12}$. Here, the observed spectrum shows bands from thin film of $Li_4Ti_5O_{12}$ as well as contribution from the underlying electrolyte substrate. This is expected, since the penetration depth of the Raman signal were to penetrate more than the 80 nm of thin film thickness reaching into cubic garnet $Li_{6.25}Al_{0.25}La_3Zr_2O_{12}$ who's Raman modes have already been described by several authors and matching well to the ones observed here.[94,168,218,230]

We confirm that the observed spectrum shows existence of both desired structure types for the battery and near order, namely, the spinel phase for thin film of $Li_4Ti_5O_{12}$ as well as $Li_{6.25}Al_{0.25}La_3Zr_2O_{12}$ from the underlying electrolyte substrate after processing which is subjected in the following as half-cells for battery tests.

2.7 All solid state battery from thin film $Li_4Ti_5O_{12}$ and cubic garnet $Li_{6.25}Al_{0.25}La_3Zr_2O_{12}$

The successful deposition of $Li_4Ti_5O_{12}$ phase therefore gave rise to an assembly of a battery cell: Figure 8a shows the schematic of the cell measured ($Li_{6.25}Al_{0.25}La_3Zr_2O_{12}$, with the $Li_4Ti_5O_{12}$ thin film), including a current collector of Cu and Li metal foil as reference. Chemical comparability of the $Li_4Ti_5O_{12}$ thin film deposited on MgO and on the garnet pellet was based on the assumption that a close phase transfer of $Li_4Ti_5O_{12}$ is present, however, changes in the interface chemistry by nature of different substrate have to be accounted. We demonstrate the successful galvanostatic charge and discharge profiles for the assembled cell, Fig 3b, over 22 cycles. A discharge capacity of ~300 mAh/g is obtained at the 1st discharge cycle that recovers close to the expected theoretical value of ~175 mAh/g at the subsequent cycles. (Note that we assign the irreversible discharge capacity obtained in the 1st cycle to potential additional oxide and hydroxide phases present at the solid electrolyte / $Li_4Ti_5O_{12}$ interface as a result of the air exposure. In order to exclude the formation of TiO_2 (anatase or rutile) impurity phases, the Raman spectra of both grown $Li_4Ti_5O_{12}$ thin films on MgO as well as on the $Li_{6.25}Al_{0.25}La_3Zr_2O_{12}$ pellet have been compared to powder reference spectra of TiO_2 anatase as well as TiO_2 rutile, as shown in Supporting Figure S3. Typical charge and discharge plateaus

for $Li_4Ti_5O_{12}$ can be clearly observed and the cycling is reversible for the tested cell. In Figure 8c, the dQ/dV plot taken from the 3rd charge / discharge cycle also corroborates our findings with oxidation and reduction peaks at 1.57 V and 1.53 V, that can be clearly assigned to $Li_4Ti_5O_{12}$, and comparable to similar solid[169] and liquid[204] electrolyte-based batteries operating with $Li_4Ti_5O_{12}$ slurry-cast anodes in literature. Oxidation and reduction peaks show the polarization in the system that can be quite expected in an all solid state cell due to interface resistance effects. The rate capability test within the first 22 cycles is shown in Figure 8d. The battery cell was tested with charge/discharge rates of 2.5 mA/g (6.3×10^{-5} mA/cm^2), 12.5 mA/g (3.1×10^{-4} mA/cm^2), 25 mA/g (6.3×10^{-4} mA/cm^2), followed by 2.5 mA/g (6.3×10^{-5} mA/cm^2). Due to the nature of the low cycling speed chosen, stable operation of the cell was maintained for 29 days. Though the Coulombic efficiency is rather limited at lower rates (e.g. 2.5 mA/g), it recovers to above ~95 % at the higher rates (e.g. 12.5 mA/g). A discharge capacity of 97 mAh/g is obtained at the 15th cycle even at the highest rate of 25 mAh/g that is an encouraging value considering the similar $Li_{6.25}Al_{0.25}La_3Zr_2O_{12}$-based solid state systems which are not thin film based and often operate at higher than room-temperature.[169]
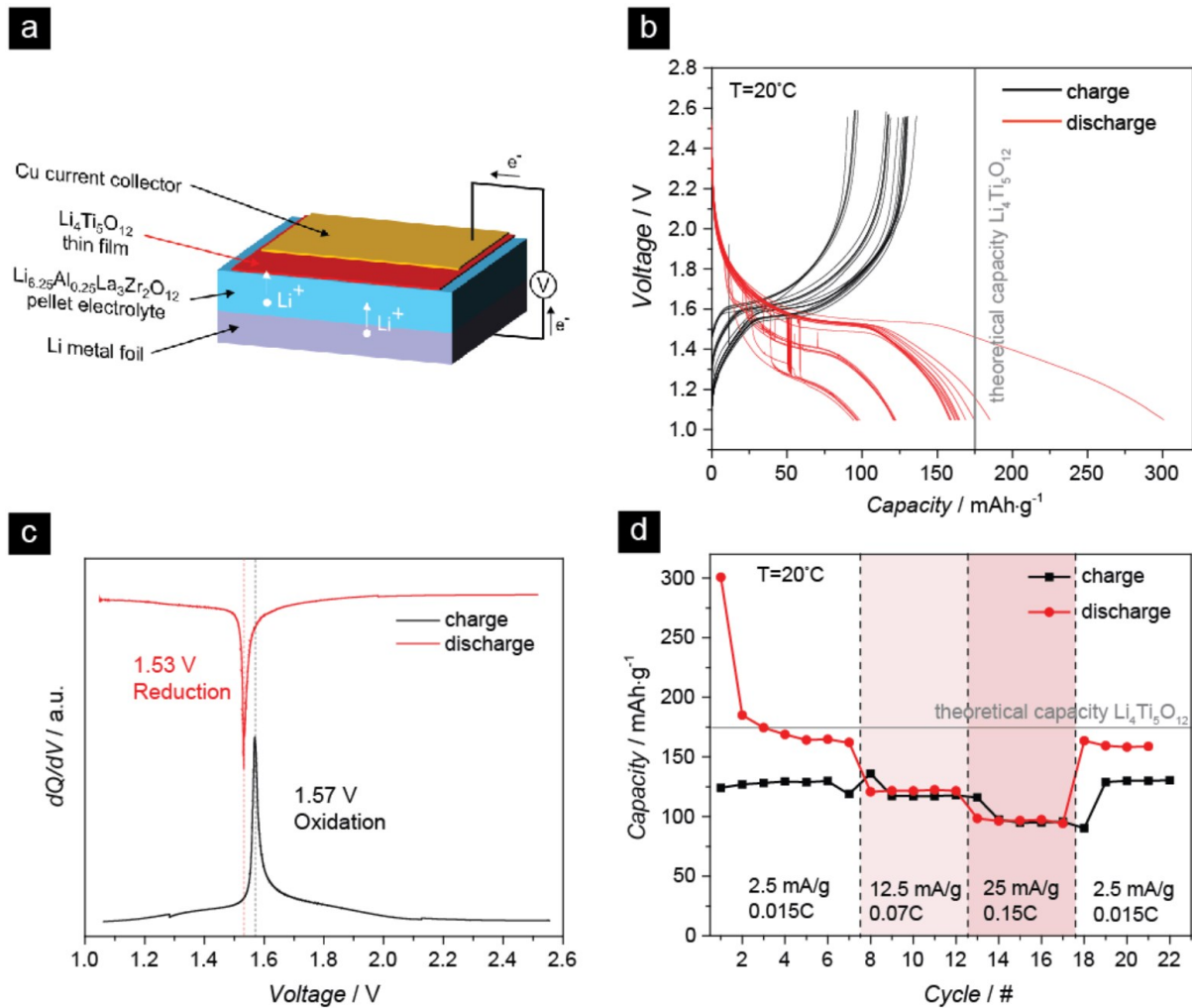
Figure 8 a) Sketch of a battery half-cell assembled for cycling experiments based on the system Li foil | $Li_{6.25}Al_{0.25}La_3Zr_2O_{12}$ pellet | $Li_4Ti_5O_{12}$ thin film | Cu current collector. Tungsten needles (black) were used to contact top and bottom electrodes. b) Charge and discharge profiles for the battery half-cell with thin film $Li_4Ti_5O_{12}$ electrode. The typical voltage plateau of $Li_4Ti_5O_{12}$ at around 1.5 V can be clearly observed. c) dQ/dV-plot of cycle number 3 at rate of 2.5 mA/g. d) Rate capability study of the same cell under different current rates. The discharge rate (red) was higher with respect to the charge rate (black).

In summary, $Li_4Ti_5O_{12}$ thin film / $Li_{6.25}Al_{0.25}La_3Zr_2O_{12}$ pellet / Li batteries could successfully be used to build and cycle the first thin film based anode / $Li_{6.25}Al_{0.25}La_3Zr_2O_{12}$-system with characteristic and reproducible voltage plateau at around 1.5 V close to theoretical capacity of 175 mAh/g. In comparison to literature work on Li-garnet all solid state batteries, one could state that the results demonstrated in this work are a step forward in the field of all solid state batteries based on $Li_{6.25}Al_{0.25}La_3Zr_2O_{12}$ solid electrolytes, see Figure 9. The previous investigations of thin film electrodes with $Li_{6.25}Al_{0.25}La_3Zr_2O_{12}$ solid electrolytes delivering capacities close to the theoretical values under stable cycling conditions mostly focused on cathodes (e.g. ($LiCoO_2$) from Ohta et al.[166]). Thus, this study gives new perspective on the use of oxide-based low voltage anodes for future strategies avoiding Li-dendrite formation or safe solid state microbattery thin film assemblies based on Li-garnets.
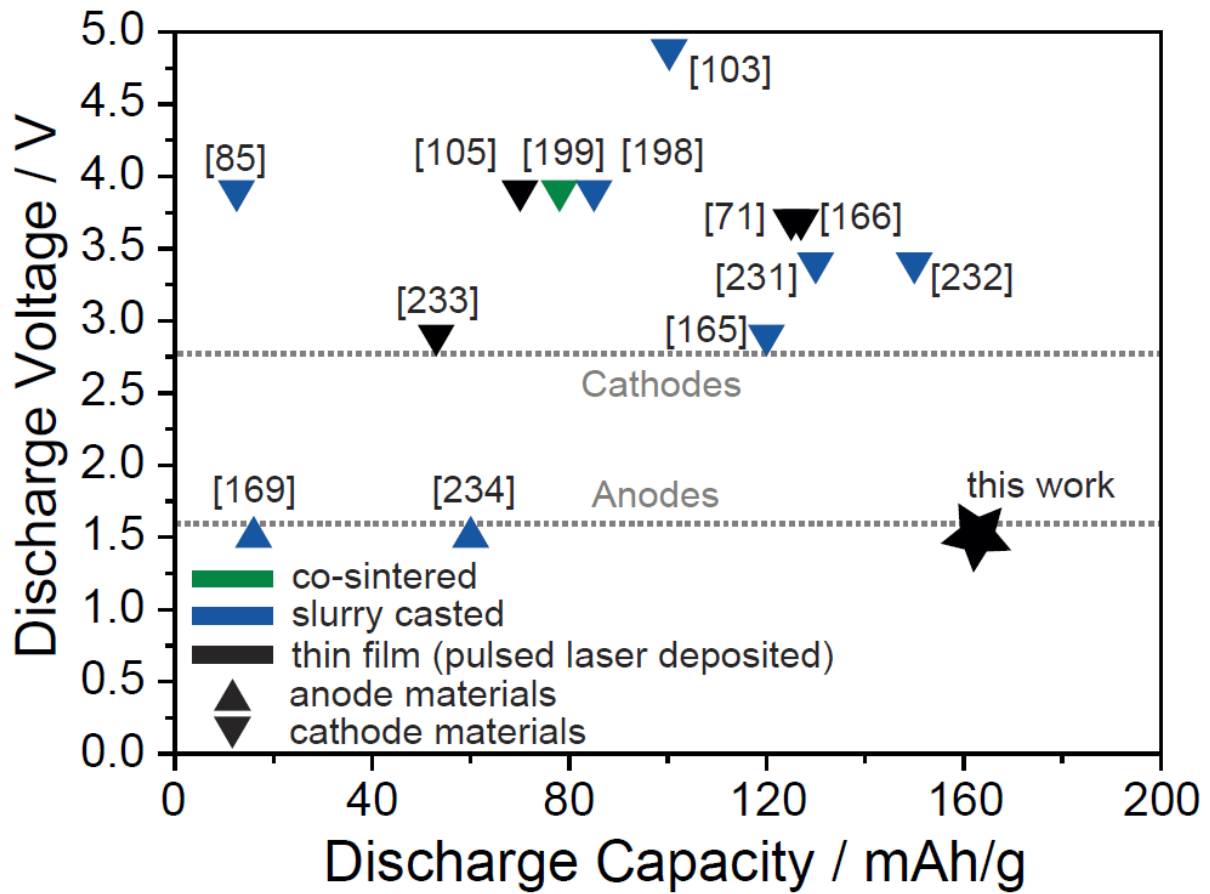
Figure 9 Overview on published work[71,85,103,105,165,166,169,198,199,231–234] *on garnet LLZO-based battery assemblies in voltage vs. achieved gravimetric capacity representation. Different deposition techniques are distinguished by color. Black indicating thin film electrode work, blue indicating any type of slurry deposition technique and green standing for co-sintering approaches.*

2 Conclusion

In this work, we demonstrate that Li-garnet electrolytes processed as pellets and combined with $Li_4Ti_5O_{12}$ thin films can show stable cycling kinetics and reach almost close to theoretical capacity of 175 mAh/g. We demonstrate here the stable operation at room temperature during 29 days with 90 % of theoretical capacity retention at 2.5 mA/g over 22 cycles. The results clearly indicate two implications to the all solid state battery field and technology: Firstly, although a lot of effort was already put in the development of suitable cathode materials for garnet electrolyte-based batteries, the conducted work positions itself as one of the first successful attempts to also implement thin film anode materials. This represents an important step forward towards the successful fabrication of full metal oxide-based batteries with $Li_7La_3Zr_2O_{12}$ electrolyte compounds. It also opens up new pathways in fabrication of future batteries with various solid oxide electrode materials, as well as to form fully ceramic microbatteries possibly on chips. Secondly, we report by the stable cycling kinetics a high stability of the $Li_4Ti_5O_{12}$ oxide anode towards $Li_{6.25}Al_{0.25}La_3Zr_2O_{12}$ which is of relevance in view of current Li-dendrites forming easily for systems with metallic Lithium anode solely.[23] DFT calculations by the Ceder group[235] suggest that $Li_4Ti_5O_{12}$ with its voltage plateau around 1.5 V fits perfect into the stability window of the presented electrolyte and agree with the presented findings. This benchmarks the suitability of oxide-based anodes such as $Li_4Ti_5O_{12}$ as alternative to lithium for safe microbattery to large-scale storage.

2   Acknowledgements

This chapter was based on the following manuscript that was submitted for publication:

Lithium Titanate Anode Thin Films for Li-Ion Solid State Battery Based on Garnets

Pfenninger Reto, Afyon Semih, Garbayo Inigo, Struzik Michal, Rupp Jennifer .L.M.

Advanced Functional Materials, 2018, 1800879

PART III: A Low Ride on Processing Temperature for a Fast Li Conduction in Garnet Solid State Battery Films

This thesis chapter is going to be published as an original research paper entitled:

The following two patents

LITHIUM-CONTAINING THIN FILMS (US 62/718,838)

And

METHODS OF FABRICATING THIN FILMS COMPRISING LITHIUM-CONTAINING MATERIALS (US 62/718,842)

Have been filed jointly by MIT and ETH Zurich based on the invention described in this chapter.

3. Abstract

A critical parameter for large-scale integration of solid state batteries is to establish processing strategies assembling battery material components and interfaces at lowest processing temperature, but keeping the Li-conduction up. Typically we live in a divided ceramic world where either processing knowhow exists to make fast (cubic) Li-garnet electrolytes through classic sintering at high temperatures beyond 1000 °C for mm-sized and high conducting components, or through thin films at attractive low processing temperatures of 600 °C and for hundreds of nanometer thickness but often at expense of orders of magnitude lowered Li-conduction. Despite extensive research efforts, integrating thin ceramic electrolytes and keeping high Lithium concentration and conduction at low processing temperature remains a challenge for solid state batteries based on Li-garnets. Here we report an alternative ceramic processing strategy establishing Lithium reservoirs directly in Li garnet films (through Li_3N multilayers) that allow for Lithiated and fast-conducting cubic solid state battery electrolytes at unusually low processing temperatures (by hundred degrees of celsius) compared to state-of-technology. A processed Li-garnet through the multilayer approach was found to have for the film a fastest ionic conductivity of $2.9(5)\times10^{-5}$ Scm^{-1} at room temperature and desired cubic phase but was stabilized at 400 °C lowered processing temperature. Here we consider in detail material processing strategies for Li-garnet conductors and describe the evolution of the new multilayer processed fast battery electrolyte films that enable future solid state battery architectures with more room for cathode volumes by design and reduce processing temperatures and costs.

3. Introduction

Solid State Batteries (SSBs) offer safe alternatives to classical Lithium-ion batteries (LIBs) due to the non-liquid nature of the electrolyte and give perspective to assure both, high energy and power densities.[100] Despite the fast growing field of solid state batteries, the high temperature manufacturing of the battery cell components and co-assembly of solid electrolyte/cathode interfaces define largely by structures and kinetics the battery characteristics for technology. Recent progress on solid state batteries identified Li-garnets such as $Li_7La_3Zr_2O_{12}$ as promising candidates for the electrolyte due to their wide electrochemical stability window,[236] fast Li-conductivity[70,127] of 0.1 mScm^{-1} at room temperature and non-flammability. Compared to other fast conducting solid state battery electrolytes such as LGPS[49,52,144] or $Li_7P_3S_{11}$,[237,238] Li-garnets exhibit an improved thermodynamic stability especially towards the Lithium anode. However, one major drawback of Li-garnet electrolytes is that the high Li-conductivity requires stabilization of the cubic phase (*Ia3̄d*[70,76] or the acentric cubic *I-43d*[73,74]) through doping of the structure with elements on either the Li-site (Al^{3+} and Ga^{3+}),[78–81] the La-site (Sr^{2+}, Nd^{3+}),[82,83,193] or on the Zr-site (mainly Ta^{5+})[17] and solid state manufacturing. The current predominant processing strategies are either sintering of the initial Li-garnet particles to a dense pellet[72,79,81,167] or a tape.[231,239,240] To activate sufficient grain boundary and volumetric diffusion in densification for either, pellet or tape, sinter temperatures beyond 1050 °C are a necessity for cubic Li-garnets. An attractive solution to drastically reduce the manufacturing temperature by more than $-\Delta 400$ °C and getting as a bonus reduction of the solid electrolyte component thickness from mm to hundreds of nanometer scale is to explore *processing of Li-garnets in the thin film form*. This would contribute in an effort to allow for an equivalent battery volume, a higher energy density as more volume can be assigned to the electrodes, allowing for a wider range of co-assembly strategies for cathode / electrolyte due to the substantially reduced processing temperatures (i.e. for co-sintered $LiCoO_2$ on $Li_{6.8}La_{2.95}Ca_{0.05}Zr_{1.75},Nb_{0.25}O_{12}$[199]) and reduce costs as high temperature sinter steps are dropped. In addition, future applications such as biosensors, wearable-computing devices as well as remote-sensing entities, where highly integrated microbattery designs are required would benefit from having access to fast conducting Li-garnet materials in thin film form. Also, these may bypass traditionally employed electrolyte films such as LIPON for microbatteries having manufacturing temperatures close to CMOS demands, faster conductivity and a wider

electrochemical stability window.[142] Here, processing of the electrolyte deserves particular attention for both, large-scale solid state batteries employed in electric vehicles (to avoid sintering, better co-assembly and reduce costs) and for microbatteries towards compatibility with non-heat resistant electronic circuits.

Thin film Li-garnets of the compositions $Li_7A_xLa_3Zr_2B_yO_{12}$ (with A = Al, x = 0-0.71) and (B = Ta, Y, y = 0-0.4) have been synthesized by vacuum-based techniques such as RF-sputtering,[126,171,172] Pulsed Laser Deposition (PLD),[134,177,178,241] and wet-chemical synthesis by MO-CVD[174] and sol-gel methods.[135,242] The vast majority of Li-garnet thin films reveal an ambient conductivity of 10^{-8} to 10^{-6} Scm^{-1} and exhibit predominantly a crystalline phase (mostly cubic or cubic/tetragonal mixed) after processing at temperatures of 600-1000 °C,[135,174,176,177] mostly by sol-gel[135,176,242] or PLD[134,178,179] depositions. Compared to tape or pellet-processed Li-garnets, which have been manufactured through high temperature sintering of powders, it can clearly be concluded that today`s state-of-technology on thin film manufacturing results in the majority at a 3 to 5 orders of magnitude reduced Li-conductivity and presents challenges in achieved phase purity of the high conducting cubic phase. We summarize, that the following challenges define for Li-garnets their implementation roadmap as fast Li-conducting solid electrolyte processed towards low temperatures:

3.1   Phase evolution

In classic sintered pellets or tapes, nucleation and crystal growth to a mostly tetragonal phase occurs predominantly in the as-synthesized powders (except for modified sol-gel routes[168]) and the active densification and grain growth proceeds via diffusion in the solid body. In this sintering process, also the transfer of the low conductive tetragonal to the high conductive cubic phase sets normally in close to 1000 °C.[127] In contrast, a dense body is directly deposited either through a wet chemical metal salt → oxide transfer or by a vacuum method, through ablation from either multiple metal targets or a full ceramic one, on a substrate at relatively low temperatures of room temperature to 300 °C.[175,241] At this low temperature of deposition the film body is dense, however, nucleation, crystallization and grain growth need to be activated either by a medium temperature deposition or post-anneals, conventionally carried out at 400-800 °C.[174,179]

In general, phase evolution studies for LLZO as thin films remain scarce: For example, amorphous films can be obtained by RF-sputtering, PLD and sol-gel methods, and revealed conductivities in the range of 3.4×10^{-7} Scm^{-1} to 2.8×10^{-6} Scm^{-1} already at room temperature.[172,177] A recent discovery on polyamorphous states by Garbayo et al.[241] provides insights on the formation of low temperature processed Li-garnets. In sputtering and PLD studies, an on-set of low conductive tetragonal phase was observed for a temperature regime of 500 to 600 °C.[126,134] Cubic phases could be synthesized for temperatures exceeding 600 °C by RF-sputtering [126] and 900 °C for MO-CVD depositions.[174] No clear trend on the dependence of the precise dopant towards thin film room temperature conductivity values could be observed for the cubic garnet films. In addition, the temperature at which the cubic phase can be stabilized is generally lowered by 400 °C for thin films, when compared to pellet or tape-processed LLZO via sintering.[126,174,176] Out of the mass the so far highest conductivities of 1.6×10^{-5} Scm^{-1} were reported for RF-sputtered Ga-doped LLZO films[126] followed by epitaxial Al-doped LLZO PLD[178] depositions with 1.0×10^{-5} Scm^{-1}, both measured at ambient for the cubic phase. A recent study on Ga-doped LLZO thin films by Rawlence et al.[126] reported the appearance of tetragonal phase between 500 °C and 600 °C, and could obtain cubic LLZO in thin film after a 5 h isothermal hold at 700 °C for thin films fabricated via RF-sputtering. In another study by Katsui and Goto,[174] MO-CVD deposited LLZO with a consecutive post anneal treatment lead to tetragonal phase at 750 °C and cubic one only above 900 °C for undoped LLZO. Furthermore, reports from Chen et al.[176] performed on Al-doped LLZO, prepared by a sol-gel method and deposited via spin-coating, achieved highest ionic conductivity of 1.7×10^{-6} Scm^{-1} for the case of a 600 °C post-annealing. In a similar manner, a comparison of reported activation energies as a function of thermal processing temperature of the thin films can be studied: Methods that employ PLD deposition achieve activation energies in thin films, which are with 0.32 eV closest to LLZO pellets,[177] which usually are in the range of 0.28-0.33 eV.[169,243] Other methods for deposition show activation energies in the range of 0.32 up to 0.60 eV.[177,179] In conclusion, it is demonstrated that an unusual wide range of conductivity variation, namely, over three orders of magnitudes exists dependent on processing method for cubic LLZO. Also, opportunities to process thin Li-garnet solid state electrolytes at low processing temperatures are clearly present. If we assume that the cubic phase is correctly identified, then this points to processing-dependent changes in chemistry, lithiation degree or an altered grain boundary to volume ratio, which come largely into play for low temperature and thin film manufacturing of cubic Li-garnet materials.

3.2   Lithiation degree

Classically sintered tapes and pellets require smart processing strategies to prevent Lithium loss during sintering, as otherwise phase transition to the low conducting tetragonal phase is a prominent challenge. A common way, that helped mitigating this issue at least for the case of high temperature tape and pellet processing, was the purposeful overlithiation of the stoichiometry prior to heat treatments (usually +10 wt.-% regarding nominal Li-stoichiometry[70]), sintering in parent powder under oxygen atmosphere and stabilization by dopants. However, Li-consisting thin films are at risk to not reach the high lithiation degrees desired. Simply put, any vacuum process triggers severe volatility of Li^+ at deposition under the exposure to temperature and high energy. In the case of thin film deposition methods from the vacuum that rely on a dense pellet target such as PLD or sputtering, purposeful overlithiation of ablation targets did not turn out to be broadly applicable, since the density achieved of overlithiated targets usually remained low with < 80 %, resulting in poor thin film deposition quality. For example, particle ablation from an overlithiated but too porous target leads to pinholes, structural inhomogeneities and was so far not demonstrated to be the route of success in processing of cubic garnet films. Also, the effect of oxygen partial pressure on the film quality and nonstoichiometry of both, oxygen and lithium ions for garnets remains unexplored.

Now given the wide scatter in ambient Lithium-conductivity over three orders of magnitude for the presumable cubic-phases of the Li-garnet materials reported for thin films,[126,242] we conclude that the effective Lithiation degrees most likely differ and are strongly processing dependent. It has also been reported for LLZO pellets, that variations in local conductivities – measured carefully by microcontacts – result in spreading over half an order of magnitude in conductivity on the same sample of confirmed cubic phase.[88] Lithiation degrees are challenging to measure and usually hardly accessible in a quantitative manner for pellets and thin films by classical lab equipment and therefore normally rarely measured nor reported. Since classic overlithiation of ceramic pellets does not work out for most vacuum processed garnet films, simply upon the high Lithium loss, the target material is too loose and crumbles, new strategies are needed. And, one may curiously ask: How do we lithiate and manufacture next generation of garnet-materials to preserve cubic phase and conductivity for thin films?

Through this study, we propose a new strategy to overcome the Lithium loss challenge for thin film depositions of garnets. The new idea is here to deposit sequences from the Li_3N and Li-garnet sources and that upon a post annealing step (or for deposition at temperature) Li_3N decomposes and Lithium diffuses into the garnet structure assuring sufficient Li-stoichiometry. Hence, we select *Li_3N as a source providing an internal Li-reservoir during anneals to compensate for the occurring Li-loss for the Li-garnet films*, see IP for further details.[244,245]

Till date only Li_2O was so far considered as internal Lithiation source to process Li-garnet films.[126,177] For example, it has been reported that multi-target RF-sputtering, such as simultaneous ablation from dense targets of Li_2O, LLZO as well as Ga_2O_3 could to some extend resolve this issue, and lead to relatively high conductivities of 1.6×10^{-5} Scm^{-1}.[126] On the other hand, another example of a multilayer deposition for the case of PLD, an alternating deposition from a dense stoichiometric LLZO as well as excess Li-providing ceramic sources Li_2O, led to only poor conductivity of 7.4×10^{-7} Scm^{-1}, probably due to the higher post-anneal treatment at 1000 °C and resulting Li-loss, see Tan and Tiwari.[177] Notably, the use of Li_2O as an overlithiation target in PLD deposition may lead to poor deposition efficiency due to the high band gap > 5 eV of the material,[246] for which we propose in this study the much more suitable Li_3N with a band gap of 1.14 eV.[247] The advantage in selecting Li_3N over other Lithiation sources for vacuum deposition is in the easy decomposition of the compound at elevated temperature and its fast deposition rate by PLD benchmarking a novel manufacturing strategy for overlithiation of Li-garnets to assure a cubic phase at low temperature and for film processing.

In the present study, we show a new processing method to manufacture at lowest processing temperature cubic and thin Li-garnet solid state battery electrolyte with fast Li-conductivity as films engineering internal Lithiation reservoirs to keep the critical phase. The presented manufacturing strategy contributes to substantially reduced processing temperatures for solid state battery electrolytes of cubic Li-garnets with desirable thin ceramic structures and high Li-conduction.

3. Experimental

3.3 Material Synthesis of the PLD Targets for Low Temperature Li-Garnet Thin Film Depositions

In order to obtain a multilayered thin film structure, two dense ceramic bodies had to be fabricated first, which were then later used as two separate targets for the deposition of the thin films. We synthesized the *PLD target for the Li-garnet* thin film PLD depositions through a nitride-based, modified sol-gel method. $Li_{6.25}Al_{0.25}La_3Zr_2O_{12}$ powder was synthesized based on a recipe shown by Van den Broek et al. in Ref.[169] For this, stable precursor sols were obtained by dissolution of stoichiometric amounts of $LiNO_3$ (99.99 %, Merck), $La(NO_3)_3(H2O)_6$ (99.9 %, Alfa Aesar), and zirconium(IV) 2,4-pentanedionate (Alfa Aesar) in a water and ethanol mixture which was calcined at 600-650 °C after drying. The powders were pressed into pellets by uniaxial pressing followed by isostatic pressing at a pressure of 440 bar for 3 min. Pellets were then sintered in an alumina crucible inside a bed of parent powder material at 1050 °C for 12 hours with ±10 °C/min. A Li-garnet target of 27 mm ± 1 mm in diameter was obtained with > 85 % of theoretical density.

As a second target for the multilayer deposition and active lithium reservoir to control the Li-garnet chemistry for post-annealed thin films, we synthesized a *PLD target for Li-nitride*. Uniaxial pressing of Li_3N powder (Sigma Aldrich, ≥ 99.5 %) inside an Ar-filled glovebox at 10 tons for 3 minutes was followed by isostatic pressing at 440 bar for 3 min. Sintering of the pellet buried in parent powder at 600 °C with ±10 °C/min for 6 hours under 50 sccm of ultra-pure N_2 lead to a pellet of 28 mm ±1 mm in diameter with > 85 % of theoretical density. Exposure to ambient atmosphere with this material was kept minimal in order to prevent potential degradation and chemical reaction in air prior to PLD system entry.

3.4 Thin film Processing of Li_3N / $Li_{6.25}Al_{0.25}La_3Zr_2O_{12}$ Multilayered Electrolytes by PLD Deposition

Thin film multilayers of repeating layer sequences of Li_3N and $Li_{6.25}Al_{0.25}La_3Zr_2O_{12}$ were deposited on (001) oriented MgO substrates (Crystec, Germany) by pulsed laser deposition. The equipment for deposition (PLD, Surface, Germany) included a KrF excimer laser of 248 nm wavelength at a frequency of 5 Hz and 10 Hz for Li_3N and $Li_{6.25}Al_{0.25}La_3Zr_2O_{12}$, respectively. Both PLD targets were thoroughly polished prior to transfer into the vacuum chamber.

The target-to-substrate distance was kept constant at 70 mm and background pressures during deposition was fixed at 0.013 hPa O_2 in the case of $Li_{6.25}Al_{0.25}La_3Zr_2O_{12}$-layers and 0.04 hPa O_2 in the case of Li_3N-layers. Each deposited film was consisting of exactly 9 individual layers: 5 were chosen to be $Li_{6.25}Al_{0.25}La_3Zr_2O_{12}$ exhibiting a film thickness of 50±5 nm, which were alternated with 4 intermediate layers of Li_3N revealing a film thickness of 25±3 nm. Independent on the annealing-strategy and active lithiation of the garnet phase, all films were always cooled down to room temperature under 0.04 hPa of oxygen inside the PLD vacuum chamber. The hypothesis of this work is to use here the lithium nitride layers of the multilayer to activate upon anneal decomposition of the Li_3N supplying the lithium to overlithiate the Li-garnet multilayer constituents. To do so, we aimed for two strategies with slightly different implications on the film growth, chemical and structural evolution: i.) we select directly the film temperature at deposition on the substrate to be at 660 °C, or ii.) we cool the film after deposition at 300 °C to room temperature and subject it to a post annealing at 660 °C under pure oxygen externally.

3.5   Structural Characterization of Targets and Thin Films Materials

The electrolyte target pellet was characterized by X-Ray diffraction (XRD, Bruker D8, USA) with Cu K_α radiation in Bragg-Brentano geometry. An extraction voltage of 40 kV at 40 mA current was used between $2\Theta = 25°\text{-}55°$, see Supporting Figure S6 for more detail on the phase analysis and literature comparison. Thin film samples on (001) oriented MgO were investigated at room temperature by a thin film XRD diffractometer machine (Bruker Discovery D8, USA) operating with Cu K_α radiation in Bragg-Brentano geometry in a range of $2\Theta = 15°\text{-}32.5°$. Microstructures of the as deposited as well as post annealed thin films were investigated by cross-sectional Scanning Electron Microscopy (SEM, Leo 1530, Germany).

3.6   Ex- and In-situ temperature and atmosphere controlled Raman Spectroscopy

After deposition of the thin films, a post-annealing treatment was performed to analyze the formation of different crystallographic phases as a function of thermal treatment. To probe the phase evolution of the multilayer to single phase Li-garnet films, we carried out in-situ and ex-situ heating / cooling-controlled Raman spectroscopy (WiTec, Germany), using a heating chamber equipped with an optical window and an active water cooling (Linkam T95-HT, Linkam Scientific, UK) operating for the temperature window of 300 °C to 980 °C at a rate of ±10 ºC/min. First, for the ex-situ measurements, the as deposited thin film samples were heated to the desired temperature under pure O_2 flow, and then measured after cool down to room temperature. Optical Raman spectroscopy was conducted with a solid state laser at 10 mW power and 532 nm wavelength with a spectral resolution 0.7 cm^{-1} used for near order structural analysis. Note, that the decrease in intensity below 80 cm^{-1} can be attributed to the edge-filter cutoff for the laser wavelength used, and is therefore attributed to an equipment artefact. In case of ex-situ analysis, samples were simply measured at room temperature.

The same experiment was also conducted in-situ, however, due to the elevated temperature, an increased background noise was present, for which we focus on ex-situ data, see Supporting Figure S7 for further details. In-situ Raman was performed to assess the annealing times required for phase formation, indicating that already 15 minutes annealing was sufficient, for which we fixed 15 minutes as the annealing time for the ex-situ experiments.

3.7 Thin Film Negative-Ion TOF-SIMS for Qualitative Elemental Analysis

To investigate the elemental distribution across the multilayered Li-garnet/Li-nitride thin film structures, an annealed film being of single Li-garnet phase was used and analyzed by TOF-SIMS (TOF.SIMS, ION-TOF GmbH, Germany). Special focus was put in the analysis of nitrogen, to clarify the distribution and content of nitrogen residues from the dissolved Li_3N layers towards the Li-garnet ones. Since the occurrence of nitrogen, which is mostly charged negatively, it is best seen in *negative ion TOF-SIMS*, we chose to use this methodology instead of the more common positive ion TOF-SIMS. For the TOF-SIMS analysis, a primary beam with 25 keV Bi^+ primary ions at a measured current of 3.52 pA was used. The sputtering was performed with 2 keV Cs^+-ion on a grater of 500 μm × 500 μm. The analysis area was 200 μm × 200 μm. The profiling was performed alternating 2.6 seconds of sputtering, 100 microseconds of analyzing with 0.5 seconds of waiting and stabilization time in between. The raster analysis area was random with a 128 × 128 pixel resolution. The emission current was set to 1 μA during the entire measurement.

3.8 Electrochemical Characterization of Thin Film Transport Properties

Electrical impedance spectroscopy (EIS) (Zahner IM6, Germany) was performed to study impedance and ionic transport processes. For this purpose, electrodes were fabricated in an in-plane geometry, using a shadow mask to sputter Pt electrodes on the Li-garnet films and in case of Arrhenius activated transport properties temperature was modulated through an atmosphere-controlled and heated Linkam chamber (Linkam Scientific, UK) to measure electrical and electrochemical characteristics in the temperature window of 50 °C to 400 °C under a constant synthetic air flow of 50 sccm. Pt electrodes were deposited via electron beam evaporation (Plassys MEB 550, France) on the Li-garnet films. Electrode thickness of 100±1 nm was confirmed by quartz crystal frequency thickness monitoring and shaped through a stainless steel shadow mask to strips with dimensions of 3.25 mm×0.5 mm at an electrode separation of 0.25 mm, see inset picture in Figure 15a. Prior to any EIS measurement, we kept an isothermal hold of 15 minutes to equilibrate the substrate and film prior to each EIS measurement. EIS measurements were carried out for the frequency range of 1 Hz to 1 MHz at an AC amplitude of 50 mV and the data were analyzed using ZView 3.4f and OriginPro 9.1 software.

3. Results and Discussion

3.9 Manufacturing Strategy for Lithiated and Low Temperature Processed Garnet Solid State Battery Electrolyte Films

In this work, we explore the deposition of initially multilayered $Li_{6.25}Al_{0.25}La_3Zr_2O_{12}$ (LLZO) / Li_3N thin films to create an internal reservoir of lithium from the Li_3N phases to diffuse and counteract delithiation during the LLZO phase formation at elevated temperature, Figure 10a. Nine repeating layers of LLZO and Li_3N with 50 nm (± 10 %) and 25 nm (± 10 %) thicknesses were deposited on top of each other on a polished (001) oriented MgO substrate by PLD from two own-processed targets. (The targets were previously processed through powder synthesis via a modified sol-gel synthesis-combustion method and a solid state synthesis method for LLZO and Li_3N, respectively. Postsequent pressing and sintering to dense ceramic bodies at 1050 °C (LLZO) and 600 °C (Li_3N) was performed, which we further detail in Experimental). To study the impact of thermal treatment for PLD deposited thin films of LLZO, we use two different paths for manufacturing, which both resulted in the formation of polycrystalline cubic LLZO thin films, Figure 10b: In the first approach, PLD multilayer deposition was conducted at 300 °C, followed by an external post annealing step for 15 min at 660 °C under pure oxygen ($pO_2 = 1013$ hPa). In the second approach, the multilayer PLD deposition was conducted at 660 °C directly at a low partial pressure of oxygen ($pO_2 = 0.04$ hPa). A light microscopy image of the as deposited film at 300 °C covering a ~0.9×0.9 cm^2 MgO substrate processed through the first approach is shown in Figure 10c.
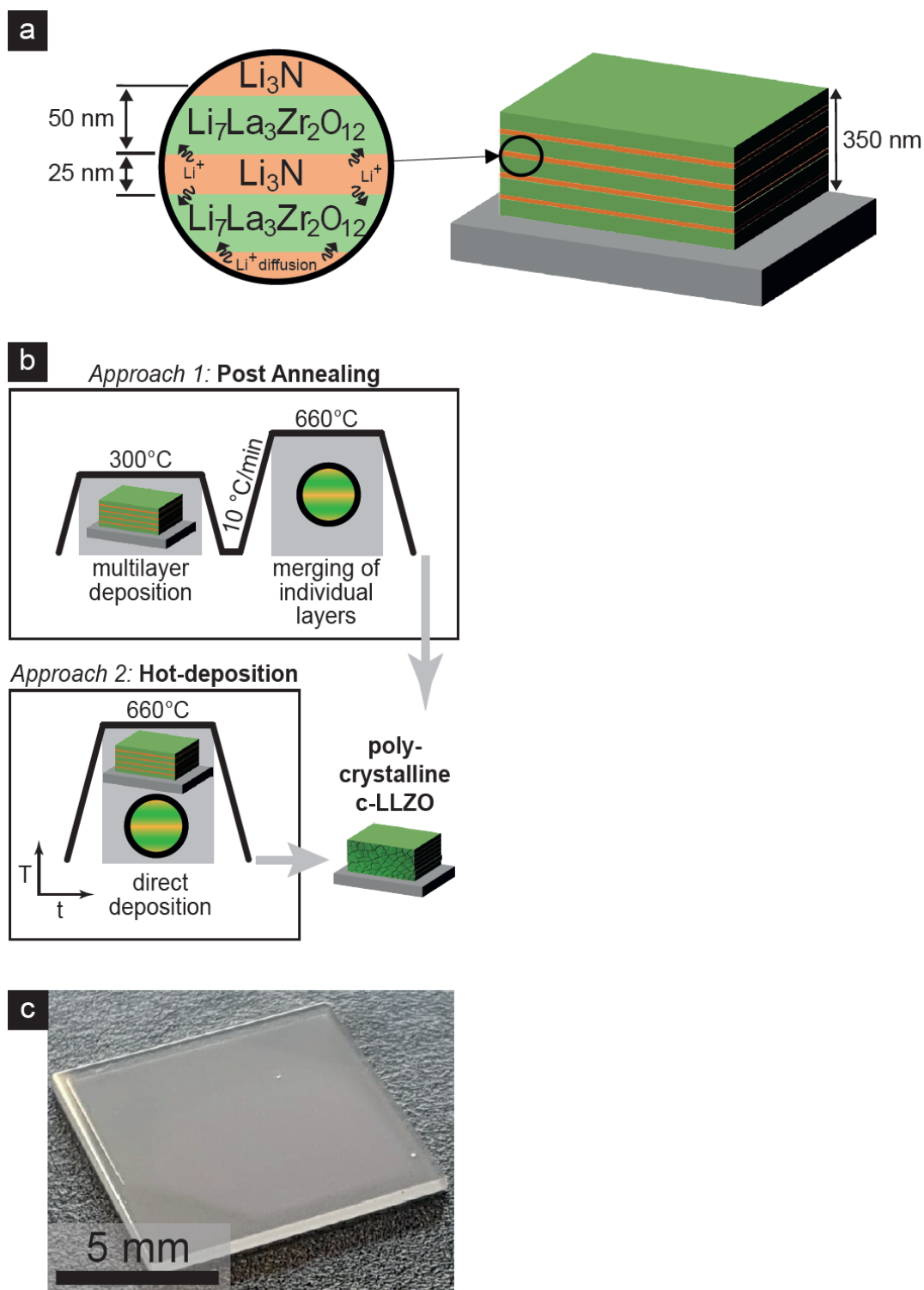
Figure 10 Schematic of the experimental approach for the employment of a multilayer structure in order to deposit cubic-Li₇La₃Zr₂O₁₂ via PLD. Thin layers of Li₃N were incorporated to compensate for lithium loss at elevated temperatures. b) Experimental procedure and schematic of the two possible approaches for obtaining dense polycrystalline thin films of Li₇La₃Zr₂O₁₂ via PLD. c) Optical image of the thin film deposited on MgO substrate.

In order to have a closer look to the microstructure, we turn to SEM and compare a sample deposited at 300 °C without post-anneal, and a film after post-anneal at 660 °C, Figure 11. The presence of the individual repeating heterolayers of LLZO and Li_3N can be observed by a difference in contrast in cross sectional SEM for the as deposited film at 300 ºC, Figure 11a. Layers of delithiated-LLZO and Li_3N where deposited at a thickness ratio of 2:1, resulting in 50 nm and 25 nm per layer, respectively. The total thickness of the obtained heterostructure was 350 nm (±10 %), as measured by SEM, with the indication of intimate contact among the two layers of garnet and nitride phase and no signs of pinholes. When looking at the same thin film in cross sectional SEM, after a post-anneal at 660 °C under oxygen, Figure 11b, the film is dense and we can no longer distinguish by inspection of the cross-section layered interfaces as in the other specimen. We interpret this in the way that the distinct multilayers united at elevated temperature and underwent a merging, so that no more repeating of sequential layers could be observed. To be exact, we note that some closed porosity exists at grain triple-points close to the bulk, which may either be an artefact from the film breakage seen in cross-sectional SEM preparation or may result from the Li_3N decomposition at temperature itself. To also check the hypothesis if thin film multilayers, directly deposited at 660 °C, also resulted in a homogeneous merged thin film of LLZO, we subjected another set of such thin films to inspection by cross-sectional SEM, see SEM Supporting Figure S8 to Supporting Figure S10.
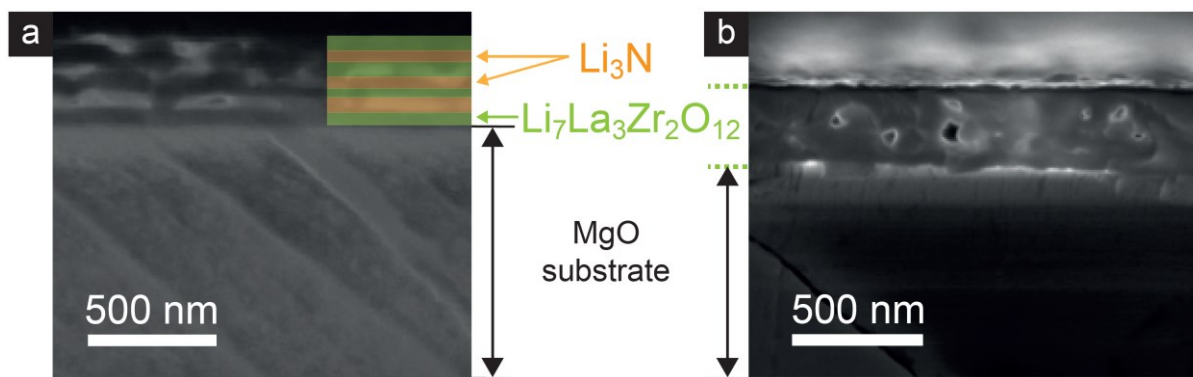
Figure 11 a) SEM image of the multilayer structure deposited at 300 °C, showing the independent layers of delithiated-Li$_7$La$_3$Zr$_2$O$_{12}$ and Li$_3$N deposited on an MgO substrate. We added a color-code for better visibility of the repeating layers of delithiated-LLZO and Li$_3$N in green and orange, respectively. b) SEM image of the same structure after post-annealing at 660 °C, showing a merged thin film of ca. 330 nm thickness.

In order to explore the transformation and local chemistry of the initial multilayered structure to a homogeneous film of LLZO, negative ion TOF-SIMS has been conducted over a film`s cross-section, Figure 12: A thin film of a 300 °C deposited multilayer Li$_3$N / LLZO structure after post annealing at 660 °C to merge the layers to LLZO is measured between two protective platinum contacts. We tracked the single negatively charged ions of Li$^-$, La$^-$, Zr$^-$, Al$^-$ and N$^-$ signal over the LLZO film cross section (through the equivalent of etch time in TOF-SIMS). Firstly, analysis of the spectral line clearly indicates that we have chemical occurrence of all cations Li, La, Zr and Al in the film. Quantitatively, the signal of Nitrogen decreased to < 10 cpm in TOF-SIMS once the post-anneal has been carried out. This indicates clearly that the decomposition of Li$_3$N over the film thickness has taken place and nitrogen goes out of the film. We can track Lanthanum and Lithium over the full thickness of the film clearly above 10 cpm. As a second focus, we analyze the negative ion TOF-SIMS signal of Aluminum over the film`s cross section, as these are good markers for Al-doped LLZO. We find for the Aluminum a periodic occurrence of 4 imposed peaks on the spectral line. A similar trend can also be seen but at a significantly lowered magnitude for Zirconium which reveals slight peak elevations coinciding with the Aluminum peak positions on the spectral line vs. cross-sectional locality of the film. Importantly, the 4 imposed peaks of the Aluminum coincide well with the initial locations of the LLZO layers of the as deposited multilayers even though the films were post annealed. The trend is less obvious for Lanthanum and Zirconium, which seems to be in general more evenly distributed through the film after post-anneal. There has been thorough

discussion in literature on the location and homogeneous distribution of Aluminum or Gallium dopants used for phase stabilization in pellet manufacturing (sintering).[72,87,89,248–250] A recent study by Fleig and Rettenwander et al.[251] demonstrated the effect of inhomogeneous distribution of Aluminum in LLZO as a factor for the observed large spread in measured conductivity values. It was found that Al / Ga dopants, which both occupy lithium sites in the garnet framework, tetrahedrally coordinated 24d[250] or at Li1 site (12a) (in the acentric cubic space group I-43d),[73] respectively, preferably go inside grain boundaries. Gallium is known for the formation of $LiGaO_2$ in the vicinity of grain boundaries,[248] whereas Aluminum forms $LiAlO_2$.[81] From a ceramics perspective it does make sense that the Aluminum accumulates mostly at the original interfaces of the multilayer even after heat treatment (similar to a classic grain boundary interface architecture in a sintered pellet); we cannot compare this finding to other literature till date.
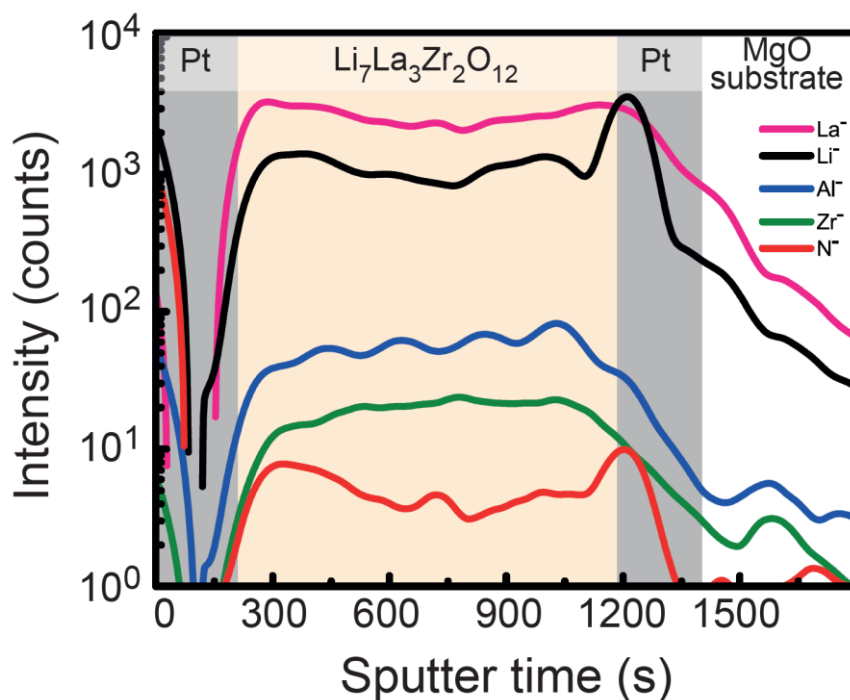
Figure 12 Negative-Ion TOF-SIMS spectrum of a thin film, which was deposited at 300 °C as a multilayered structure followed by a post annealing at 660 °C. Platinum electrodes were deposited on both sides to protect the thin film from exposure and exchange with environmental conditions.

We conclude from the negative ion TOF-SIMS results, firstly that most of the initial Li_3N layer have decomposed (Nitrogen < 10 cpm) after post anneal of the original multilayer, and propose that the lithium diffused into the neighboring $Li_{6.25}Al_{0.25}La_3Zr_2O_{12}$ forming phase majority. Secondly, one can show by TOF-SIMS clearly the origin of processing through the multilayer deposition approach where the Aluminum-dopant of LLZO can be found close to the original locations of the multilayer interfaces even after heat treatment and merging of the layers. In an analogy, one can understand this as similar to increased dopant concentrations present in sintered pellet bodies. Importantly, no major presence of Nitrogen is traceable after post-anneal and all phase composing cations are found for the merged LLZO film.

3.10 Understanding the Role of Internal Lithium Reservoir (Li$_3$N) for the Synthesis of Cubic-Li-Garnet Films at Low Processing Temperatures

To understand the phase evolution with respect to annealing temperatures of the initially multilayered LLZO / Li$_3$N to single LLZO thin films, an ex-situ Raman spectroscopy was pursued. The multilayered films of alternating LLZO and Li$_3$N sequences deposited at 300 °C were selected and post annealing temperatures were varied accordingly prior to Raman analysis in a Linkam hotplate stage, Figure 13a. Close to the original deposition temperature at 300 °C, the multilayered LLZO / Li$_3$N films reveal a generally broad Raman signal with local maxima around 97 cm^{-1}, 325 cm^{-1}, 518 cm^{-1} as well as 665 cm^{-1}. We interpret the characteristic broad peak observed around 325 cm^{-1} and 665 cm^{-1} to the amorphous state of LLZO as discussed by Garbayo et al.,[241] reporting signatures around 335 cm^{-1} and 670 cm^{-1}, respectively.[241] An overlap of the T$_{2g}$ LLZO with the strongest longitudinal E$_{1u}$ Raman mode around 350 cm^{-1} for Li$_3$N [252] exists which does not further allow to confirm the Li$_3$N phase solely by Raman.

Upon heating to 425 °C, more distinct peaks between 100 cm^{-1} and 200 cm^{-1} appear, mainly at 122 cm^{-1}, 159 cm^{-1} and 197 cm^{-1}. Those are indications for the start of an on-going crystallization process. At 585 °C, characteristic peaks at 106 cm^{-1} and 126 cm^{-1} assigned to T$_{2g}$ vibrational modes, as well as the triplet (209 cm^{-1}, 247 cm^{-1}, 288 cm^{-1}) between 200 cm^{-1} and 300 cm^{-1} with T$_{2g}$, A$_{1g}$ and T$_{2g}$ vibrational modes could be identified, respectively.[218,230] Those can be allocated to a full development of the tetragonal LLZO phase.[230] Notably, at 585 °C the peak at 647 cm^{-1} as well as the peak at 247 cm^{-1} (both assigned to A$_{1g}$ vibrational modes) also emerged reducing the overall number of Raman active vibrations and they remained present over all further post annealing up to 710 °C. We interpret this as a phase transformation of the film from the tetragonal to the cubic phase of LLZO taking place between 630 °C and 660 °C. (Note that peaks of the T$_{2g}$ / E$_g$ vibrational modes around 107 cm^{-1} , 123 cm^{-1}, A$_{1g}$ and T$_{2g}$ at 254 cm^{-1} and 364 cm^{-1}, and T$_{2g}$ and E$_g$ at 418 cm^{-1}, 515 cm^{-1} commonly attributed to lithium sublattice vibrations, see Ref.[230]). For temperatures higher than 810 °C, the appearance of peaks at 299 cm^{-1}, 394 cm^{-1}, 492 cm^{-1}, 516 cm^{-1} was measured. Those can further be assigned to E$_g$, F$_{2g}$, A$_{1g}$ and F$_{2g}$ vibrational modes respectively,[241,253] indicating phase transformation to the delithiated pyrochlore La$_2$Zr$_2$O$_7$ phase (LZO). Inspection of these films by micro-Raman reveals that islands of 2-10 µm average in diameter exists which could be identified by as delithiated LZO, whereas the remaining part of the thin film still showed

the full feature-set of cubic LLZO, see Supporting Figure S11 and Supporting Figure S12 for details. Hence, a phase separation exists where local spots of delithiated LZO progress in the LLZO microstructure matrix of the film.
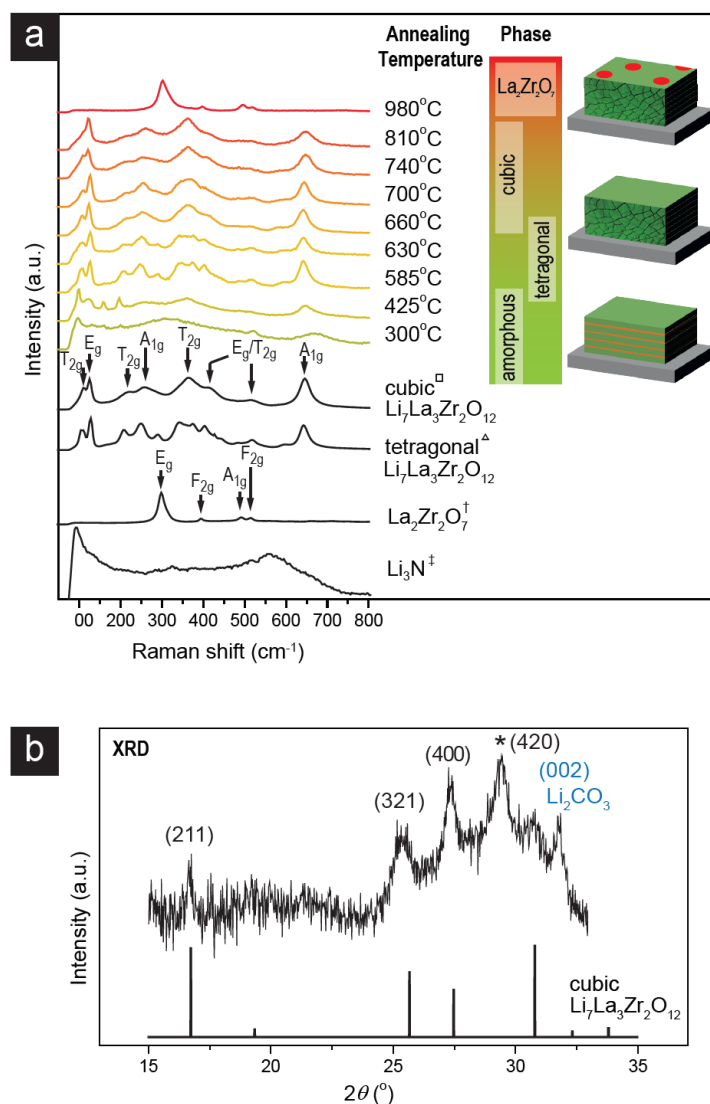
Figure 13 a) Ex-situ Raman crystallization study of separate thin films deposited at 300 °C by PLD, followed by a post annealing at selected temperatures in pure O_2. Films were all measured after cooldown to room temperature. The crystallization started to occur at 425 °C, at 585 °C the tetragonal phase of $Li_7La_3Zr_2O_{12}$ was fully developed, whereas at 660 °C the phase transition to the cubic phase fully completed. At 810 °C, the crystallites of the common delithiated phase ($La_2Zr_2O_7$[253]) started appearing on the thin film of c-$Li_7La_3Zr_2O_{12}$. At 980 °C, a full transformation from Li-garnet to pyrochlore $La_2Zr_2O_7$ was observed due to lithium loss. All reference data was taken from spectra obtained by Tietz et al.[230] (Δ,□) and Kong et al.[253] (†) and stoichiometry and vibrational modes were assigned according to tentative assignments from literature.[230,253]. For comparison, the spectra of the Li_3N PLD target is shown (‡). b) Thin film XRD pattern of the film deposited at 660 °C, showing the formation of the cubic $Li_7La_3Zr_2O_{12}$, in agreement with ICSD 183607.[254] An additional diffraction peak at 31.8° was assigned to the presence of the secondary phase of the Li_2CO_3, which formed due to the long-time exposure to ambient during the measurement. A substrate peak at 29.46° was assigned to MgO and is marked accordingly (*).

To probe the occurrence of the cubic LLZO, identified for post annealing at 660 °C in Raman spectroscopy, we exposed the film also to thin film XRD, Figure 13b. Diffraction peaks could be observed at 16.6°, 25.2°, 27.2°, 30.6° and 31.8° in 2θ geometry. The first four peaks agree with cubic LLZO crystal structure for the Miller indices (211), (321), (400) and (420), respectively, and are in agreement with ICSD 183607.[254] There are two additional peaks at 29.46° and 31.8° which refer to the MgO substrate and Li_2CO_3[229] a known byproduct to form upon exposure of LLZO to moist atmosphere in pellets,[229] respectively (see reference MgO XRD measurement in Supporting Figure S13).

In order to probe, whether there are differences in phase evolution between the two deposition strategies for thin film cubic LLZO, grown in PLD or post annealed at high temperature, we engaged a direct comparison by Raman spectroscopy of the two thin films. Importantly, we also compare these initially multilayer processed films with a traditionally processed LLZO PLD film purely deposited from a single LLZO target at the same temperature of 660 °C, Figure 14. Note that the films deposited at 300 °C and post annealed and the one deposited at 660 °C were exposed to different oxygen partial pressures of 1013 hPa and 0.04 hPa, respectively.

We directly compared the thin films obtained from the two different approaches, the post annealing route conducted at 660 °C towards the hot-deposition at the same temperature, which we rate optimal conditions for both approaches. Both spectra show the observable peaks of the T_{2g} / E_g vibrational modes around 107 cm^{-1} and 123 cm^{-1}, however with more peak overlap in the case of the hot-deposition at 660 °C in PLD. The vibrational modes A_{1g} and T_{2g} at 254 cm^{-1} and 364 cm^{-1} are also present in both cases. However, an additional feature between those to peaks at 309 cm^{-1} could exclusively be identified in the case of the hot-deposition. We interpret those as a feature from a minor contribution of the delithiated phase $La_2Zr_2O_7$, for which the characteristic E_g vibration is found around 299 cm^{-1}. The spectrum of a film *not* processed by a multilayer approach, but from a single LLZO target, shows broad peaks around 340 cm^{-1} and 670 cm^{-1}. Due to the non-distinct features on the observed peaks, we could not identify a particular crystallographic phase being transferred to thin film in this sample. Thus, the shown multilayer process in this work demonstrates the necessity of additional Li_3N reservoirs for a successful transfer of Li-garnet to the thin film form by PLD.
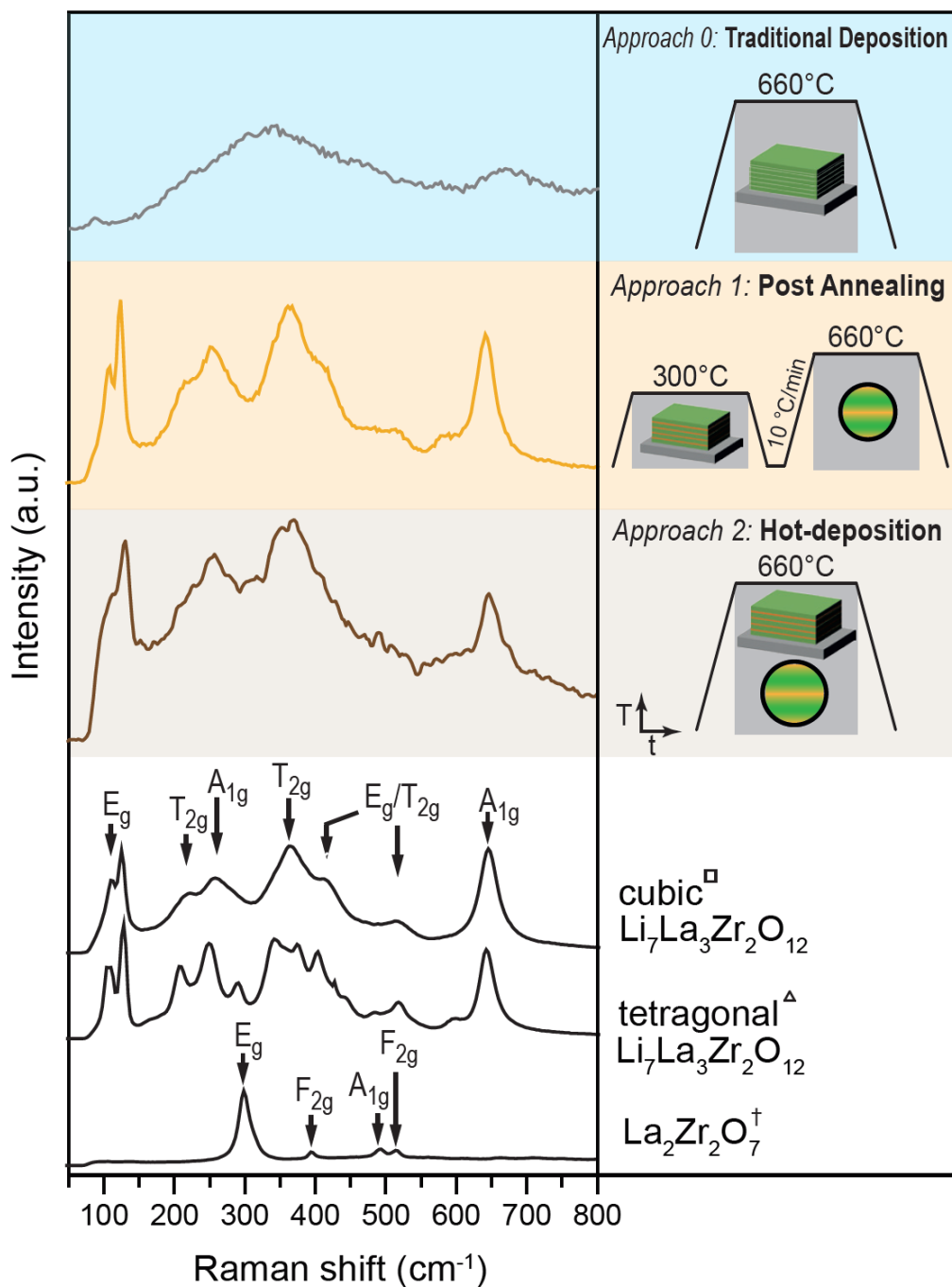
Figure 14 Raman spectra of selected thin films deposited by PLD under optimal conditions by three different approaches. The spectra were recorded after cooldown to room temperature. Reference spectra were taken from Tietz et al.[230] (Δ,□) and Kong et al.[253] (†) and vibrational modes were assigned according to tentative assignments.

In summary, both deposition approaches via multilayers with Li_3N did result in the formation of the cubic phase of LLZO in thin film form, however in the case of a hot deposition at 660 °C with no post anneal, we do observe potential minor phase contributions from the delithiated phase LZO. This may point to slightly different Lithium concentration per volume, even though the main phase of cubic LLZO is maintained. Altered oxygen partial pressures, to which the two samples were subjected during fabrication, 1013 hPa O_2 for the post-annealed sample vs. 0.04 hPa O_2 for the case of hot deposition, could play a key role, even though phase stability is preserved in both. A recent study by Kubicek et al.[255] suggests altered transport properties as a function of oxygen non-stoichiometry vs. lithium non-stoichiometry, with relative oxygen vacancy concentrations estimated in between 2×10^{-7} to 4×10^{-4} for a similar Aluminum doping concentration (0.15-0.3 Al per formula unit). With curiosity on observable changes in conduction, we will subject the films now to a conductivity study in the following.

3.11   Conductivity of Cubic Garnet Solid State Electrolyte Films

In accordance, we collected electrochemical impedance spectra for measuring the total conductivity (bulk and grain boundary contributions) of thin films either processed via the new multilayer approach based on Li_3N / LLZO or from a traditional LLZO target alone. Electrochemical impedance measurements in an in-plane geometry were performed, as depicted in the inset picture in Figure 15a. Due to strong overlap of bulk and grain boundary contributions from the Nyquist representation of EIS, it was not possible to separate and quantify those separately. Consequently, a resistor in parallel with a constant-phase-element was used for fitting and understood as the total Li^+ conductivity of the film. An example of collected data points and respective fitting of the post-annealed sample at 240 °C and 281 °C is shown in Figure 15a. The calculated conductivities are plotted in an Arrhenius-type representation, respectively, Figure 15b.
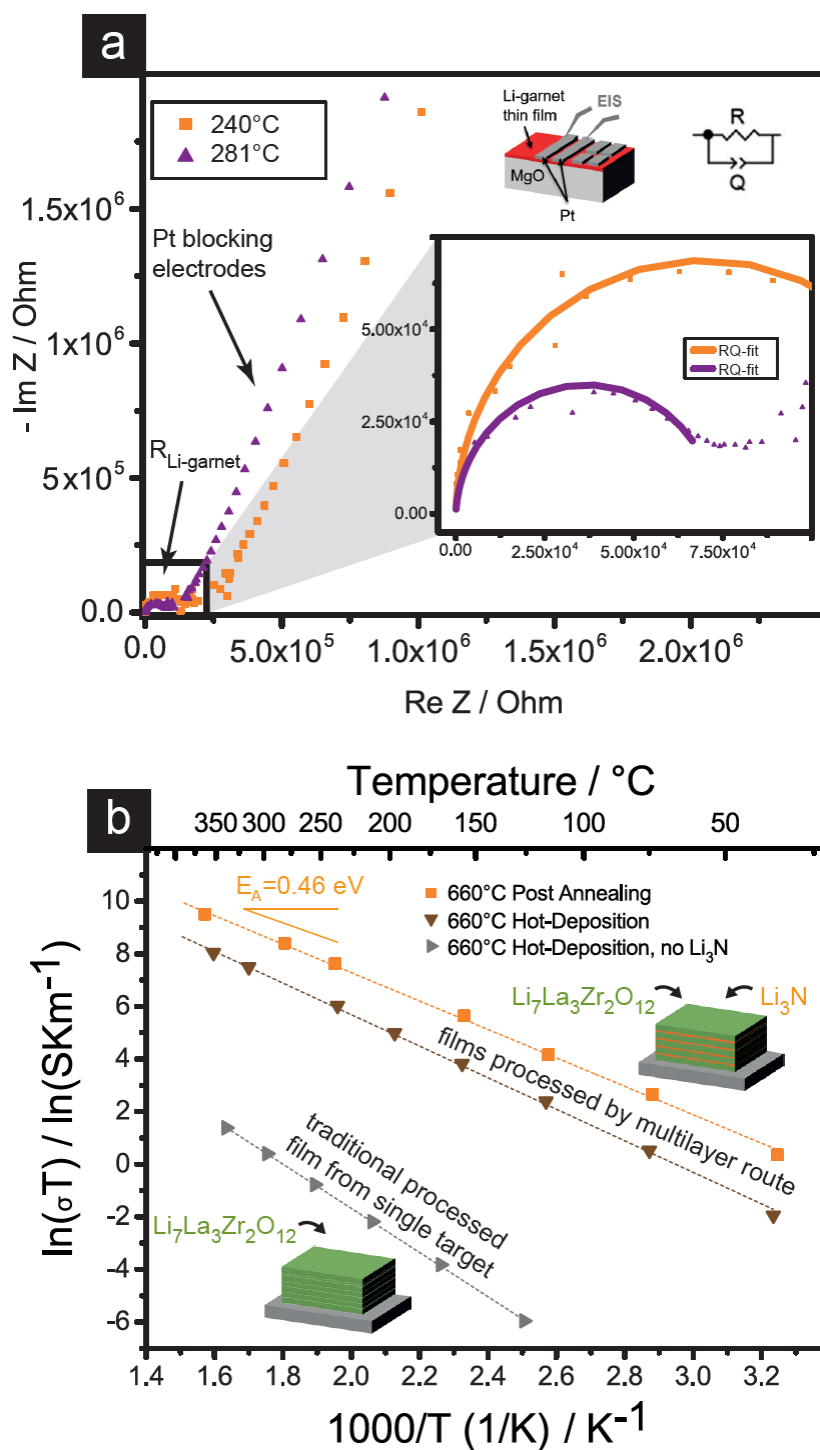
Figure 15 a) Nyquist plots obtained at two selected temperatures of 240 °C and 281 °C from the multilayered LLZO thin film, after post-annealing at 660 °C. The respective fitting (resistor in parallel to a constant-phase-element) is shown in solid lines. b) Temperature dependence of the in-plane total conductivity of selected thin films as a function of the temperature in Arrhenius-type representation. For comparison, a hot-deposited LLZO thin film without Li₃N used for fabrication is shown in grey.

Three different thin films were compared, two of which showed cubic phase in Raman near order investigation: One of the films was deposited at 660 °C directly as multilayered structure with no post annealing treatment, and the other thin film underwent a post crystallization treatment under pure oxygen for 15 minutes at 660 °C. In the direct comparison of the polycrystalline cubic LLZO thin films fabricated by multilayer approaches, either deposited directly at 660 °C or at 300 ºC with post annealing under pure O_2 at 660 °C, the latter did achieve a highest total conductivity of $2.9(5) \times 10^{-5}$ Scm^{-1} ($E_A = 0.46(3)$ eV) at room temperature (23 °C) whereas the hot-deposited reached $0.26(5) \times 10^{-5}$ Scm^{-1} ($E_A = 0.52(3)$ eV). Obtained activation energies are within the expected range for thin film depositions (see Figure 16, 0.32-0.60 eV[177,179]) but clearly lower in direct comparison to pellets (0.28-0.33 eV[169,243]), in agreement with previous reports.

For comparison, we also added conductivity data obtained from a thin film processed from a LLZO target only, aka with no Li_3N used for fabrication, also deposited at 660 °C. In this sample, an extrapolated room temperature conductivity of $5.96(5) \times 10^{-11}$ Scm^{-1} and an activation energy of $E_A = 0.72(3)$ eV was obtained. In conclusion, thin films that underwent a post annealing treatment at 660 °C and were deposited at 300 °C revealed higher conductivity values than those that were hot-deposited at 660 °C. This could be explained by differences in oxygen off-stoichiometry between both films, since post annealed films were exposed to ambient pressure of O_2 during thermal treatment at the highest temperature and therefore facilitated transformation and loss of nitrogen than in the case of low partial pressure of oxygen in the PLD vacuum chamber, when grown directly.

3.12 Advantage of Film Processing with Internal Li₃N Lithiation Reservoirs for Lithium Conductivity in Garnet Solid State Electrolytes

By comparing our results to literature of earlier deposited cubic LLZO through traditional means, Figure 16a, it can be concluded that the film processed through the internal building in of initial Li_3N reservoirs clearly outperforms in effective conductivity; viz. being closest to pellets and tapes so far but at remarkably 400 °C lowered processing temperature. This also manifests in the spread obtained on different thin film deposition techniques with regard to activation energies for ionic transport, Figure 16b. Here, obtained values for the novel multilayer strategies also show facilitated ionic transport with activation energies of 0.46 eV and 0.52 eV, respectively, as compared to 0.72 eV for a thin film without Li_3N.
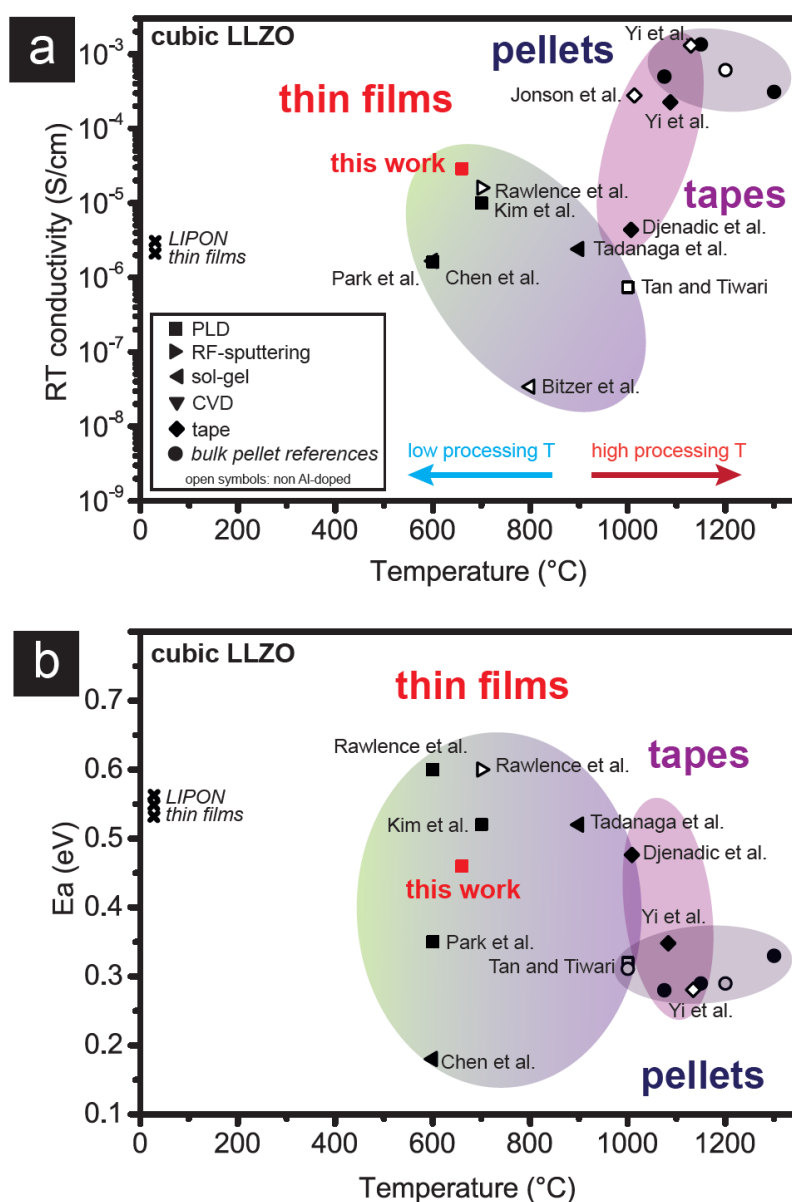
Figure 16 a) Comparison of cubic phase LLZO thin film (<1 µm thickness) Li-ion conductivities at room temperature vs. processing / annealing temperature used. The shape of each datapoint represents the method used for fabrication. Open symbols correspond to LLZO thin films, that contain different dopants than the one used in this study. A comparison to LLZO pellet conductivities is given in round symbols for the doping concentration used in this study[169,243,256] (0.25-Al^{3+} per formula unit) as well as for other dopants,[257] respectively. When compared to literature,[126,134,135,176–179,242] values obtained in this study represent the highest room temperature Li-ion conductivity in thin films of cubic LLZO. The conductivity of selected LIPON thin films[29,191] is shown for comparison. b) Similar graph of LLZO thin film activation energies vs. processing / annealing temperature used. Lowest activation energies have so far been reported for sol-gel deposition techniques followed by PLD deposition. A comparison to bulk LLZO pellet activation energies[71,169,243,256,257] is given in round symbols.

In summary, we compared conductivity of three different thin films of LLZO, two employing the presented approach of Li$_3$N multilayer acting as a reservoir counteracting Li-loss during deposition, and one sample without any Li$_3$N used for fabrication. We conclude that the multilayer processing strategies shown in this work propose a viable route for deposition of highly conductive Li-garnets at significantly lowered processing temperatures.

When comparing the electrolyte performance achieved by the novel strategy of Li$_3$N / LLZO multilayers, it becomes evident that highest conductivity in Li-Garnets – also upon transfer to thin films – is within reach. Since dense and crack-free electrolyte thin films are key components for the integration of high energy and power dense energy storage devices, the assembly of solid state batteries based on multilayer Li$_3$N processing shown in this work will allow for design concepts enabling thin electrolytes without the need for traditional sintering (low temperature processing) and gives room for larger cathode volumes in the overall cell design.

3   Conclusions

All solid state battery Li-garnet electrolytes were fabricated through a new multilayer processing approach using Lithium (Li_3N) reservoirs to establish at an unusually low processing temperature of 660 °C, thin and dense ceramic films with excellent Lithium ionic conductivity. This was achieved by employing a new multilayer approach combining LLZO with Li_3N layers, thus compensating the typical Lithium loss happening during low temperature vacuum deposition approaches of Li-garnet electrolytes. The low band gap of the lithium nitrate is particularly attractive for fast deposition rates and low temperature decomposition to serve the case of being an internal Lithiation source for film processing. The results clearly demonstrate that if such measures are not taken into account for Li-garnet electrolyte processing desired cubic phase cannot be established for the low temperature target or sacrifices on the electrolyte component volume in the battery cell design have to be accepted. Although several processing technology issues require attention, including technologies of cheap best wet-chemical low temperature processing routes, this work opens up a new route for the fabrication of thin solid state battery Li-garnet electrolytes with very high ionic conductivity processed at lowest temperature. In essence, these are interesting candidates for solid state batteries in electric mobility, future microbatteries as they outperform classics such as LIPON electrolyte films, or other type of Lithionic devices such as Lithium operated environmental and chemical sensors.[258]

3   Acknowledgements

This chapter is based on the following manuscript and two patent applications that were submitted for publication:

A Low Ride on Processing Temperature for a Fast Li Conduction in Garnet Solid State Battery Films

Pfenninger Reto, Struzik Michal, Garbayo Inigo, Stilp Evelyn, Rupp Jennifer .L.M.

Nature Energy, 2019, https://doi.org/10.1038/s41560-019-0384-4

AND

The following two patents:

LITHIUM-CONTAINING THIN FILMS (US 62/718,838)

And

METHODS OF FABRICATING THIN FILMS COMPRISING LITHIUM-CONTAINING MATERIALS (US 62/718,842)

Those have been filed jointly by MIT and ETH Zurich based on the invention described in this chapter.

PART IV: Thin Film Battery Cycle Tests for Li_7MnN_4 Anode, $LiNi_{0.8}Co_{0.15}Al_{0.05}O_2$ Cathode and $Li_{6.25}Al_{0.25}La_3Zr_2O_{12}$ Electrolyte Films

4 Abstract

Carbon-free all solid state battery architectures based on fast ceramic Li-Ion conductors have gained a lot of interest, both for large scale as well as microbattery applications. We hereby present a fully CMOS-integrated thin film microbattery based on thin film garnet electrolyte $Li_{6.25}Al_{0.25}La_3Zr_2O_{12}$ combined with high capacity cathode $LiNi_{0.8}Co_{0.15}Al_{0.05}O_2$ and Li_7MnN_4 anode. By utilization of processing conditions within CMOS compatibility (silicon substrate, $T < 300$ °C) we could show proof-of-concept cycling over 26 cycles between 1 V and 4.2 V. On a footprint of only 0.0125 cm^2 and a total microbattery stack thickness of 550 nm, a total energy density of 0.12 $\mu Whcm^{-2}\mu m^{-1}$ and a power density of 2.6 $\mu Wcm^{-2}\mu m^{-1}$ could be achieved.

4 Introduction

The increasing complexity of portable electronics and personal tracking devices leads to a growing demand in new high energy storage solutions offering high gravimetric and volumetric capacity.[180,181] All solid state battery technology arose as promising solution for on-chip integrated energy storage, showing good chemical stability, high 3D stacking potential and increased safety, due to utilization of solid state components only.[142,182] The use of only solid state materials implies a high miniaturization potential, since it is feasible to transfer every single component of the cell to thin films (< 1 μm in total thickness). Together with CMOS (Complementary Metal Oxide Semiconductor) processing compatibility, this opens perspectives for designing new types of energy efficient personal and medical micro devices communicating with each other serving as hardware parts in the Internet-of-Things.[183]

Ceramic all solid state battery electrolytes and architectures have already been successfully transferred to thin film microbattery architectures using predominantly nitrogen doped and glassy Li_3PO_4 (LIPON).[184–186] These have demonstrated potential for powering of portable electronics in the low-power regime, i.e. replacing supercapacitors in chip units such as sensors or actuators.[186,259–261] Utilization of only solid state materials for the battery gives opportunity of using alternative high voltage and high energy density electrodes, such as nitrate-/sulfur[240] or antimony-based[262] electrodes, which are poorly compatible with liquid-based systems.[31,187,188] Furthermore, the use of thin films implies decreasing the thickness of the electrolyte by 2-3 orders of magnitude, with a subsequent reduction of the internal resistance and an improvement of the efficiency of the cell.

A good solid state electrolyte material should show high and pure Li-ionic conductivity, ideally above 1 mScm^{-1} in order to compete with polymer-based ones, high mechanical and thermal stability and high chemical stability against electrode materials.[100,142] When reviewing the field on available solid state electrolytes,[48] highest attention was set on NASICON,[39,44] LISICON,[45,50,190] LIPON,[191] closo-borates,[263–265] LGPS[49,144] and recently on cubic garnet $Li_7La_3Zr_2O_{12}$ (LLZO).[127] In terms of conductivity, NASICON[39] and glassy sulfides[55] offer reasonable ionic conductivity[39] but at the cost of poor stability, i.e. air sensitivity issues.[42,43] Remarkable high ionic conductivity was shown for LGPS (with 12 mScm^{-1} at room

temperature[52]), although only at a narrow stability window around 2 Volts limiting the use of high voltage cathode materials.[53] Looking for a good chemical stability, LIPON was the best option, however, suffering from poor ionic conductivity (1-2 μScm^{-1}), what challenges thin-film microbattery technology to uplift in power density.[32] Opposed to that, garnet $Li_7La_3Zr_2O_{12}$ (LLZO) appears as a very promising option, since it presents both fast Li mobility and a promising stability.[103,240] Fast Li^+-conductivity in LLZO was firstly reported by Weppner et al.,[70] with up to 1 $mScm^{-1}$, although in a thermodynamically unstable cubic phase.[75,76,127] The highly conducting cubic phase can however be stabilized by doping: Introducing dopants in either the Li-site (Ga^{3+}, Al^{3+}, Fe^{3+})[72,78,79,81], the La-site (Ca^{2+} and Sr^{2+})[70,71,82,266] or the Zr-site (Nb^{5+}, Ta^{5+})[71,84,94,266–268] leads to phase stabilization and high conductivity values, e.g. 1.35×10^{-3} Scm^{-1} measured at room temperature in the case of Al^{3+}-doped LLZO.[169,243,256] Moreover, a good stability vs. metallic Lithium has been reported in different works,[95,231,269] allowing for direct integration of the highest possible capacity anode with lowest voltage. Standard processing of the Li-garnets are in the form of sintering to pellets[169,270] or tapes[271] from pressed powders or precursors.

In the recent years, different research groups have focused on the transferability of garnet electrolytes to thin films, for fabrication of microbattery assemblies. However, up to now the deposition of high-conducting LLZO films has shown to be challenging.[126,241] Different deposition methods, such as Physical Vapor Deposition (PVD),[137,174] Pulsed Laser Deposition (PLD),[177] RF-sputtering[171,172] and sol-gel methods[135] have been explored, however, it is still not yet fully understood how the crystalline phase, stoichiometry and ionic conductivity evolve. Most recently, the authors contributed with a detailed analysis on thin film phase evolution and its effect on ionic transport properties for cubic Al-doped LLZO deposited by PLD.[272] Other authors focused on the control of crystallinity, and thus conduction properties of LLZO electrolyte films deposited by RF-sputtering as initiated by Rawlence et al.[126] and a recent study focusing on thin films on Ta/Al-codoped LLZO, deposited by PLD found beneficial conduction properties for low-temperature deposited amorphous films.[241] Still, the need of further advances in the thin film transfer of the electrolyte Li-garnet is reflected in the typically poor ionic conductivity achieved in thin films thereof, usually remaining 3 to 5 orders of magnitude behind the values obtained for bulk ceramic pellets.[171,172,177,242]

Turning to electrode materials, the selection of the appropriate candidates for either anode or cathode in a microbattery setup imposes several constraints upon the system: First of all, only materials that offer sufficient electrochemical stability towards the electrolyte and reveal sufficient stability in air can be employed; which excludes Lithium (also not being CMOS compatible) .[235] In this sense, the utilization of ceramic anode materials in combination with Li-garnet solid state electrolytes became a significant alternative for all thin film microbatteries. Looking at previous literature, main emphasis on the development of thin film electrodes has been explored for pellet based garnet-electrolytes for the following electrodes: *Cathodes* - For $LiCoO_2$ cathodes, see Asaoka et al. who reported capacities of up to 130 mAh/g although with cycling stability challenges.[71,166,198,199] Jin and Mc Ginn[200] reported the use of $LiMn_2O_4$ as cathode electrode on Al-doped $Li_7La_3Zr_2O_{12}$-based cells, also fighting cycling instabilities. Other cathode alternatives include the Nickel-based layered oxides with general formula $LiNi_{1-x-y}Co_xAl_yO_2$, which have been explored extensively in the past.[273–275] Among them, those doped with Aluminum showed highest structural and enhanced thermal stability.[276]

Anode - As for the anode materials, we recently contributed with the optimization of PLD fabricated thin film $Li_4Ti_5O_{12}$ anodes,[270] that was shown as viable electrode materials compatible with bulk LLZO electrolytes and also successfully cycled as stable solid state battery, reaching 90 % of theoretical capacity retention at 2.5 mA/g over 22 cycles. As a rather unusual candidate we consider in this work lithium transition metal nitrides appear,[277] since they show appreciable capacities above 180 mAh/g with best explored stoichiometries of $Li_{3-2x}M_xN$ (M = Co, Ni, Mn), however, these were only tested with liquid electrolytes so far.[278,279] Notably, despite its favorable properties as a battery anode material, broader application of Li metal nitrides has mostly been disregarded due to incompatibility with liquid electrolytes and the very hygroscopic nature of this compound.[280] Through this work, we will explore its use in a thin film microbattery architecture, for which exposure to ambient conditions and humidity can be minimized, since the thin film anode layer is buried under layers of solid electrolyte and cathode.

In this work, we have selected $LiNi_{0.8}Co_{0.15}Al_{0.05}O_2$ (NCA) as cathode and Li_7MnN_4 (LMN) with anti-fluorite structure-type as the anode material and integrate those with Li-garnet thin films for operation in a microbattery thin film architecture, Figure 17a. All components of the

battery in this work, namely anode, cathode and electrolyte, were deposited in the form of thin films. Good thin film processability by various methods (PLD[281–283], RF-sputtering[284,285]) has been reported for NCA, in combination with a good gravimetric capacity of 220 mAh/g, good structural stability and relatively high voltage vs Li$^+$.[286] In the case of LMN, no thin film reports are available in literature, however judging from bulk investigations, a relatively low voltage operation has been reported, with a low plateau at only 1.1 V vs. Lithium and acceptably low volume expansion upon cycling of only around 7 %.[287] We choose Li_7MnN_4 in favor of other nitrides such as Li_7CoN_4 as the anode material, due to its high gravimetric capacity and improved degradation stability over lithium-cobalt-nitride.[278,279] A comparison of the chosen electrodes with other alternatives is presented in Figure 17b, in terms gravimetric capacity as a function of the voltage (vs. Li) in battery cell operation. Here, due to the low voltage plateau of Li_7MnN_4 anode,[279] a remarkable voltage difference of 3.1 V towards the corresponding cathode $LiNi_{0.8}Co_{0.15}Al_{0.05}O_2$ [288] can be noted. Both candidates also offer theoretical capacities of > 200 mAh/g at moderate volume expansion of 7 % or below, showing the good suitability of the individual components selected for this study.[289] Despite their promise, Li_7MnN_4 and $LiNi_{0.8}Co_{0.15}Al_{0.05}O_2$ electrodes have so far not been integrated and operated as a thin film microbattery for Li-garnet electrolyte films.
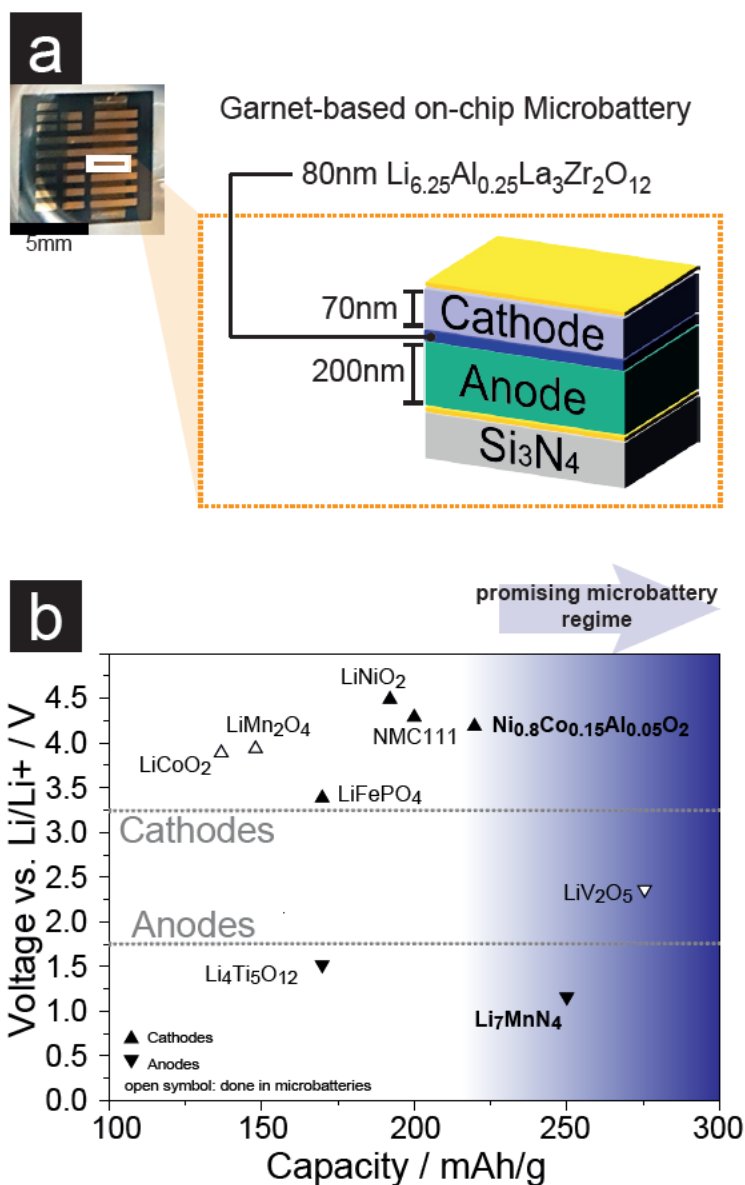
Figure 17 a) Optical image of on-chip battery and its schematic representation of the individual layers. b) Voltage vs. Capacity plot of several battery electrodes. Open symbols represent materials, which have already been integrated in garnet-based microbatteries.[71,103,165,166,169,198,200,231]

All in all, through this work we show for the first time the fabrication and operation of a fully thin film based all solid state Li-ion battery at a total stack thickness of less than 500 nm, combining for the first time thin films of the Li-garnet electrolyte $Li_{6.25}Al_{0.25}La_3Zr_2O_{12}$ and high capacity electrodes. We demonstrate controlled deposition of dense and crack-free thin films of $LiNi_{0.8}Co_{0.15}Al_{0.05}O_2$ cathode material as well as in particular Li_7MnN_4 anode, for which no thin film report had previously been published to the best of the authors' knowledge. Composition and phase analysis was performed on each of the layers individually by growing on single crystalline substrates such as MgO. We investigated the near order vibrational characteristics to confirm phase stability via Raman spectroscopy. Electrochemical Impedance Spectroscopy (EIS) was employed to investigate the conduction properties of each single film. Finally, we probe the lithium dynamics in rate capability upon charging and discharging and study the development of cell voltage and capacity with respect to changing (dis)charge rates. Ultimately, we conclude on the potential of integration of garnet $Li_{6.25}Al_{0.25}La_3Zr_2O_{12}$ as a future electrolyte for microbattery applications. We see a huge prospect for integration and novel battery cells combining all the layers of the battery in the form of thin films based on Li-garnet solid electrolytes as model structures to understand the interface stability and electrochemistry, even for later large-scale battery storage but particularly in the area of microbatteries.

4. Experimental

4.1 Preparation of the Anode, Electrolyte and Cathode PLD Targets

$Li_{6.25}Al_{0.25}La_3Zr_2O_{12}$ powder was synthesized based on a modified sol-gel method reported by van den Broek et al. in Ref.[169] Here, stable sols were obtained by dissolving stoichiometric amounts of $LiNO_3$ (99.99 %, Merck), $La(NO_3)_3(H2O)_6$ (99.9 %, Alfa Aesar), and zirconium(IV) 2,4-pentanedionate (Alfa Aesar) in a (1:1) water and ethanol mixture and calcined at 600–650 °C after drying. Powders were formed in pellets of 32 mm in diameter by uniaxial and then isostatically pressed under 440 bar for 3 min. Thereafter, pellets were sintered at 1050 °C for 12 hours in a bed of parent powder with heating/cooling rates of 10 °C/min. After sintering, a pellet of > 85 % of theoretical density was obtained, dry-polished and stored in an Ar-filled glovebox.

Li_7MnN_4 material was synthesized following solid state synthesis method proposed by Panabière et al[287]. A mixture of Li_3N (Sigma Aldrich, $\geq$ 99.5 %, mesh 80) and Mn powder (Alfa Aesar, 99.95 %, mesh 325) was ground and mixed inside an Ar-filled glovebox using 20 wt.-% excess of Li_3N with regard to the stoichiometric ratio for Li_7MnN_4. The powders were uniaxially pressed at 7 tons for 2 minutes to form a pellet with a diameter of 11 mm, which was isostatically pressed at 1000 kN for 3 minutes. The exposure to humid ambient atmosphere was minimized by sealing the raw powders under the protective atmosphere. Pellets were calcined in two steps in an alumina crucible in a bed of parent powder under the flow of hydro-nitrogen (99 % N_2, 1 % H_2, 50 sccm) with heating rates of 10 °C/min up to 650 °C and 5 °C/min up to 750 °C at which temperature pellets were kept isothermally for 7 hours followed by cooling with 5 °C/min. After sintering, pellets (> 85 % density) were dry-polished and stored in an Ar-filled glovebox.

$LiNi_{0.8}Co_{0.15}Al_{0.05}O_2$ powder was obtained and used as received (Sigma Aldrich, < 0.5 μm particle size, > 98 %). 8 g sample of the material was formed by uniaxial pressing (40 kN, 3 min) followed by isostatic pressing (1000 kN, 3 min) into pellets of 32 mm in diameter. The pellets were polished in order to remove any surface contaminant and sintered in an alumina crucible at 810 °C for 24 hours at heating and cooling rate of 5 °C/min under constant O_2 flow of 50 sccm, following Ramana et al.[283] After sintering, the pellet was again thoroughly polished and stored in an Ar-filled glovebox.

4.2 Thin Film Processing of Li_7MnN_4 Anode, $LiNi_{0.8}Co_{0.15}Al_{0.05}O_2$ Cathode and $Li_{6.25}Al_{0.25}La_3Zr_2O_{12}$ electrolyte

All functional layers of the electrochemical cell were prepared by pulsed laser deposition (PLD) technique using ceramic target of theoretical density > 85 %. The PLD system (PLD, Surface, Germany) was equipped with a KrF excimer laser of 248 nm wavelength at average energy values of 1.5 Jcm^{-2}. All films were deposited at a frequency of 10 Hz with a target to substrate distance of 70 mm with energy of 45 mJ. Background pressures for Li_7MnN_4, $LiNi_{0.8}Co_{0.15}Al_{0.05}O_2$ and $Li_{6.25}Al_{0.25}La_3Zr_2O_{12}$ were 10 mTorr N_2, 10 mTorr O_2 and 10 mTorr O_2 respectively. The temperature of the substrates during all depositions were kept constant at 300 °C, except for the determination of the degree of lithiation in NCA, for which a deposition temperature of 500 °C was used. Two different substrates were used for thin film deposition in this study: (001) oriented MgO substrates (Crystec, Germany) for structural and electrical characterization of each individual layer; Si-wafer with Si_3N_4 coating (PE-CVD) for electrochemical characterization of a full cell. Current collectors were made of 100 nm e-beam evaporated Au (Plassys MEB 550, France) of lateral dimensions of 3.25 × 0.5 mm, either separated 0.25 mm for in-plane AC conductivity (see inset picture in Figure 19b) or stacked between the thin films with an overlapping area of 0.0125 cm^2.

4.3 Structural Characterization of PLD Targets and Thin Films

A structural characterization was performed at room temperature in Bruker D8 X-Ray diffractometer in Bragg-Brentano geometry using Cu K_α radiation ($\lambda = 1.5406$ Å) at an emission current of 40 mA at a voltage of 40 kV. Near order structure was investigated at room temperature by means of Raman Spectroscopy using WiTec Alpha 300M+ system with spectral resolution of 0.7 cm^{-1}. The spectra were collected under excitation of 532 nm radiation at 10 mW of laser power. For the study of the lithiation state of the cathode material, a 633 nm radiation at a low power of 1 mW was used. Note that an increase in intensity can be observed around 95 cm^{-1} due to the edge-filter installed for the wavelength used, which blocked signals < 95 cm^{-1}. We therefore interpret this as an equipment artefact.

Microstructures of the deposited thin films were investigated by scanning electron microscopy (SEM, Leo 1530, Germany) using in-lens as well as secondary electrons detectors.

4.4 Electrochemical Characterization of Thin Films

Electrochemical Impedance Spectroscopy characterization was performed inside a heated Linkam stage (Linkam Scientific, UK) using Zahner IM6 (Germany) Frequency Response Analyzer. The impedance data was collected on a symmetrical cell with Li^+ blocking Au electrodes within a temperature range of 50-400 °C under steady flow of 50 sccm of dry synthetic air with 50 mV AC amplitude in the frequency range of 1 Hz to 1 MHz. Impedance data was analyzed using ZView 3.4f and OriginPro 9.1.

Galvanostatic cycling of the fully ceramic microbatteries was carried out between 1.0 V and 4.2 V inside the Ar (99.99990 % purity)-filled glovebox using a source measurement unit (Keithley 2602B, USA) with own written code (Python)[219]. Characterization was carried out at the temperature of 150 °C. The applied current rate for the following galvanostatic cycling was calculated with the assumption of a dense, homogeneously flat thin film of constant thickness. Rates between 0.12C and 0.6C were applied.

4. Results and Discussion

4.5 Thin Film deposition of functional electrode and electrolyte layers

We first explore the deposition of the electrode and electrolyte materials for the thin film microbattery architecture. For this, we characterize each thin film component separately, addressed by the separate sections in the following.

$LiNi_{0.8}Co_{0.15}Al_{0.05}O_2$ Cathode Thin Film.

We first turn to the investigation of thin films of cathode material $LiNi_{0.8}Co_{0.15}Al_{0.05}O_2$ deposited by PLD on MgO substrates. Films were deposited at temperatures between 300 °C and 500 °C, under an oxygen background pressure of 10 mTorr O_2 from a home-made $LiNi_{0.8}Co_{0.15}Al_{0.05}O_2$ target (the correct phase and degree of lithiation of the bulk target was confirmed by XRD, see Supporting Figure S14 in the Supplementary Information). First, the growth of crack-free and dense cathode layers was checked by cross-sectional SEM imaging, see Figure 18a. Here, a thin film of 250 nm ± 25 nm thickness grown on an MgO substrate can be seen, with a gold top contact of 100 nm ± 10 nm in bright contrast. The phase identification was carried out by Raman spectroscopy, since it allowed us to track the Li content of the deposited films.[290] Presented in Figure 18b, the obtained Raman spectrum for an NCA film deposited at 500 °C is compared with literature reference data of bulk fully charged and discharged $LiNi_{0.8}Co_{0.15}Al_{0.05}O_2$. The film presents a peak around 505 cm^{-1}, which attribute to the A_{1g} stretching mode of the crystalline $LiNi_{0.8}Co_{0.15}Al_{0.05}O_2$ material reference.[283] Centered at a wavenumber regime belonging to the NiO_2 lattice between 450 cm^{-1} and 575 cm^{-1}, this region has been identified to be sensitive in Raman to lithiation degree variations, upon splitting of the main vibrational mode into two distinct modes at 475 cm^{-1} and 553 cm^{-1} respectively.[290] Since no peak splitting was observed in the deposited cathode thin film, our Raman analysis suggested that no severe delithiation upon thin film transfer occurred during deposition. It should be noted here, that films deposited at lower temperatures (300 °C) presented less intense Raman spectra associated to a lower crystallinity, which made impossible the judgement on the lithiation degree by means of Raman spectroscopy. However, no significant differences in terms of Li transfer are expected when reducing the deposition temperature.
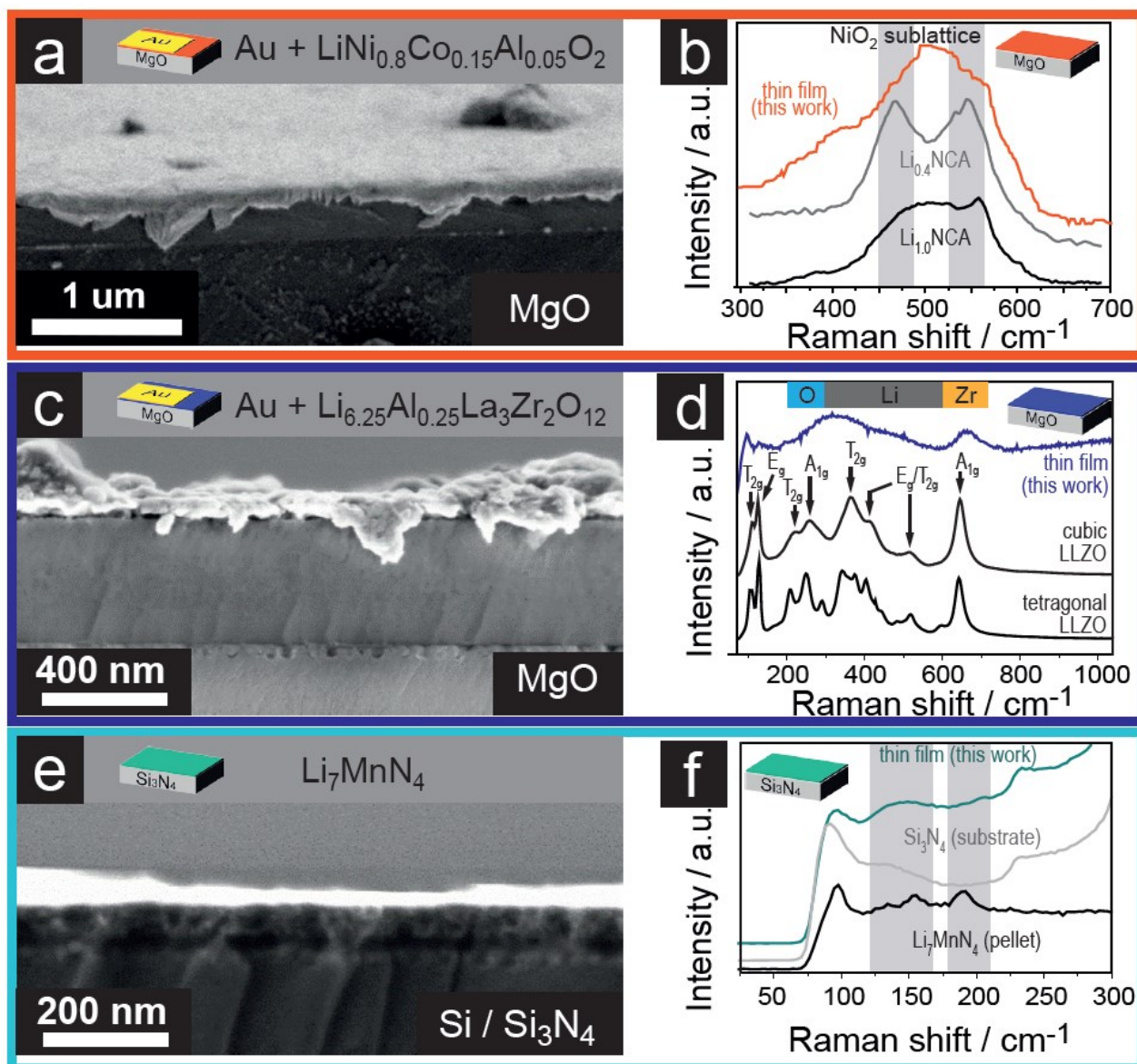
Figure 18 a) Cross-sectional SEM image of 250 nm LiNi₀.₈Co₀.₁₅Al₀.₀₅O₂ cathode thin film deposited on MgO with 100 nm gold top current collector. b) Raman spectrum (633 nm wavelength, 1 mW) of the LiNi₀.₈Co₀.₁₅Al₀.₀₅O₂ cathode thin film in the range around 500 cm⁻¹. Comparison with literature[290] spectra of both, the fully lithiated LiNi₀.₈Co₀.₁₅Al₀.₀₅O₂ (Li₁.₀NCA) and the fully delithiated Li₀.₄Ni₀.₈Co₀.₁₅Al₀.₀₅O₂ (Li₀.₄NCA) confirm the presence of the lithiated state. c) Cross-sectional SEM image of electrolyte Li₆.₂₅Al₀.₂₅La₃Zr₂O₁₂ thin film (400 nm) deposited on MgO with 100 nm gold top current collector. d) Raman spectrum of the electrolyte Li₆.₂₅Al₀.₂₅La₃Zr₂O₁₂ thin film and comparison with corresponding literature spectra of cubic and tetragonal phase of LLZO, taken from Tietz et al.[218,230] e) Cross-sectional SEM image of Li₇MnN₄ anode thin film (100 nm) deposited on a Si / Si₃N₄ substrate. f) Raman spectrum of the Li₇MnN₄ anode thin film and comparison to Raman spectra of the pellet prior to deposition together with a blank substrate reference.

Li_{6.25}Al_{0.25}La₃Zr₂O₁₂ Electrolyte.

Deposition of the thin film LLZO electrolyte was adapted from a previous study by the authors,[241] obtaining an amorphous, but sufficiently Li conducting film (we refer here to Ref.[241] for further details on deposition conditions and properties). An XRD of the electrolyte pellet used for thin film deposition can be seen in Supporting Figure S15. Please note, that an electrolyte of amorphous nature was preferred here, to keep the processing temperature down.[23] Thus, amorphous garnet electrolyte films were grown on top of MgO substrates at 300 °C, see an exemplifying cross sectional SEM image in Figure 18c. Here, a thin film of Li$_{6.25}$Al$_{0.25}$La$_3$Zr$_2$O$_{12}$ with 400 nm ± 40 nm thickness is shown on top of an MgO substrate (a protective gold coating of 100 nm ± 10 nm can be also observed in bright contrast on top of the film). We interpret this as a dense and crack-free thin film with no indication of crystallization, in consistency with Ref.[241] Raman spectroscopy allowed us to analyze the near range order of the amorphous film not accessible by XRD, see Figure 18d. Two broad peaks could be observed around 325 cm^{-1} and 665 cm^{-1}, respectively. Following the Raman crystallization study of Garbayo et al.[241], we assigned the broad peak observed (325 cm^{-1} and 665 cm^{-1}) to the amorphous state described in previous report, where it was found around 335 cm^{-1}.and 670 cm^{-1}, respectively.

Li$_7$MnN$_4$ Anode.

The investigation of the generally hygroscopic thin film of Li$_7$MnN$_4$ anode was carried out on Si$_3$N$_4$ / Si substrate, since this was the target CMOS integrated substrate, which was later on used for the stacked growth of the thin film microbattery. Figure 18e shows a cross sectional SEM image of a thin film of Li$_7$MnN$_4$ with 100 nm ± 10 nm total thickness, grown on a Si / Si$_3$N$_4$ substrate. We observe a homogeneous film as grown by PLD at 300 °C. The microstructure likely showed some degree of closed porosity. It should be noted here, that Li$_7$MnN$_4$ is known for its poor stability in ambient atmosphere and that NH$_3$ outgassing is reported to occur as a degradation process.[280] It is expected that this degradation most likely already started upon the short time of exposure to humid atmosphere needed for measuring the corresponding cross sectional SEM, leading to the observed porosity. A Raman spectra of the thin film of Li$_7$MnN$_4$ anode is presented in Figure 18f, compared to the pellet reference from which the thin film was ablated, as well as a blank substrate of Si / Si$_3$N$_4$. First, the pellet reference revealed two vibrational modes at 155 cm^{-1} and between 180 to 200 cm^{-1}

respectively. Due to the absence of any experimental nor theoretical work on vibrational modes of this material, no assignment to particular mode could be established with confidence. Upon thin film transfer at 300 °C, features of the initial pellet reference could be identified in the observed thin film. We interpret the broad shape of the observed peak with potential amorphous phase contributions though. Since the thin film of this material will later upon cell assembly be in direct contact with lithium-metal-oxides, one may question in this context, whether the combination of such a nitride with only oxides and noble metal as interfacing layers remain structurally functional. Here, reports from Cabana et al.[291,292] shows that even under the assumption of partial oxynitride-formation at the interface to an oxide, the electrochemical performance is rather maintained or improved than deteriorated.

4.6 Electrical properties of the functional films

In order to elicit the ionic transport properties of each single thin film deposited by pulsed laser deposition, we employed electrical impedance spectroscopy for each single layer, in an in-plane geometry and using top gold contacts (see inlet in Figure 19b). A Nyquist-type plot with corresponding equivalent circuit used for fitting (resistor parallel to a constant-phase-element (CPE)) is shown in Figure 19a for 3 selected temperatures of 38 °C, 200 °C and 225 °C for NCA, LMN and LLZO, respectively. Corresponding fitting curves are shown in solid lines. The Li^+ conductivity of the three functional thin films used in this work were calculated from the impedance experiments and plotted in Figure 19b. For the three films, thermally activated Arrhenius-type conduction was found. Highest total conductivity was found for the cathode material $LiNi_{0.8}Co_{0.15}Al_{0.05}O_2$, with an activation energy of 0.20(3) eV. The obtained values are consistent with literature reports, see e.g. Amin et al.[286] Regarding the Garnet electrolyte $Li_{6.25}Al_{0.25}La_3Zr_2O_{12}$, an activation energy of 0.74(3) eV was measured, which is also within a typical range for LLZO thin film electrolytes deposited at this temperature.[241] Finally, for the anode material, an activation energy of 0.56(3) eV was calculated for the thin film. Unfortunately, no comparison to literature was possible in this case, since no report is available for Li^+ conductivity in Li_7MnN_4 thin films. Still, the obtained activation energy was slightly higher than a measured report for a bulk pellet, 0.42 eV.[293] We interpret the discrepancy to be either due to a different microstructure in the thin film, a higher degradation from the larger surface to bulk ratio in thin films, or strain effects, which are known to alter activation energies substantially, also in other kinds of thin film oxides.[213]
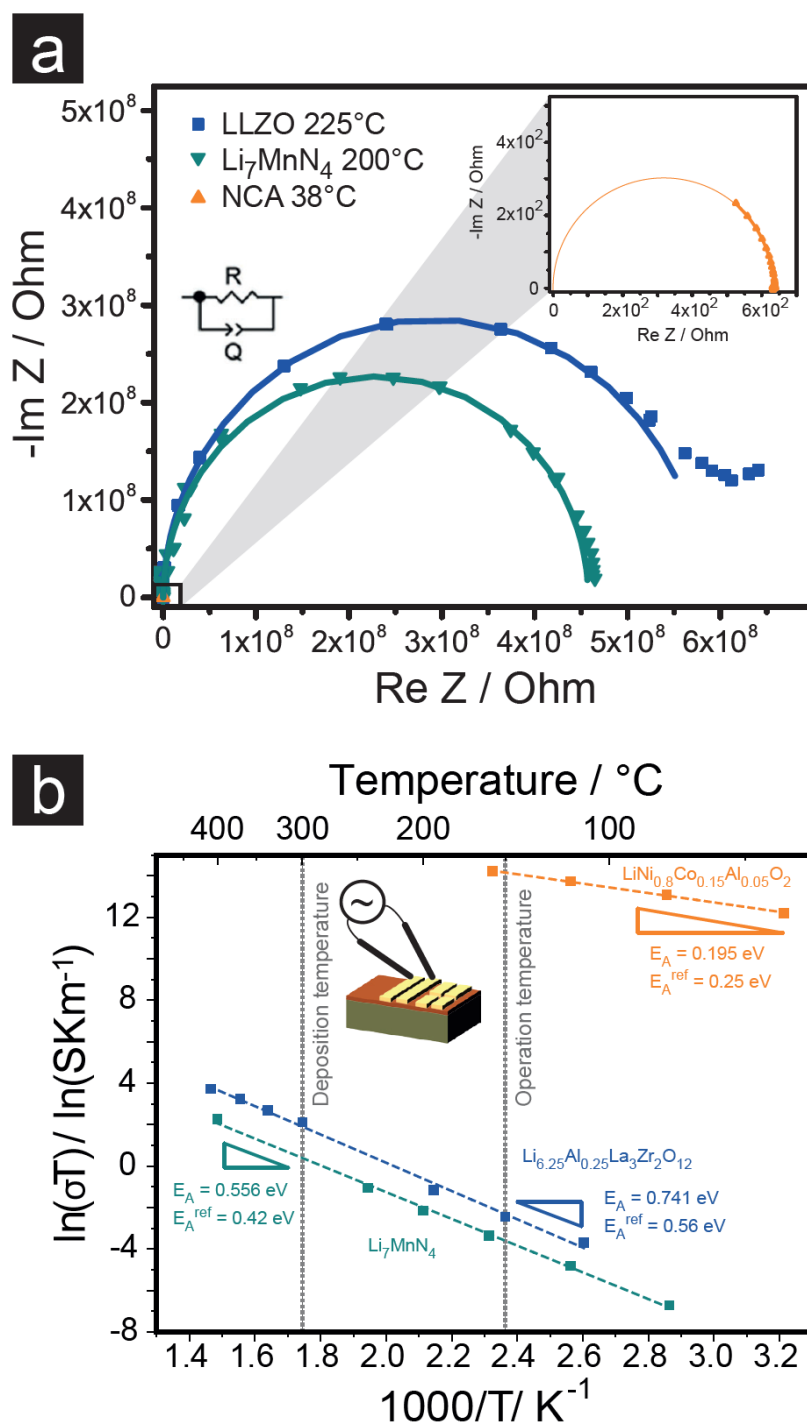
Figure 19 a) Arrhenius-type plot of conductivity and activation energy of anode, electrolyte as well as cathode thin films.[241,286,293] b) Nyquist type representation of the impedance characteristics of the three thin films $Li_{6.25}Al_{0.25}La_3Zr_2O_{12}$ (LLZO), Li_7MnN_4 and $LiNi_{0.8}Co_{0.15}Al_{0.05}O_2$ (NCA) at selected temperatures of 225 °C, 200 °C and 38 °C respectively. The R-Q element used for fitting is shown in the inset picture and fitting results are shown in solid lines.

4.7 Thin film all solid state microbattery assembly

After the full characterization of every single layer, we turn to the fabrication and characterization of a thin film all-solid state microbattery based on the optimized materials. The successful deposition of an all thin film anode (LMN) / electrolyte (LLZO) / cathode (NCA) microbattery stack is shown in the cross sectional SEM image of Figure 20a. The figure includes a corresponding cartoon for the identification of the different layers and their growth order. In bright contrast, two gold layers of 100 nm ± 10 nm thickness used for current collection sandwiching the entire microbattery cell, which consists of a 70 nm ± 10 nm NCA cathode, 80 nm ± 10 nm LLZO and 200 nm ± 10 nm LMN anode. Judging from the observed cross-sectional SEM image, adhesion between all layers, electrode-electrolyte as well as electrode-current collector, seems to establish an intimate contact, however with the expected fast degradation of the delicate LMN component upon measurement. Notably, all the thin films were grown at 300 °C, fully within the processability window of CMOS technology. Again, the strong hygroscopicity of the anode thin film could not be avoided in the SEM technique used for observation. However, in later microbattery operation, this effect is minimized since the battery design was set in such a way that the most critical material (Li_7MnN_4 anode) was kept buried and protected under reasonable gas-/ and humidity-tight coverage of the top oxides and metals. It is important to highlight, though, that SEM imaging shows a strong adhesion of the different layers even though the decomposition of the anode already started. Also, in order to exclude the hypothesis of a potential reaction between the gold current collector and the Li_7MnN_4 anode thin film, leading to a decomposition of Li_7MnN_4, an additional cross-sectional SEM image of the entire microbattery stack without bottom gold contact is shown in Supporting Figure S16, with no visible change in morphology in the Li_7MnN_4 when grown on Si / Si_3N_4 directly.
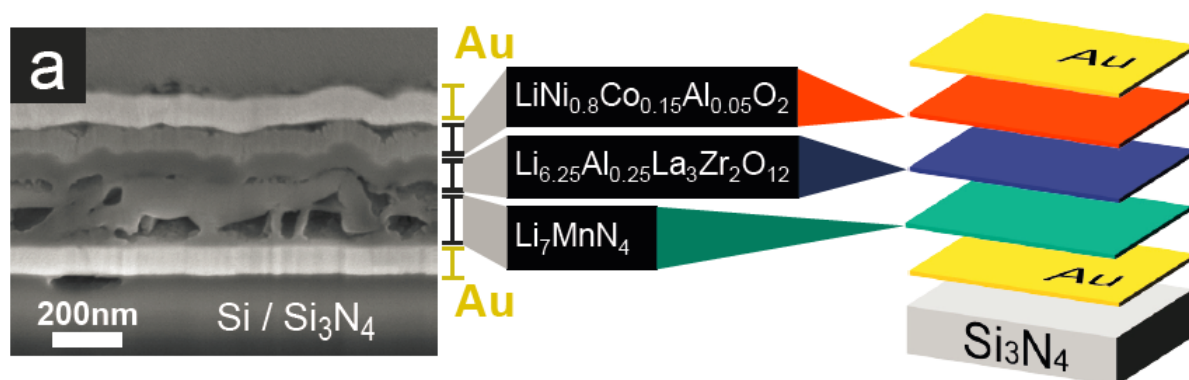
Figure 20 a) Cross-sectional SEM image of complete microbattery stack and its corresponding cartoon representation with Au ¦ Li₇MnN₄ ¦ Li₆.₂₅Al₀.₂₅La₃Zr₂O₁₂ ¦ LiNi₀.₈Co₀.₁₅Al₀.₀₅O₂ ¦ Au integrated on CMOS compatible Si ¦ Si₃N₄ substrate.

An impedance analysis of the full battery stack was carried out as-fabricated, and also after battery cycling (see next section) in order to check possible degradation issues. The Nyquist representation of the impedance measured under two conditions, pre-/ and post-cycling at 150 °C, is shown in Figure 21. Spectra were then fit with a set of 3 Constant Phase Elements (CPE) elements in series and a leading resistor as a model equivalent circuit (see inset circuit diagram in Figure 21). The resulting fitting is shown as a solid line in the same plot. In both cases, two clear semicircles could be observed, one of significantly lower resistance at high frequencies and a larger one at lower frequencies. Due to the complexity of the full cell under investigation, no clear assignment of semicircle with their respective conductivity mechanism could be established. Therefore, we focus our analysis to the evolution of total resistance with cycling. Only a slight decrease in the post-cycling lower frequency contribution could be observed when comparing both spectra, leading to a decreasing of the total resistance from 13.35 kΩ (before cycling) to 12.45 kΩ (after cycling), which corresponds to a decrease in resistance of about 7 %. Therefore, changes in resistance were observed upon cycling, motivating a further investigation of this material system in a follow-up work.
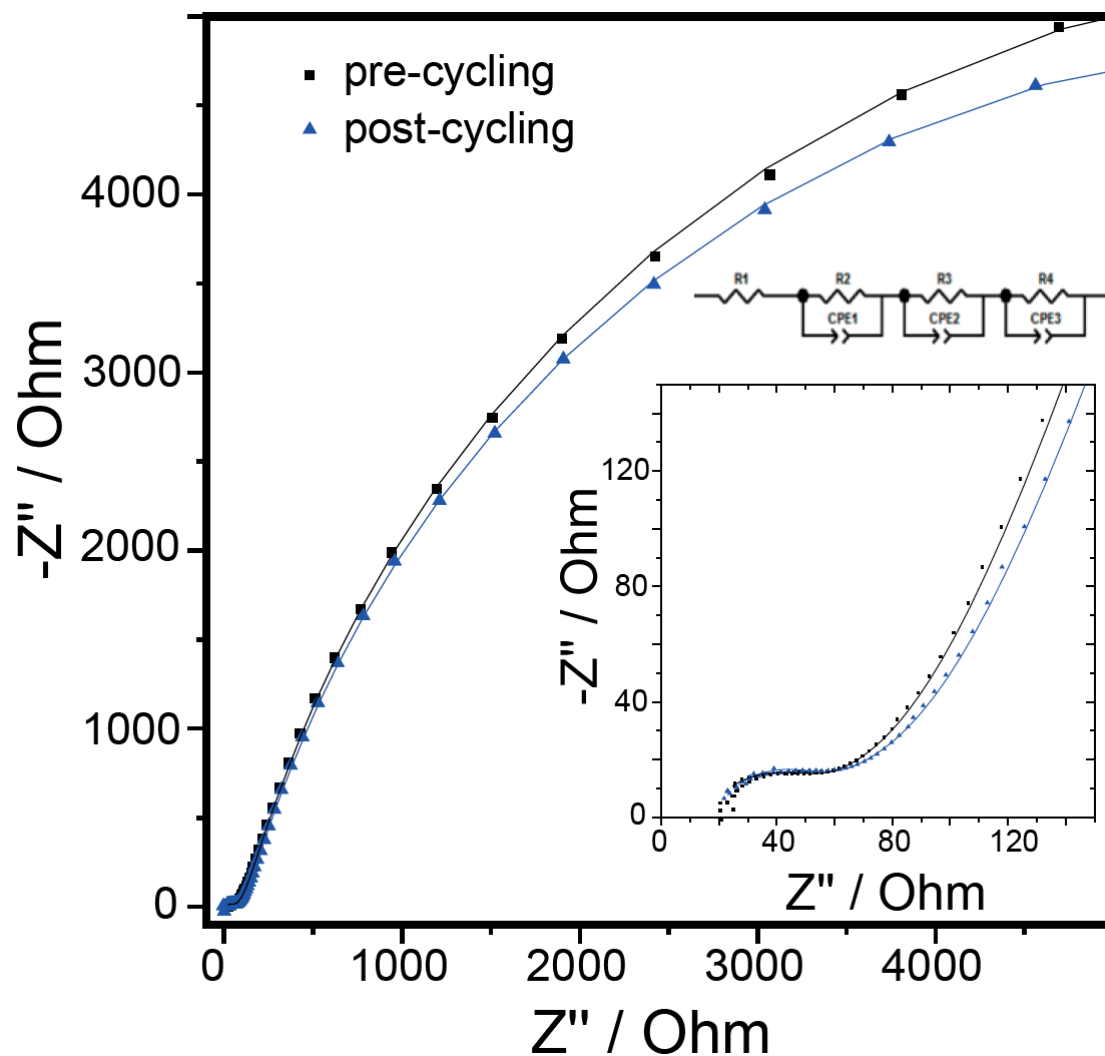
Figure 21 Nyquist plot of microbattery stack pre-/ and post-cycling at 150 °C. The respective fitting (4 resistors, where 3 are in parallel to a constant-phase-element, see inset picture) is shown in solid lines. A zoom-in magnification of the high-frequency part is given in the inset, respectively.

Cycling Performance of thin film all solid state microbattery.

In Figure 22a, we demonstrate successful galvanostatic charge and discharge profiles for a fully thin film microbattery based on the described functional layers over 26 cycles at different rates. Cell voltage vs. gravimetric capacity is plotted in Figure 22b, and a corresponding dQ/dV-plot for cycle number 5 and cycle number 22 was extracted from this data and calculated in Figure 22c. Corresponding oxidation and reduction peaks corresponding to Mn^{5+}/Mn^{6+}, Co^{4+}/Co^{3+} and Ni^{4+}/Ni^{2+} were assigned at 1.1 V, 3.3 V and 3.7 V respectively, as indicated in Figure 22c.

Cycling was conducted at 10 nA (0.12C), 20 nA (0.24C) and 50 nA (0.6C) respectively in the voltage range of 1 V to 4.2 V. In the first 5 cycles a gravimetric and volumetric capacity of 0.8 mAh/g and 0.05 μAhcm$^{-2}\mu$m^{-1} could be obtained that after testing at higher rate even peaked at ~1.4 mAh/g and 0.08 μAhcm$^{-2}\mu$m^{-1} respectively, as shown in the capacity vs number of cycles plot in Figure 22d. Higher rates, especially at 0.6C did lead to severe discrepancy between charge and discharge capacity. This may be attributed to slow kinetics leading to extensive polarization effects. Performance values obtain in this study show the feasibility of Li-garnet based all thin film microbatteries, however only low cycling rates of 0.12C reveal usable capacity.
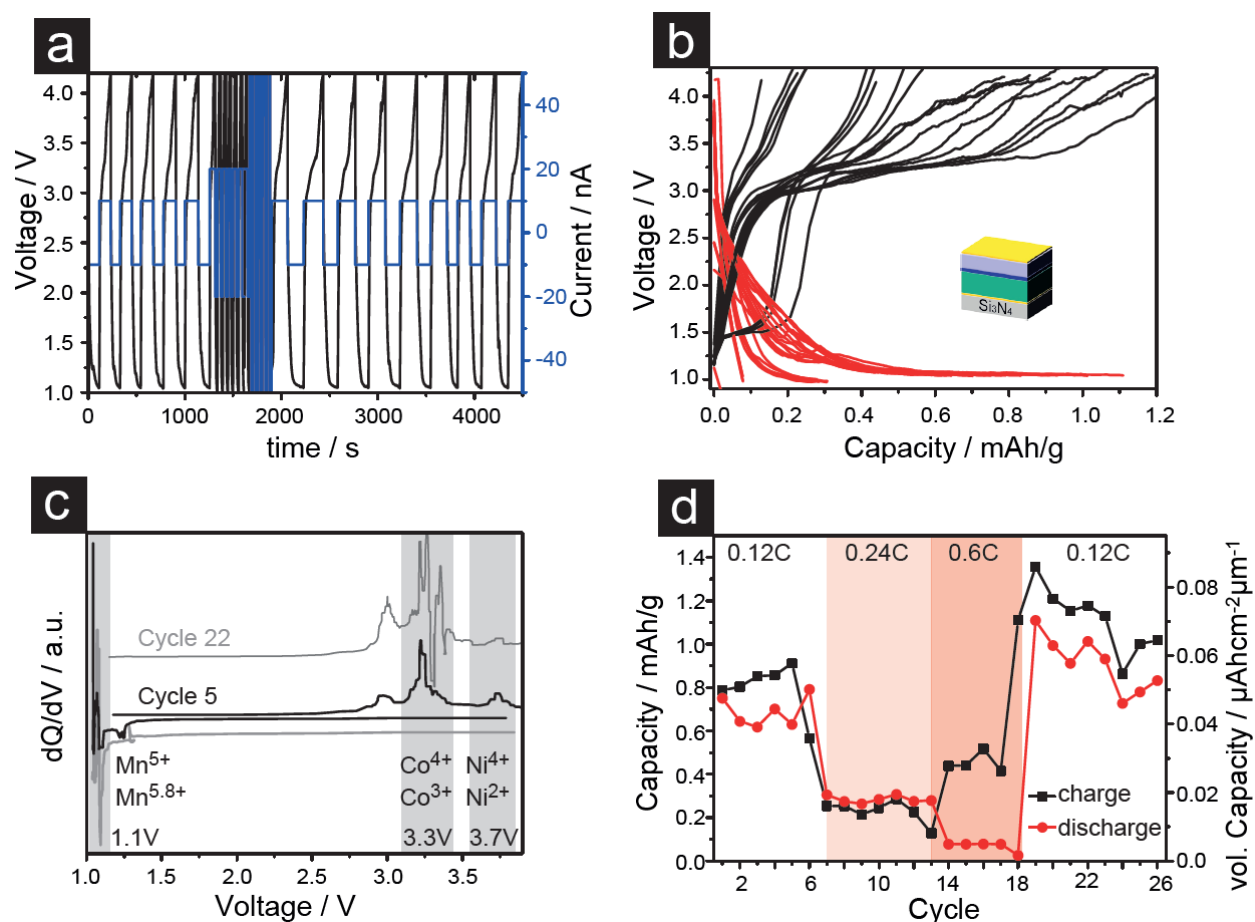
Figure 22 a) Voltage and Current vs. time diagram of the microbattery under operation. b) Galvanostatic cycling profiles during charge and discharge of the microbattery assembly. Cycling took place between 1.0 V and 4.2 V. c) dQ/dV vs. Voltage plot derived and calculated from cycle 5 and cycle 22, with the assignment of corresponding oxidation/reduction peaks of Co, Ni as well as Mn. d) Capacity vs. cycle plot of rate capability of on-chip microbattery. Rates between 0.12C and 0.6C have been assessed.

Advantage of fully ceramic thin film all solid state microbattery based on Li-garnets.

In Figure 23, we compared the achieved results toward values obtained from literature regarding energy and power density in a Ragone-style plot with focus on microbattery performances. Here, best results so far have been benchmarked by Bates et al., achieving 2.5×10^2 µWhcm^{-2}µm^{-1} and $\sim 1 \times 10^3$ µWcm^{-2}µm^{-1} in energy density and power density, respectively, based on a LIPON-integrated microbattery. Values obtained in the present study contribute with 0.12 µWhcm^{-2}µm^{-1} and 2.6 µWcm^{-2}µm^{-1}, for energy and power density, respectively. Even though this study marks a microbattery with all thin film based components on the Li-garnet material class, it already competes in performance with low-end supercapacitors. Intended as a proof-of-concept, this work thereby contributes to first efforts in implementation of Li-garnets to a thin film microbattery.
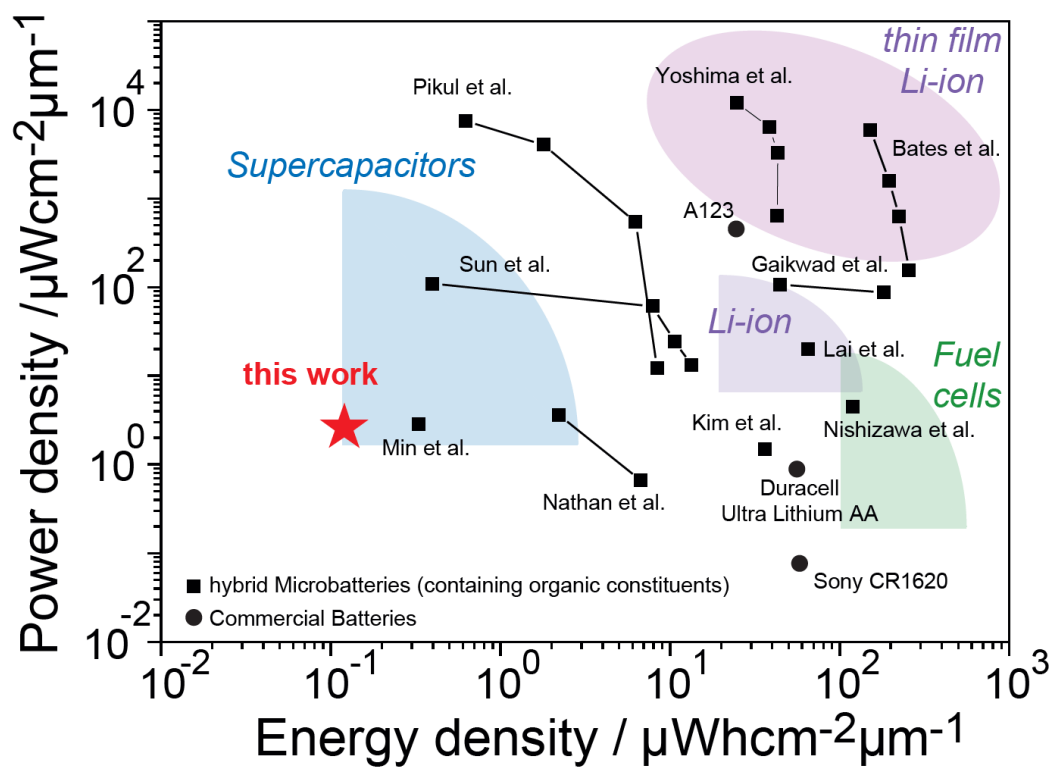
Figure 23 Ragone style plot of power density vs. energy density. Among the different literature references,[31,184,186,259,294–300] this work positions itself as the first report of an all-thin film garnet microbattery.

4.   Conclusion

In this work, we demonstrate the fabrication and operation of a thin film garnet $Li_{6.25}Al_{0.25}La_3Zr_2O_{12}$ based thin film battery, working at a temperature of 150 °C. The rather unconventional anode material Li_7MnN_4 was combined with the garnet electrolyte and a thin film $LiNi_{0.8}Co_{0.15}Al_{0.05}O_2$ as cathode material. A full characterization of every single thin film layer was accomplished, which is especially relevant for the Li_7MnN_4 anode, since it represents the first report in the thin film transferability of this material. The feasibility of the Li_7MnN_4 / $Li_{6.25}Al_{0.25}La_3Zr_2O_{12}$ / $LiNi_{0.8}Co_{0.15}Al_{0.05}O_2$ system working as a thin film battery was proven, with a total thickness of 550 nm and 0.0125 cm^2 of total footprint, an energy density of 0.12 µWhcm^{-2}µm^{-1} and power density of 2.6 µWcm^{-2}µm^{-1}. Remarkably, all processing could be achieved at 300 °C, which is within the thermal compatibility window of CMOS processing, marking its potential interest in on-chip integration of battery components for future remote sensing and implantable medical microdevices. Despite the promise, further work is required to optimize the cell losses and capitalize on the full capacity of the presented battery. We can conclude based on this work, – showing repetitive cycling – that Li-garnet thin film batteries have perspective for future microbatteries.

4.   Acknowledgements

PART V: Development of software tools to perform ultra-low current cycling for microbattery application

This thesis chapter was published as an open source software publication entitled:

5 Abstract

Throughout the experimental progress, the required accuracy for data acquisition was carefully assessed, in particular in the context of microbattery performance evaluation. Microbatteries are predicted to become important components of various microscopic on-chip devices such as sensors or medical devices.[26] In comparison to classical battery cells, microbatteries have very small volumes and masses of the constituent layers. Due to small masses of electrode material found in thin films, combined with the small footprint of on-chip integrated microbatteries, low rate cycling (< 1C) could only be successfully achieved, if the current / voltage accuracy of the applied charging and discharging load equally scaled down with the – orders of magnitude – reduced masses resulting from thin film processing. Here, state-of-the-art instrumentation for cycling at rates of 0.01C in the case of a thin film of 80 nm thickness (see chapter II) or a fully CMOS integrated microbattery (see chapter IV), required us to apply currents as low as 10 nA in a noise-free manner, combined with voltage potential measurements in the range of 1 V to ~5 V. In the following chapter, we will explain, how an *own written codebase was programmed* from scratch, capable of reaching cycling with currents below 100 nA, as well as cyclovoltammetry with high voltage accuracy. The developed software was able to reach minimum applied currents of 10 nA at a resolution of 5 pA and minimum time steps between two measurement data points of 1 ms, outperforming current commercial alternatives, fully compliant with commonly used battery testing techniques such as galvanostatic cycling.

5   Motivation

Especially when dealing with thin film integrated microbatteries, or thin film electrodes of low mass, grown on top of solid electrolyte pellets, high accuracy measurements of current and voltage are of utter importance to judge on the cycling performance of such a cell assembly. This aspect is particularly crucial, since one of this thesis' main emphasis laid on the investigation of compatibility of Li-garnets with *thin film* electrodes: Looking at the microbattery discussed in chapter IV, an NCA thin film electrode of only 80 nm thickness on a footprint of 0.0125 cm^2 was assembled, resulting in an effective cathode mass of only 500 ng. If a testing load for this electrode configuration of 20 mA/g shall be applied, the resulting required current dropped to ~10 nA. Similarly, for the case of the LTO thin film anode from chapter II, with thickness of 80 nm and active area on the pellet electrolyte of 0.38 cm^2, a desired current of 24 nA for a slow rate cycling of 2.5 mA/g can be noted.

In essence, cycling of microbatteries based on thin film electrodes required also the testing equipment being capable to transmit currents at best as low as 10 nA together with high stability of the source and accurate measurement of battery cell response. In Table 4, we summarize performance metrics of commercial battery testing equipment, and compare their minimum applicable current, the maximum accuracy thereof and the time steps, between which two data points can be recorded.

Notably, no commercial system evaluated in this study allowed for the application of currents below 100 nA, as identified to be required for the intended slow rate battery testing for on-chip integrated microbatteries. To accommodate for the lack of market-based technology, we decided to adapt the "smart measurement unit" platform from Keithley™ 26xx series for our measurement purposes. We were able to outperform all available commercial system in 2016, with applicable minimum currents of 10 nA at a resolution of 5 pA. Also in terms of minimum time steps between two measurement data points 1 ms benchmarked – with two orders of magnitude higher acquisition speed – the technical possibilities at that time. The closest commercial system in terms of minimum current was the Maccor™ 4000 series with 300 nA, however at a much worse current resolution of only 30 nA. In terms of acquisition time, the closest commercial system to our own built cycler was Biologic™ SP-150 with 20 ms, still twenty times slower than our own implementation.

The emerging need for suitable testing equipment for nanoscopic energy storage devices therefore motivated the development of an own written software package fulfilling the required measurement speed and accuracy. In order to enlarge the impact of the efforts taken to develop the software suite, we chose to make it publicly available for download, aiding the development of future on-chip integrated energy storage devices.

Table 4 Technical specifications of battery cycling equipment commercially available in 2016, in comparison to our own built setup for nanoscopic microbattery testing. (*) The timespan by which the "ultra-fast acquisition mode" can generate data is limited to a few seconds, depending on the available memory of the system and is clearly below the timespan needed for galvanostatic battery cycling. The speed in a regular continuous mode is fixed to 0.05 s.

Manufacturer / Model	Min. current [A]	Current resolution [A]	Min. Timestep [s]	Reference
Biologic SP-150	1×10^{-5}	7.6×10^{-10}	0.02	[301]
Arbin BT2000	1.0×10^{-5} *(BT-2043)*	2.0×10^{-9} *(BT-2043)*	0.01	[302,303]
Maccor 4000 series	3×10^{-7}	3.0×10^{-8}	0.1	[304,305]
Astrol BATT-SMALL	8.5×10^{-6}	1.5×10^{-7}	0.1	[306]
UMS software (This work)	$\mathbf{1 \times 10^{-8}}$	$\mathbf{5.0 \times 10^{-12}}$	**0.001***	[307]

In the scope of electrochemistry, we also identified a lack on suitable testing equipment on recently studied *general lithiated thin films*, which shall be evaluated for their suitability as memristive logic components in future computing architectures. Such memory devices, also fabricated by our group, were based on thin film processing on similarly small footprints, with the following minor differences in requirements:

- Added need for bipolar chronoamperometric measurements
- Unipolar as well as bipolar voltage cycling for the evaluation of switching capabilities, also at pulse widths ranging from seconds down to ~10 ns, a common switching time in memristive random access memory devices.
- Multiplexing and automated testing on several CMOS fabricated microdots in sequential or parallel configuration, enabling to gather a statistical selection.
- Precise control over environmental conditions during testing such as specific partial pressures of oxygen in an oxygen / argon mixture, thereby controlling non-stoichiometry in oxides.

Due to the growing list of specialized requirements for electrochemistry, we extended the functionality of the package from a single-function → single-output program, to an object-oriented modular system, which can interact with instrumentation specialized for low-current

sourcing (such as Keithley 622x Precise Current Source), high accuracy galvanostatic cycling (such as Keithley 2601, Keithley 2602, Keithley 2612, Keithley 2636) as well as voltage pulsing with simultaneous current measurement down to 10 aA (Keithley 4200-SCS). Electrochemical transport properties were evaluated with home-written specific drivers for the respective impedance bridges Solartron 1260, Zahner IM6 as well as Gamry 600. In order to automatically measure Arrhenius activated conduction, drivers for heat-controllers inside electrical furnaces where added to the package, such as a driver for the commonly used temperature controllers Eurotherm 32xx series, as well as the different low-temperature and high-temperature stages fabricated by Linkam, UK. In order to keep control over partial pressures in experimental chambers during measurement, drivers for gas mass-flow controllers where added such as Vögtlin MFC and Bronkhorst EL-FLOW series.

Upon reviewing suitable software for lab-automation, we discovered that most other research colleagues performing similar measurements used a graphical, script-based programming environment from National Instruments, called LabView™. Unfortunately, this software suite shared a few disadvantages, common to many commercial software products. Those include non-deterministic behavior upon data acquisition, resulting in non-deterministic timing behavior on fast data acquisition, poor reproducibility across different software versions and increasing costs, often in non-perpetual annual license models.

We therefore decided to publish the entire software package as an open source project on "ETH Research Collection" under the copyleft license GPL, by which all functionality can be used by anyone free of charge and code can be reused for future projects with similar needs in the field of electrochemistry.

5   Codebase

The entire software package is written in the python programming language version 2.7 and consists of 12'877 own written lines of code, separated on 51 different files. In order to document code functionality, 2'787 lines of documentation comments were added explaining the code. To facilitate the installation process, the pyqtgraph (http://pyqtgraph.org/) library for real time graphical output was directly bundled with the software as well as the VXI and RPC device communication library specific to Keithley's LAN/LXI communication protocol.

All device drivers for specific lab equipment can be found in a separate "driver" folder. Drivers are designed to run atomistic, they can be implemented in other software projects directly without cumbersome dependencies on third-party libraries. Regarding platform compatibility, we evaluated Linux (distribution Debian, version 7) and Mac OS X as the preferred operating system environments to work with. For a successful installation on either, dependent software libraries, such as the Python programming environment have to be installed first. Additional packages for mathematical computations and graphical output have to be installed as well and where not packed with the software due to their size. Those are in particular python-numpy (and python-pyqtgraph, in case a more recent version is preferred, towards the one bundled with the software).

Since the code is written in a script-based programming language, measurement instruction can be executed directly, with no intermediate compilation step required. Graphical output is generated in real-time, allowing for direct judgment on potential immediate measurement responses, which can be particularly useful for the troubleshooting of electrical contacting.

5 Evaluation and Discussion

The value of precise galvanostatic cycling extends beyond the field of microbatteries and was already extensively pointed out by Dahn and co-worker[308–310] to be of critical importance, especially in the scope of predictions on long term cycling stability in battery cells. With classical methodology, a prediction of cycle life, say after 10'000 cycles, would require years of continuous testing. This is not only problematic since it blocks expensive measurement channels on equipment for a long time, it also delays scientific knowledge-gain on degradation, which can only be extracted and improved after a completion of the protocol. Here, careful monitoring of the coulombic efficiency (CE) can potentially already early on identify potential parasitic reactions happening at very slow rate in each cycle.[311] In order to measure CE accurately, parameters such as error in cell current, cell voltage, temperature and time between measurement data points have to be precisely monitored and controlled up to an accuracy of ± 0.01 %.[308] Applied to our own designed measurement equipment, for an intended testing current of 10 nA for cycling, the required precision quantifies to 100 pA for the current accuracy and no more than 100 μV of uncertainty on the voltage measurement, which are both fulfilled by our equipment which offers 5 pA and 10 μV, respectively.[307] However, there are also quantities in our setup, for which we cannot yet offer the precision required for precise CE measurements, namely the temperature, which also affects the cell voltage, and which we only control within the range of ± 5 °C (required: < 1 °C). Accurate temperature control during galvanostatic cycling of microbatteries presented in this thesis, would therefore require an environmental chamber inside an Argon-filled glovebox, with embedded micro-positioners for thin film electrode contacting. Obviously, the engineering required was therefore beyond the scope of this work, and focus was set on low-rate cycling of thin films only, with the option for a potential experimental upgrade in a continuation of this work. In summary, the presented setup is well suited and prepared for high precision CE measurements, though with minor modifications on more advanced temperature control.

One may now curiously ask, why the essential and necessary effort on precise measurement of low current and voltage were taken, and why not simply higher-mass cathodes were applied, for which currents in the milli-Ampère range would have been adequate? Here, four main aspects were identified as clear benefits for the investigation of thin films instead:

- In thin films, a high interface volume is present, which form the boundary towards new electrodes and electrolytes, towards which we try to investigate compatibility as a main focus of this thesis. A higher fraction of "interface effects" contributing to macroscopic measurements such as in galvanostatic cycling is therefore expected to enhance and pinpoint our compatibility assessments.

- The Li-garnet material class so far lacks a method for thin film transfer of high ionic conductivity by pulsed laser deposition. If the electrolyte is deposited in thin film, it is likely that only at low current rates, ionic motion will be sufficient for cycling, especially with the poor expected conductivity, in case the recipe for deposition is still not optimized.

- Thin film deposition of uncommon electrode materials such as Li_7MnN_4, which have never been implemented in solid state battery designs, or olivine-type cathodes, for which compatibility towards Li-garnet is unexplored and poor conductivity is expected, will be more forgiving in terms of current-collection, for which no sophisticated conductive additives with unknown cross-effects have to be developed.

- Slow rate cycling – in general but also on thin film electrodes – comes at the clear advantage of a more accurate description of oxidation and reduction potentials in dQ/dV, for which highest rate cycling would not allow for a clear assignment and interface incompatibilities could go unnoticed.

With those aspects and the necessary requirements on data acquisition in mind, we evaluated suitable measurement equipment, for which we rated the Keithley 26xx series as the most suitable instrumentation for our specific purpose. With a customized feed-trough for electrical contacting of microbatteries and half-cells on hot plates inside the Argon-filled glovebox, we completed our setup. Cycling of thin film electrodes in combination with Li-garnet electrolytes – either in the form of a bulk pellet, or as a thin film electrolyte – could successfully be shown, the implementation of own written software in conjunction with high accuracy instrumentation pave a new route toward thin film microbattery testing.

5   Conclusion

Throughout this thesis, we identified a lack on suitable equipment for assessing the performance of our intended microbattery architectures, for which we developed our own toolset from scratch.

With a continuous effort over the entire course of this thesis, and the help of co-workers, in particular Eva Sediva and Sören Boyn, the software package quickly grew in maturity. The modularity of the system in combination with its real-time graphical output allowed for an adoption of the system also from microbattery tests to other fields such as for memristive memory testing, fuel cell testing and controlling of solar-to-fuel reactors, making automated testing and easy data analysis a reality. Extensive documentation for both, source-code and a manual in PDF form, which explains all functionality, was also written in the hope that the tool proves its usefulness for future generations of engineers to come.

This chapter was based on the following software publication that was submitted for free download:

PART VI: Summary and Outlook

6 General Conclusion

In the bigger picture, the aim of this thesis was to design and understand novel Li-garnet based all-solid state batteries and their interaction in contact with oxide and nitride electrode materials. We started by synthesizing bulk, dense ceramic bodies of cubic garnet electrolyte pellets with the stoichiometry $Li_{6.25}Al_{0.25}La_3Zr_2O_{12}$ and extended our study to the fabrication of suitable electrode materials. Here, the zero-strain anode material $Li_4Ti_5O_{12}$ was of particular interest and was synthesized in its lithiated state, which allowed for successful thin film deposition by pulsed laser deposition on top of the electrolyte pellet. $Li_4Ti_5O_{12}$ as a model compound of a well-understood anode material in liquid-based battery cells gave the opportunity to investigate for the first time the compatibility of a thin film anode material in combination with garnet electrolytes in general.

We showed through investigation via Raman spectroscopy, scanning electron microscopy as well as galvanostatic cycling under varying rates, the feasibility of $Li_4Ti_5O_{12}$ as an anode material in combination with garnet electrolyte and also showed that the system Lithium metal ¦ bulk garnet pellet ¦ $Li_4Ti_5O_{12}$ thin film ¦ copper current collector, could be cycled to higher than 90 % of its theoretical capacity of 175 mAh/g, therefore benchmarking the capability of thin film anode in the garnet material class.

In a further step, the search for novel materials – in particular high capacity anodes – was extended from oxides to nitrides. Here, the unconventional choice of Li_7MnN_4 was taken to successfully assemble this rarely used anode material in thin film form and characterize its thin film transport properties by impedance spectroscopy. Its poor stability and degradation in humid air has always been a severe issue and could only be addressed by several design decisions: i.) minimized exposure upon thin film transfer ii.) employment of a microbattery cell design, in which the anode was buried under the electrolyte material and therefore protected by the substrate as well as electrolyte from exposure to detrimental environmental conditions.

119

The combination of those key principles allowed for the assembly of a stacked microbattery on a Si / Si_3N_4 substrate, employing $LiNi_{0.8}Co_{0.15}Al_{0.05}O_2$ thin film cathode, $Li_{6.25}Al_{0.25}La_3Zr_2O_{12}$ thin film electrolyte and Li_7MnN_4 thin film anode. By this, the first successful fabrication of a fully thin film microbattery with garnet electrolyte could be demonstrated to the field. Notably, all processing conditions during the fabrication of this first garnet-based microbattery could be maintained at a temperature of 300 °C, which is fully within the compatibility window of CMOS processing. Inspired by the first success in a full thin film microbattery based on a *nitride* electrode, very soon the idea came, to explore further nitride compounds to also functionalize garnet LLZO thin films.

In this context, first experiments on Li_3N in combination with garnet LLZO where conducted. The assumptions made behind the choice of this particular combination of materials was that Li_3N would – at elevated temperature – decompose and release N_2 and then leaving a lithium reservoir, that could then be subsequently incorporated into the garnet LLZO framework, assisting in the formation of the highly conductive cubic phase.

As it became apparent during first tests, a multilayered thin film structure with 9 repeating layers of Li_3N and LLZO could exactly serve as a model system to explore this mechanism. We used the heterostructure Li_3N / $Li_{6.25}Al_{0.25}La_3Zr_2O_{12}$ to study the phase evolution and formation of garnet phases upon thermal treatment in the temperature range of 300 °C to 980 °C. This was achieved through ex-situ and in-situ Raman spectroscopy as well as characterization of the resulting transport properties in thin film samples by electrical impedance spectroscopy.

In summary, we found that two different strategies could equally lead to the formation of the highly Li-conductive cubic phase in LLZO. Firstly, by deposition of a multilayered structure at 300 °C, followed by an external post-anneal treatment at 660 °C under pure oxygen, and secondly, by direct deposition of the multilayered structure at 660 °C. In terms of electrical transport properties, so far highest thin film conductivity could be reported on the thin film of $Li_{6.25}Al_{0.25}La_3Zr_2O_{12}$ with $2.9(5) \times 10^{-5}$ Scm^{-1} at room temperature, and an activation energy $E_A = 0.46(3)$ eV.

In parallel to the above-mentioned experiments, it also became apparent that current measurement equipment used for classical liquid-based battery testing was not optimized and designed to work and assess microbattery performances. Either the stability of the output

current was insufficient, resulting in signal ripples or the minimum output current, which could be set for galvanostatic cycling, was not in the required low nano-Ampère range, needed for such small battery cells of only 550 nm total thickness. This inspired the development of an own measurement software, called UMS, capable of cycling nanobatteries at fixed and stable galvanostatic currents of only 10 nA in the voltage range of 0-10 V. The great acceptance of the lab software I wrote, also lead to a broad extension of the codebase to now over 10'000 lines of code, with its capabilities extended to cyclovoltammetry, automated impedance acquisition, memristor-testing as well as ultra-short pulsed memristor testing.

In conclusion, several aspects around microbatteries could be addressed in the following thesis. In the first part, main focus was set on the Li-garnet $Li_{6.25}Al_{0.25}La_3Zr_2O_{12}$ and its compatibility with several electrode materials such as $Li_4Ti_5O_{12}$, Li_7MnN_4 and $LiNi_{0.8}Co_{0.15}Al_{0.05}O_2$. We could successfully show for the first time an operational cell of a *thin film anode* in combination with Li-garnet. We also demonstrated in this work the first *all thin film based microbattery* utilizing LLZO as the electrolyte. A lucky discovery on the novel Li_7MnN_4 anode material, which worked in a microbattery, led to the deeper investigation of nitrides in combination with Li-garnet. Since thin film depositions of Li-garnet have so far been challenging, and the stabilization of the highly Li-conductive crystallographic phase could not be achieved through pulsed laser deposition so far, the novel idea of multilayer deposition with sacrificial Li-reservoir Li_3N and thermal post-annealing could successfully solve this issue.

6   Outlook and Future Challenges

The achieved highest conductivity for thin film Li-garnet solid state electrolytes reported in this work through the new nitrate multilayer and post anneal processing may contribute to the development of novel and powerful microbattery architectures. Processing of own microbattery architectures revealed that more work is required to identify the rate determining steps and suitability of best electrode arrangement for such microbatteries. For example, the compatibility of other electrode materials such as sulfur-based cathodes or silicon / antimony-based anodes is of equal importance, even though it remains undiscussed, and one can expect exciting new combinations of lithiated garnets, both in bulk and thin film form, with electrodes that may improve on stability and cyclability.

Another important priority of future development in the field of energy storage has to be set on environmental aspects, such as the use of abundant elements and non-toxic choices of electrode materials, especially if solid state battery technology should soon make its way into portable electronics and transportation. In best case, future research efforts should also be directed into the avoidance of socio-economically critical elements such as cobalt, which is mainly mined in the Democratic Republic of Congo, often involving exploitation of workers and child labor.[22]

Here, research has the unique opportunity to show paths and sustainable ways to future energy storage, based on non-critical elements that one should not leave unattempted.

Lithiated thin films not only start to play an emerging role in energy storage applications, but also in novel "Lithionic" memory and sensing devices, for which fabrication and characterization urge solid understanding. Here, the fundamentals, such as showing a proof-of-concept of a first working microbattery based on this material, or the deposition of the cubic phase in thin film form, may inspire future research on this relevant and important topic of lithiated garnet electrolytes, which also deserves a lot of attention in a continuation of this work.

PART VII: Appendix

Supplementary Information Part II
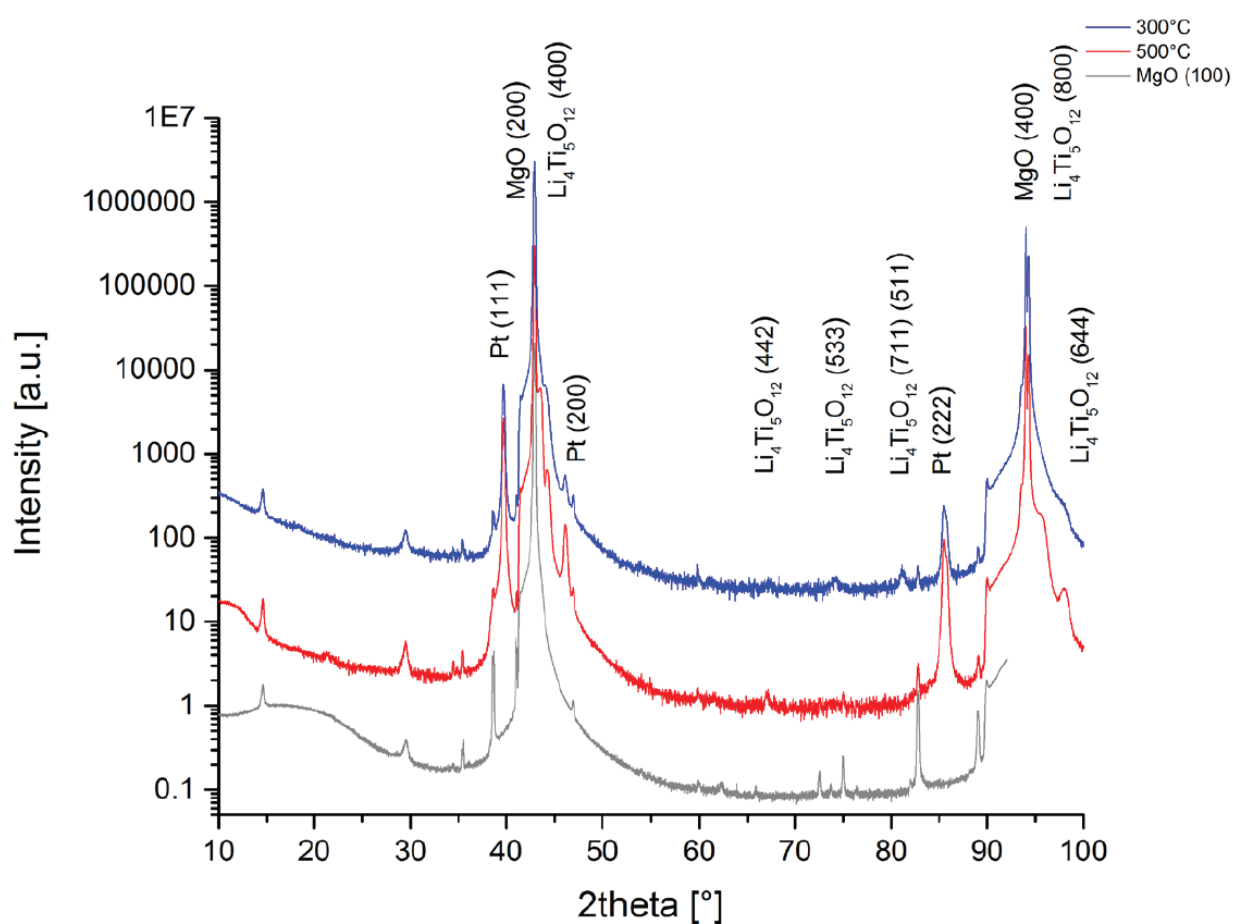
Figure S1 Thin film XRD spectra of LTO thin films deposited at 300 °C and 500 °C with corresponding comparison to Platinum metal, $Li_4Ti_5O_{12}$ literature reference and substrate background.
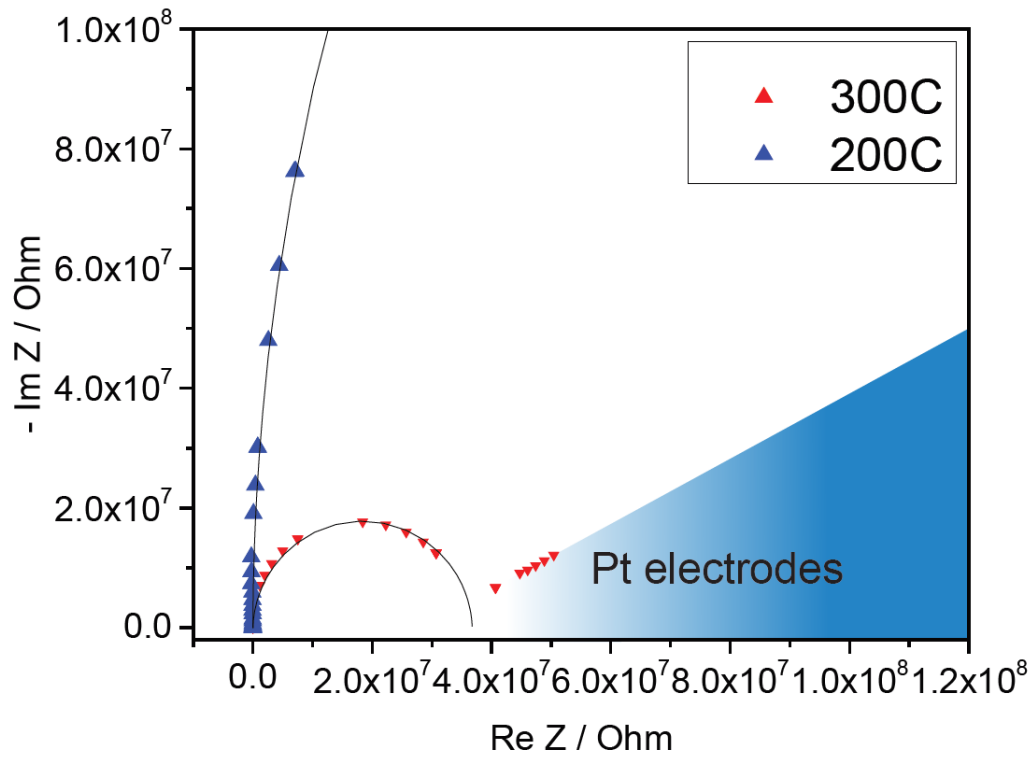
Figure S2 Nyquist representation of the impedance recorded at 200 °C and 300 °C, respectively. The fitted equivalent circuit is shown in solid lines.
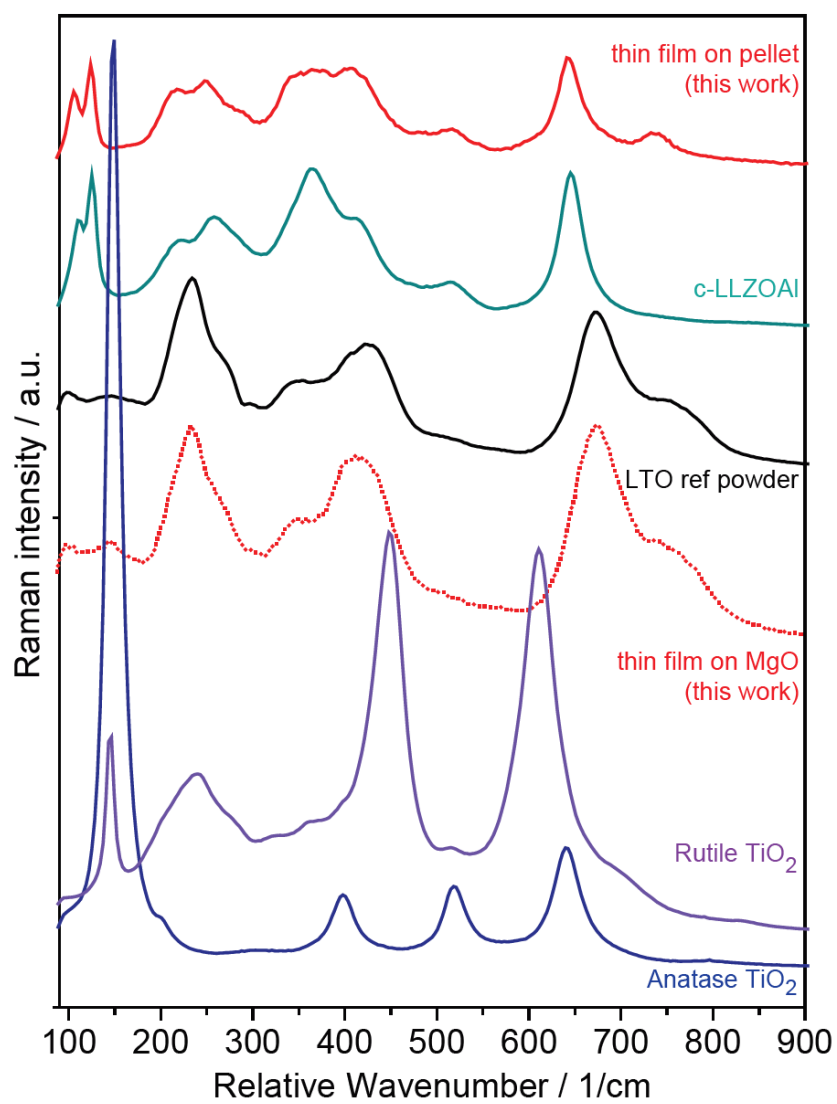
Figure S3 Raman spectra of the thin film deposited on the pellet in comparison to powder spectra of the most common delithiated impurity phases of TiO₂ (anatase and rutile).
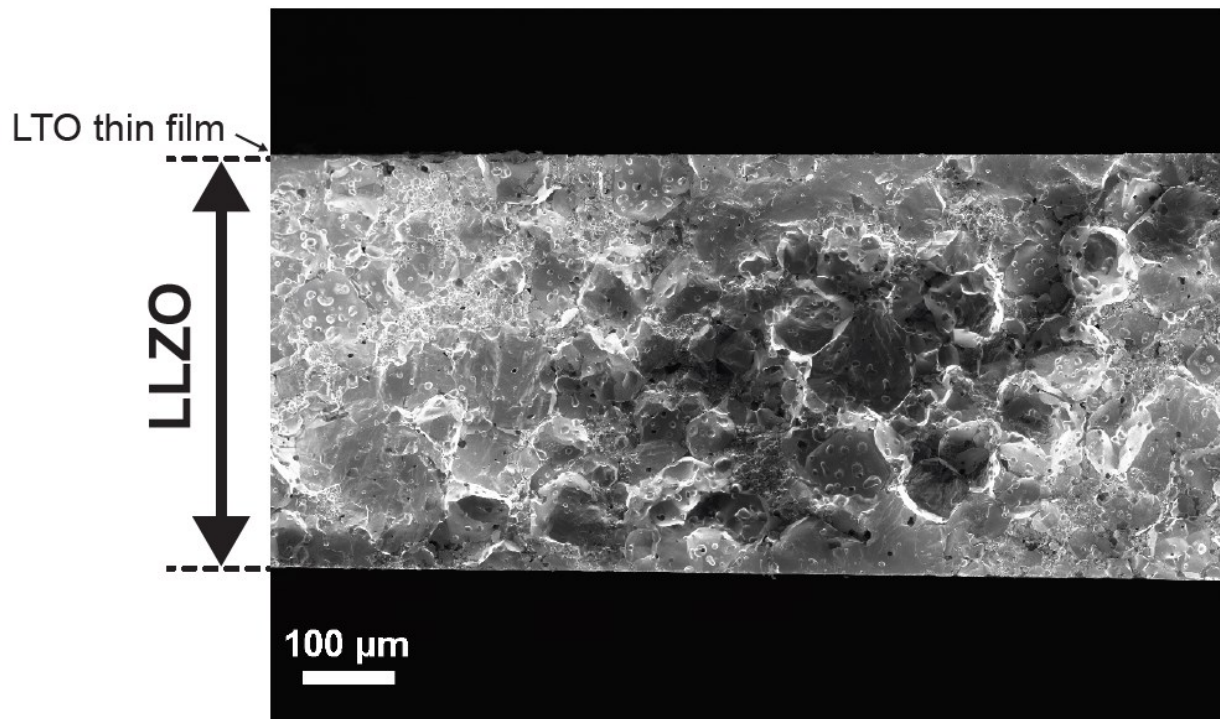
Figure S4 Cross sectional SEM image of the polished pellet with thin film on top.
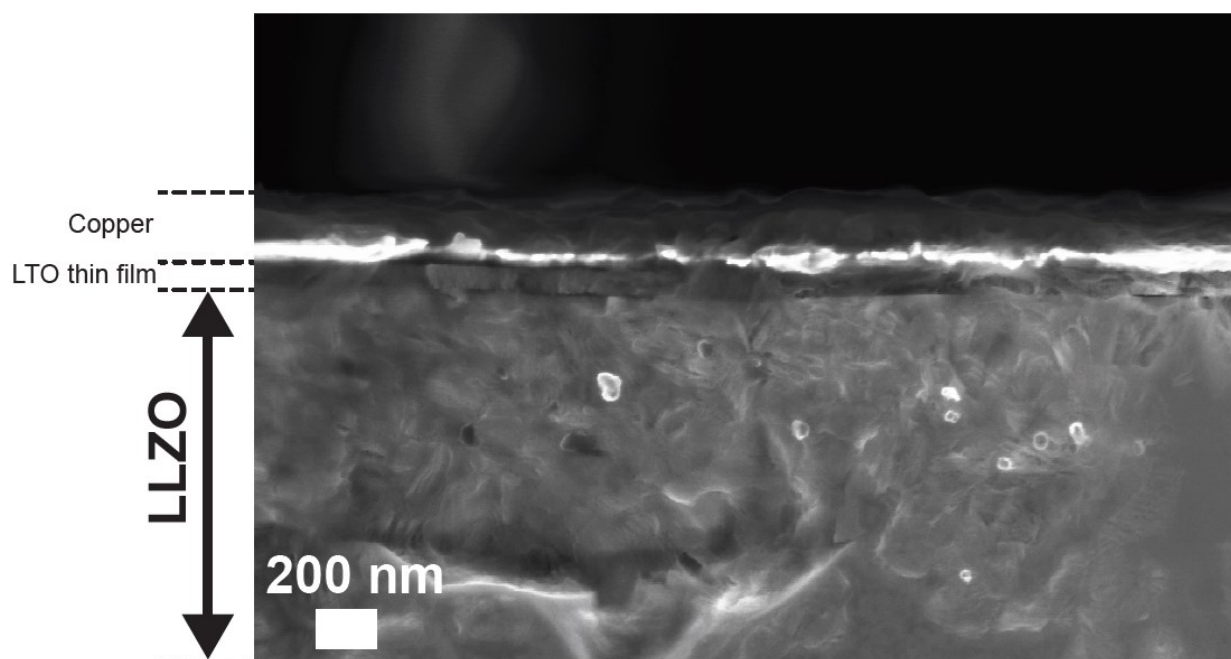
Figure S5 Cross-sectional SEM image of the same pellet after deposition of 100 nm copper current collector.

Supplementary Information Part III
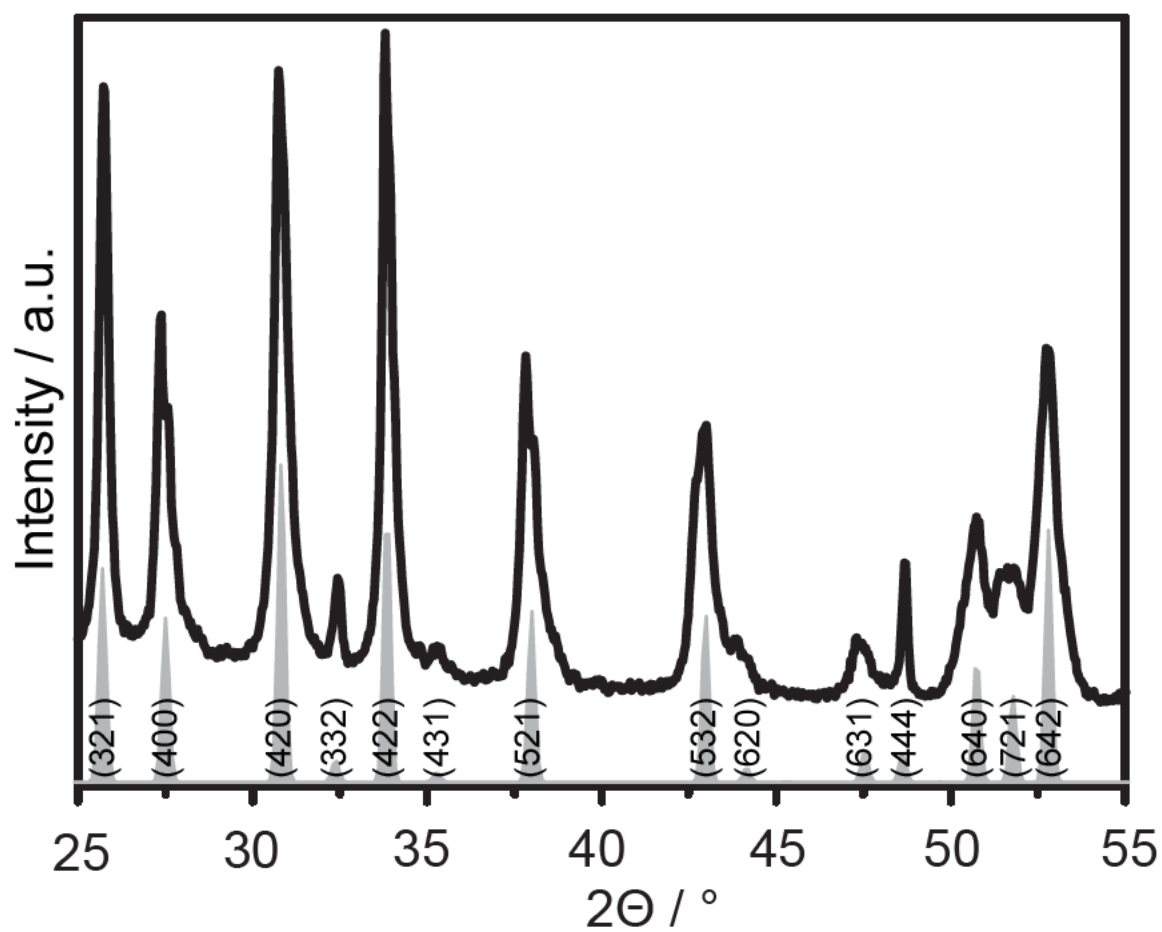
Figure S6 To confirm of the correct crystallographic phase of the target material in use, a dense pellet of cubic $Li_{6.25}Al_{0.25}La_3Zr_2O_{12}$ was analyzed by XRD. A comparison to ISCD185539 is given in grey bars.
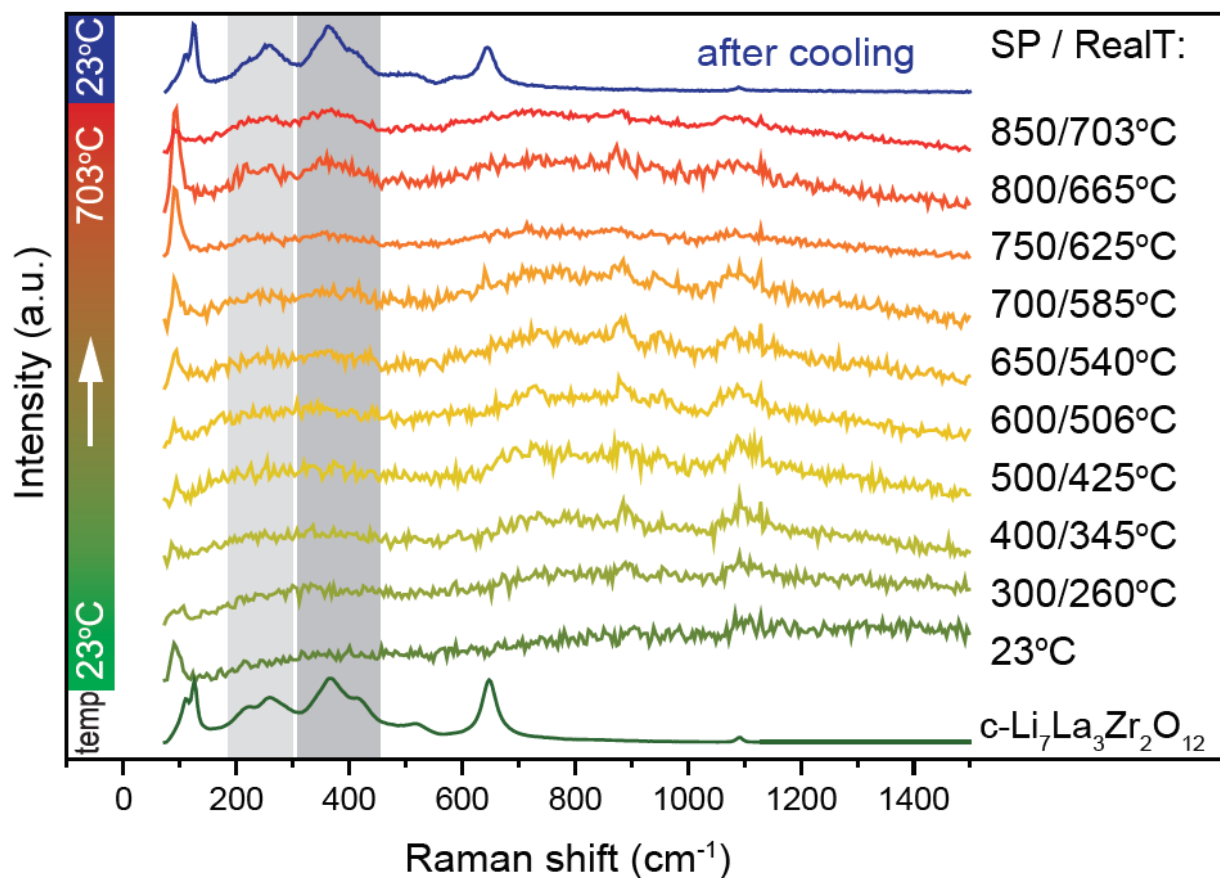
Figure S7 The observation of the transformation from Li₃N / Li₆.₂₅Al₀.₂₅La₃Zr₂O₁₂ multilayered electrolyte thin film could also be observed in-situ by heating a sample to different temperatures while at the same time observing its Raman signal. Due to the long working distance of sample inside heater and Raman microscope, only a low numerical aperture 50x-lens could be used leading to much higher background noise levels than for the study conducted ex-situ. Still, similar conclusions than in the ex-situ analysis could be attained, and a temperature range of 23 °C-700 °C was found adequate for the crystallization of cubic LLZO from the grown multilayers.

In-situ Raman was mainly performed to assess the annealing times required to obtain the different phases. Surprisingly, – unlike in pellet processing of LLZO – in-situ Raman indicated that already 15 minutes of annealing time at each of the measured temperatures was sufficient to establish the respective phases over the entire surface of the thin film. Based on this results, 15 minutes was fixed as the annealing time for the ex-situ experiments.

To assure that the initial multilayer thin film merged to form a homogeneous cubic LLZO film, additional cross-sectional SEM images have been taken. As observed in the following 3 figures, this was also attained for the fabrication approaches of direct deposition at 660 °C without a further post annealing step.
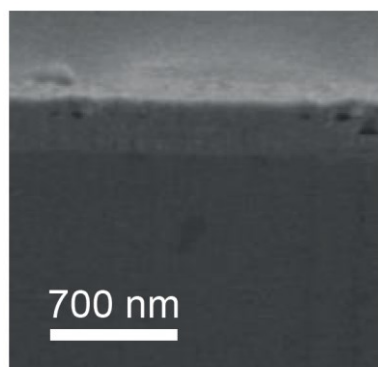
Figure S8 Cross-sectional SEM image of a thin film fabricated direct deposition as a multilayer structure at 660 °C.
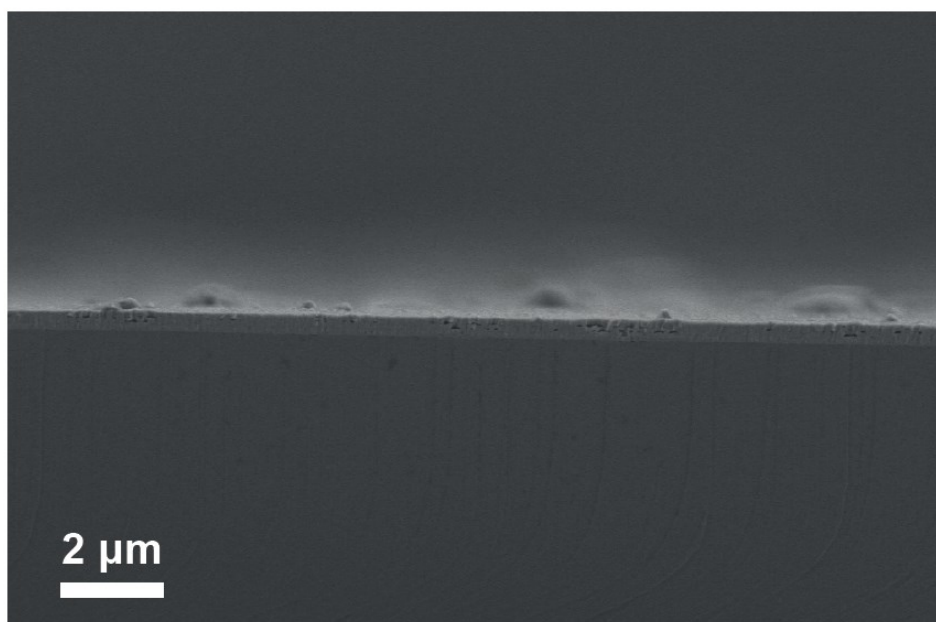
Figure S9 Cross-sectional SEM image of a thin film fabricated direct deposition as a multilayer structure at 660 °C.
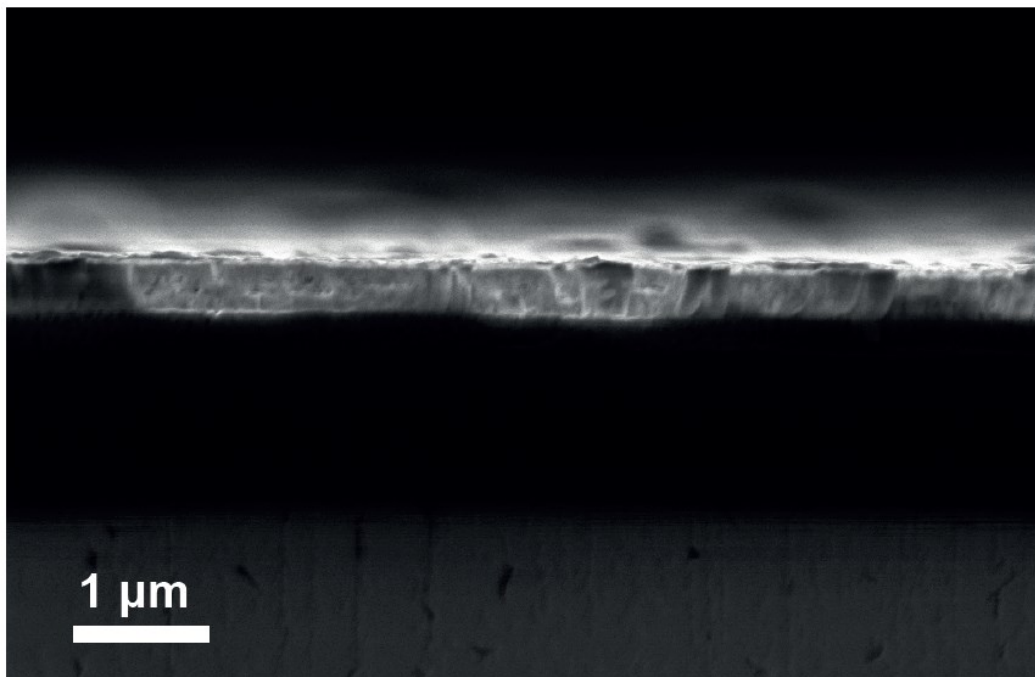
Figure S10 Cross-sectional SEM image of a thin film fabricated direct deposition as a multilayer structure at 660 °C.
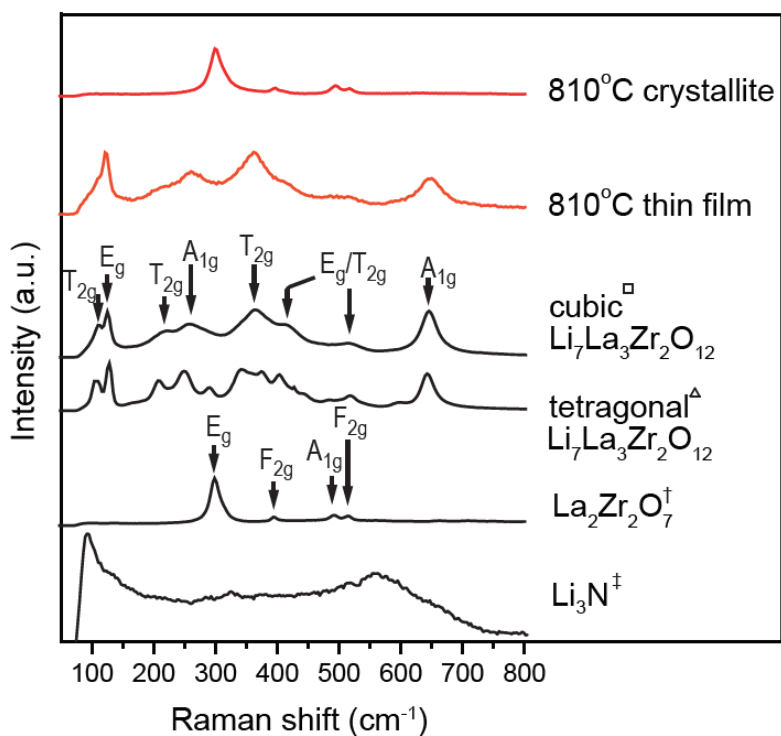
Figure S11 Ex-situ Raman crystallization study in micro-Raman spot measurements of a thin film deposited at 300 °C by PLD, followed by a post annealing at 810 °C in pure O_2. The film was measured after cooldown to room temperature. All reference data was taken from spectra obtained by Tietz et al.[230] (∆,□) and Kong et al.[253] (†) and stoichiometry and vibrational modes were assigned according to tentative assignments from literature.[230,253]. For comparison, the spectra of the Li_3N PLD target is shown (‡).
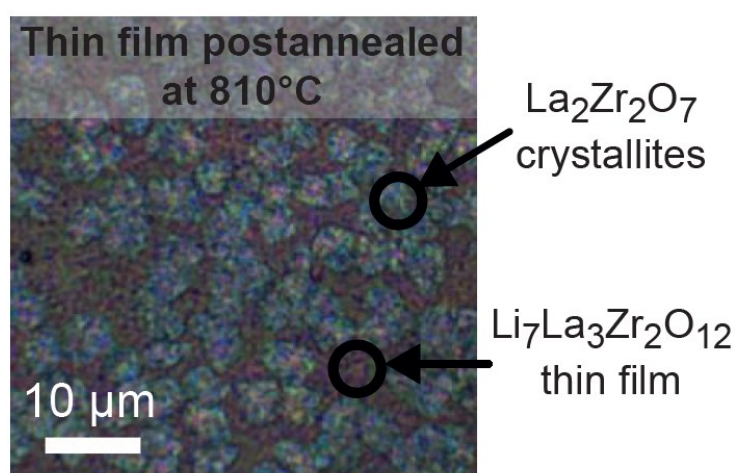
Figure S12 Optical image of the same thin film, thermally treated at 810 °C, showing the thin film of c-$Li_7La_3Zr_2O_{12}$ in coexistence with crystallite islands of the delithiated pyrochlore phase $La_2Zr_2O_7$.
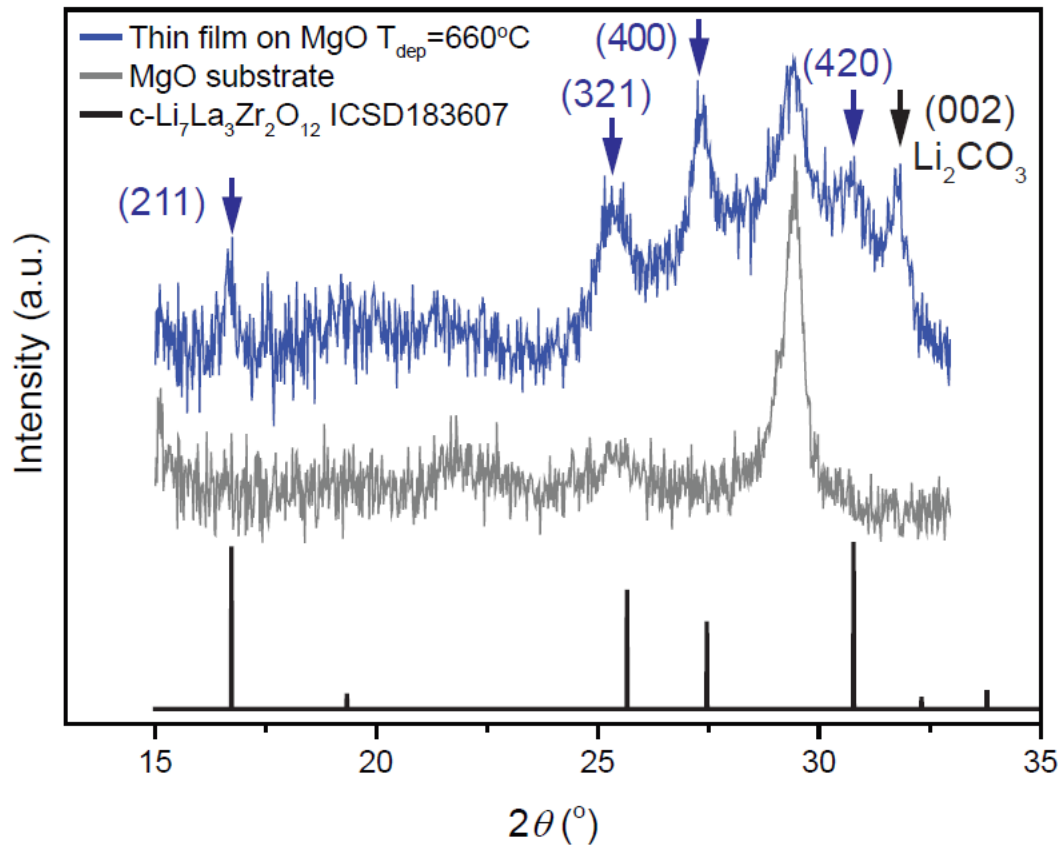
Figure S13 Thin Film XRD measurement of MgO substrate on which a cubic thin film of LLZO was deposited.

Supplementary Information Part IV
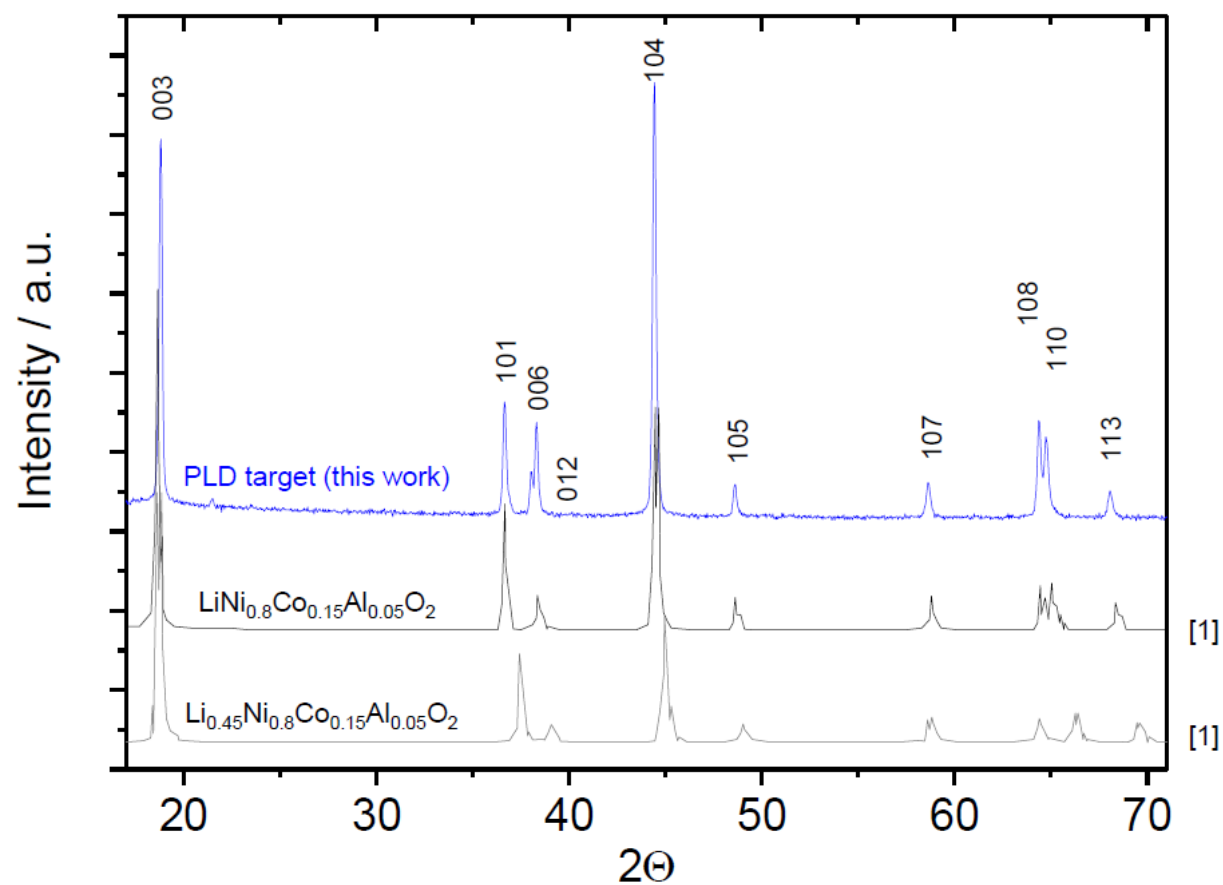
Figure S14 XRD plot of cathode target used for PLD ablation. No lithium loss observed in initial target material, if compared to literature reference (black).[312]
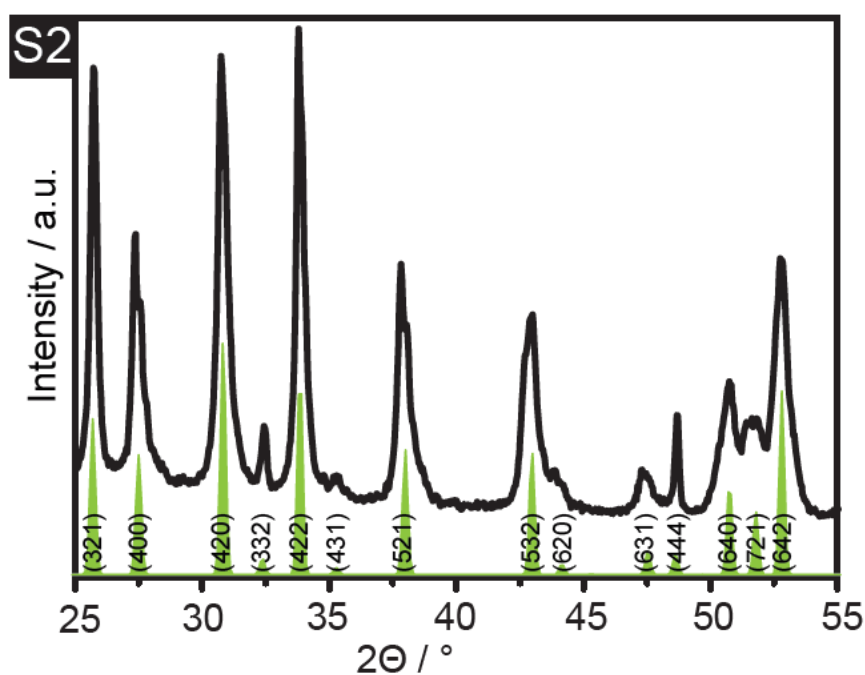
Figure S15 XRD graph of cubic Li₆.₂₅Al₀.₂₅La₃Zr₂O₁₂ electrolyte target pellet used for PLD ablation. A comparison towards ISCD185539 is shown.

Figure S16 Cross sectional image of microbattery cell grown directly on Si / Si₃N₄ substrate without bottom current collector. The immediate decomposition of the anode thin film upon exposure to ambient atmosphere induced closed porosity

List of Figures

List of Supplementary Figures

List of Tables

List of Abbreviations and Symbols

AC	alternating current
a.u.	arbitrary units
C	Rate at which a battery is discharged *or* capacity
CCEM	Competence Center for Energy and Mobility
CE	Coulombic Efficiency
CMOS	complementary metal oxide semiconductor
CPE	Impedance circuit fit element with constant phase
CV	Cyclic voltammetry
CVD	Chemical vapor deposition
D-MATL	Department of Material Science ETH Zürich
DC	Direct current *or* Dimethyl Carbonate
DME	Dimethoxyethane
E_A	Activation energy of charge transfer
EC	Ethylene Carbonate
EIS	Electrochemical impedance spectroscopy
EMC	Ethyl Methyl Carbonate
I	Current
ICSD	Inorganic crystal structures database
Inlens	Inlens SEM detector
LAGP	$Li_{1.5}Al_{0.5}Ge_{1.5}(PO_4)_3$
LATP	$Li_{1.3}Al_{0.3}Ti_{1.7}(PO_4)_3$
LCO	$LiCoO_2$
LGPS	electrolyte based on $Li_{10}GeP_2S_{12}$
LIB	Lithium ion battery
LIPON	nitrogen doped glassy Li_3PO_4
LISICON	Lithium super ionic conductor
LiTFSI	Lithium bis(trifluoromethanesulfonyl)Imide
LLTO	$Li_{0.5-3x}La_{0.5+x}TiO_3$

LLZO	$Li_7La_3Zr_2O_{12}$
LLZO:Al	Aluminum-doped $Li_7La_3Zr_2O_{12}$
c-LLZO	$Li_7La_3Zr_2O_{12}$ in cubic phase
t-LLZO	$Li_7La_3Zr_2O_{12}$ in tetragonal phase
LMN	Li_7MnN_4
LTO	$Li_4Ti_5O_{12}$
MO-CVD	Metal-organic chemical vapor deposition
MS	Magnetron sputtering
NASICON	Sodium super ionic conductor
NCA	$LiNi_{0.8}Co_{0.15}Al_{0.05}O_2$
PC	Propylene Carbonate
PEC	Poly(Ethylene Carbonate)
PLD	Pulsed laser deposition
PVD	Physical vapor deposition
Q	Impedance circuit fit element with constant phase
Raman	Raman spectroscopy
R	Impedance circuit fit element ohmic resistor
RF	Radio frequency
RT	Room temperature
SE2	Secondary electron detector
SEM	Scanning electron microscopy
SSB	solid state battery
t	Time
T	Temperature
Θ	Scattering angle
TEM	Transmission electron microscopy
UMS	Unified Measurement Software
VC	Vinylene Carbonate
XRD	X-Ray Diffraction
σ	mixed ionic/electronic conductivity
Z	complex impedance (Z' real part, Z'' imaginary part)

Bibliography

[1]   A. Volta, *Phil. Trans. R. Soc. Lond.* **1800**, *90*, 403.
[2]   *Journal of Natural Philosophy, Chemistry & the Arts*, London, **1802**.
[3]   G. Planté, *C. R. Hebd. Acad. Sci. Paris* **1855**, *40*, 554.
[4]   S. Li, Y. Dong, L. Xu, X. Xu, L. He, L. Mai, *Advanced Materials* **2014**, *26*, 3545.
[5]   D. Imamura, M. Miyayama, M. Hibino, T. Kudo, *J. Electrochem. Soc.* **2003**, *150*, A753.
[6]   M.-C. Lin, M. Gong, B. Lu, Y. Wu, D.-Y. Wang, M. Guan, M. Angell, C. Chen, J. Yang, B.-J. Hwang, H. Dai, *Nature* **2015**, *520*, 324.
[7]   B. L. Ellis, L. F. Nazar, *Current Opinion in Solid State and Materials Science* **2012**, *16*, 168.
[8]   V. Duffort, X. Sun, L. F. Nazar, *Chem. Commun.* **2016**, *52*, 12458.
[9]   D. Aurbach, Z. Lu, A. Schechter, Y. Gofer, H. Gizbar, R. Turgeman, Y. Cohen, M. Moshkovich, E. Levi, *Nature* **2000**, *407*, 724.
[10]   P. Canepa, S.-H. Bo, G. S. Gautam, B. Key, W. D. Richards, T. Shi, Y. Tian, Y. Wang, J. Li, G. Ceder, *Nature Communications* **2017**, *8*, 1759.
[11]   J. B. Goodenough, *J Solid State Electrochem* **2012**, *16*, 2019.
[12]   A. Patil, V. Patil, D. Wook Shin, J.-W. Choi, D.-S. Paik, S.-J. Yoon, *Materials Research Bulletin* **2008**, *43*, 1913.
[13]   N. Nitta, F. Wu, J. T. Lee, G. Yushin, *Materials Today* **2015**, *18*, 252.
[14]   B. Dunn, H. Kamath, J.-M. Tarascon, *Science* **2011**, *334*, 928.
[15]   K. Mizushima, P. C. Jones, P. J. Wiseman, J. B. Goodenough, *Materials Research Bulletin* **1980**, *15*, 783.
[16]   J. B. Goodenough, K.-S. Park, *J. Am. Chem. Soc.* **2013**, *135*, 1167.
[17]   Y. Li, J.-T. Han, C.-A. Wang, H. Xie, J. B. Goodenough, *Journal of Materials Chemistry* **2012**, *22*, 15357.
[18]   SPIEGEL ONLINE, Hamburg, N. Kwasniewski, "Note7-Fiasko: Samsung senkt Gewinnerwartung - SPIEGEL ONLINE - Wirtschaft," can be found under http://www.spiegel.de/wirtschaft/unternehmen/brennende-galaxy-note-7-samsung-kappt-gewinnerwartung-a-1116250.html, **n.d.**
[19]   A. Manthiram, X. Yu, S. Wang, *Nature Reviews Materials* **2017**, *2*, 16103.
[20]   N. Nitta, G. Yushin, *Particle & Particle Systems Characterization* **2014**, *31*, 317.
[21]   D. S. Jung, T. H. Hwang, S. B. Park, J. W. Choi, *Nano Lett.* **2013**, *13*, 2092.
[22]   D. Larcher, J.-M. Tarascon, *Nature Chemistry* **2015**, *7*, 19.
[23]   F. Aguesse, W. Manalastas, L. Buannic, J. M. Lopez del Amo, G. Singh, A. Llordés, J. Kilner, *ACS Appl. Mater. Interfaces* **2017**, *9*, 3808.
[24]   K. Yan, Z. Lu, H.-W. Lee, F. Xiong, P.-C. Hsu, Y. Li, J. Zhao, S. Chu, Y. Cui, *Nature Energy* **2016**, *1*, 16010.
[25]   C. Yang, K. Fu, Y. Zhang, E. Hitz, L. Hu, *Advanced Materials* **2017**, *29*, 1701169.
[26]   F. Albano, Y. S. Lin, D. Blaauw, D. M. Sylvester, K. D. Wise, A. M. Sastry, *Journal of Power Sources* **2008**, *185*, 1524.
[27]   Y. Wang, B. Liu, Q. Li, S. Cartmell, S. Ferrara, Z. D. Deng, J. Xiao, *Journal of Power Sources* **2015**, *286*, 330.
[28]   L. Porz, T. Swamy, B. W. Sheldon, D. Rettenwander, T. Frömling, H. L. Thaman, S. Berendts, R. Uecker, W. C. Carter, Y.-M. Chiang, *Advanced Energy Materials* **2017**, *7*, 1701003.
[29]   X. Yu, J. B. Bates, G. E. Jellison, F. X. Hart, *J. Electrochem. Soc.* **1997**, *144*, 524.
[30]   S. Larfaillou, D. Guy-Bouyssou, F. le Cras, S. Franger, *Journal of Power Sources* **2016**, *319*, 139.

[31] B. J. Neudecker, N. J. Dudney, J. B. Bates, *J. Electrochem. Soc.* **2000**, *147*, 517.

[32] J. B. Bates, N. J. Dudney, G. R. Gruzalski, R. A. Zuhr, A. Choudhury, C. F. Luck, J. D. Robertson, *Solid State Ionics* **1992**, *53*, 647.

[33] A. Schwöbel, R. Hausbrand, W. Jaegermann, *Solid State Ionics* **2015**, *273*, 51.

[34] C. S. Nimisha, G. M. Rao, N. Munichandraiah, G. Natarajan, D. C. Cameron, *Solid State Ionics* **2011**, *185*, 47.

[35] H. Aono, E. Sugimoto, Y. Sadaoka, N. Imanaka, G. Adachi, *J. Electrochem. Soc.* **1990**, *137*, 1023.

[36] L.-O. Hagman, P. Kierkegaard, P. Karvonen, A. I. Virtanen, J. Paasivirta, *Acta Chemica Scandinavica* **1968**, *22*, 1822.

[37] J. B. Goodenough, H. Y.-P. Hong, J. A. Kafalas, *Materials Research Bulletin* **1976**, *11*, 203.

[38] H. Y.-P. Hong, *Materials Research Bulletin* **1976**, *11*, 173.

[39] H. Aono, E. Sugimoto, Y. Sadaoka, N. Imanaka, G. Adachi, *J. Electrochem. Soc.* **1989**, *136*, 590.

[40] B. E. Francisco, C. R. Stoldt, J.-C. M'Peko, *Chem. Mater.* **2014**, *26*, 4741.

[41] B. E. Francisco, C. R. Stoldt, J.-C. M'Peko, *J. Phys. Chem. C* **2015**, *119*, 16432.

[42] A. Ahmad, T. A. Wheat, A. K. Kuriakose, J. D. Canaday, A. G. McDonald, *Solid State Ionics* **1987**, *24*, 89.

[43] T. Kida, K. Shimanoe, N. Miura, N. Yamazoe, *Sensors and Actuators B: Chemical* **2001**, *75*, 179.

[44] P. Hartmann, T. Leichtweiss, M. R. Busche, M. Schneider, M. Reich, J. Sann, P. Adelhelm, J. Janek, *The Journal of Physical Chemistry C* **2013**, *117*, 21064.

[45] H. Y.-P. Hong, *Materials Research Bulletin* **1978**, *13*, 117.

[46] P. G. Bruce, A. R. West, *Journal of Solid State Chemistry* **1982**, *44*, 354.

[47] U. v. Alpen, M. F. Bell, W. Wichelhaus, K. Y. Cheung, G. J. Dudley, *Electrochimica Acta* **1978**, *23*, 1395.

[48] P. Knauth, *Solid State Ionics* **2009**, *180*, 911.

[49] R. Kanno, M. Murayama, *J. Electrochem. Soc.* **2001**, *148*, A742.

[50] T. Kobayashi, Y. Imade, D. Shishihara, K. Homma, M. Nagao, R. Watanabe, T. Yokoi, A. Yamada, R. Kanno, T. Tatsumi, *Journal of Power Sources* **2008**, *182*, 621.

[51] M. Murayama, R. Kanno, M. Irie, S. Ito, T. Hata, N. Sonoyama, Y. Kawamoto, *Journal of Solid State Chemistry* **2002**, *168*, 140.

[52] N. Kamaya, K. Homma, Y. Yamakawa, M. Hirayama, R. Kanno, M. Yonemura, T. Kamiyama, Y. Kato, S. Hama, K. Kawamoto, A. Mitsui, *Nat Mater* **2011**, *10*, 682.

[53] F. Han, Y. Zhu, X. He, Y. Mo, C. Wang, *Advanced Energy Materials* **2016**, *6*, 1501590.

[54] S. Wenzel, S. Randau, T. Leichtweiß, D. A. Weber, J. Sann, W. G. Zeier, J. Janek, *Chem. Mater.* **2016**, *28*, 2400.

[55] K. Minami, A. Hayashi, S. Ujiie, M. Tatsumisago, *Solid State Ionics* **2011**, *192*, 122.

[56] Y. Seino, M. Nakagawa, M. Senga, H. Higuchi, K. Takada, T. Sasaki, *J. Mater. Chem. A* **2015**, *3*, 2756.

[57] H. Muramatsu, A. Hayashi, T. Ohtomo, S. Hama, M. Tatsumisago, *Solid State Ionics* **2011**, *182*, 116.

[58] S. Chen, D. Xie, G. Liu, J. P. Mwizerwa, Q. Zhang, Y. Zhao, X. Xu, X. Yao, *Energy Storage Materials* **2018**, *14*, 58.

[59] T. Ohtomo, A. Hayashi, M. Tatsumisago, Y. Tsuchida, S. Hama, K. Kawamoto, *Journal of Power Sources* **2013**, *233*, 231.

[60] W. Xu, J. Wang, F. Ding, X. Chen, E. Nasybulin, Y. Zhang, J.-G. Zhang, *Energy Environ. Sci.* **2014**, *7*, 513.

[61] Y. Inaguma, L. Chen, M. Itoh, T. Nakamura, *Solid State Ionics* **1994**, *70–71*, 196.

[62] O. Bohnke, *Solid State Ionics* **2008**, *179*, 9.

[63] F. Aguesse, V. Roddatis, J. Roqueta, P. García, D. Pergolesi, J. Santiso, J. A. Kilner, *Solid State Ionics* **2015**, *272*, 1.

[64] F. Aguesse, J. M. L. del Amo, V. Roddatis, A. Aguadero, J. A. Kilner, *Advanced Materials Interfaces* **2014**, *1*, 1300143.

[65] Y. Inaguma, C. Liquan, M. Itoh, T. Nakamura, T. Uchida, H. Ikuta, M. Wakihara, *Solid State Communications* **1993**, *86*, 689.

[66] S. Stramare, V. Thangadurai, W. Weppner, *Chem. Mater.* **2003**, *15*, 3974.

[67] V. Thangadurai, W. Weppner, *Journal of the American Ceramic Society* **2005**, *88*, 411.

[68] V. Thangadurai, W. Weppner, *Advanced Functional Materials* **2005**, *15*, 107.

[69] J. Wolfenstine, J. L. Allen, J. Read, J. Sakamoto, *Journal of Materials Science* **2013**, *48*, 5846.

[70] R. Murugan, V. Thangadurai, W. Weppner, *Angewandte Chemie International Edition* **2007**, *46*, 7778.

[71] S. Ohta, T. Kobayashi, T. Asaoka, *Journal of Power Sources* **2011**, *196*, 3342.

[72] J. L. Allen, J. Wolfenstine, E. Rangasamy, J. Sakamoto, *Journal of Power Sources* **2012**, *206*, 315.

[73] R. Wagner, G. J. Redhammer, D. Rettenwander, A. Senyshyn, W. Schmidt, M. Wilkening, G. Amthauer, *Chem Mater* **2016**, *28*, 1861.

[74] R. Wagner, G. J. Redhammer, D. Rettenwander, G. Tippelt, A. Welzl, S. Taibl, J. Fleig, A. Franz, W. Lottermoser, G. Amthauer, *Chemistry of Materials* **2016**, *28*, 5943.

[75] J. Awaka, N. Kijima, H. Hayakawa, J. Akimoto, *Journal of Solid State Chemistry* **2009**, *182*, 2046.

[76] J. Awaka, A. Takashima, K. Kataoka, N. Kijima, Y. Idemoto, J. Akimoto, *Chemistry Letters* **2011**, *40*, 60.

[77] C. A. Geiger, E. Alekseev, B. Lazic, M. Fisch, T. Armbruster, R. Langner, M. Fechtelkord, N. Kim, T. Pettke, W. Weppner, *Inorganic Chemistry* **2011**, *50*, 1089.

[78] C. Bernuy-Lopez, W. Manalastas, J. M. Lopez del Amo, A. Aguadero, F. Aguesse, J. A. Kilner, *Chemistry of Materials* **2014**, *26*, 3610.

[79] J. Wolfenstine, J. Ratchford, E. Rangasamy, J. Sakamoto, J. L. Allen, *Materials Chemistry and Physics* **2012**, *134*, 571.

[80] D. Rettenwander, G. Redhammer, F. Preishuber-Pflügl, L. Cheng, L. Miara, R. Wagner, A. Welzl, E. Suard, M. M. Doeff, M. Wilkening, J. Fleig, G. Amthauer, *Chem. Mater.* **2016**, *28*, 2384.

[81] D. Rettenwander, R. Wagner, J. Langer, M. E. Maier, M. Wilkening, G. Amthauer, *European Journal of Mineralogy* **2016**, *28*, 619.

[82] M. A. Howard, O. Clemens, K. S. Knight, P. A. Anderson, S. Hafiz, P. M. Panchmatia, P. R. Slater, *Journal of Materials Chemistry A* **2013**, *1*, 14013.

[83] A. Dumon, M. Huang, Y. Shen, C.-W. Nan, *Solid State Ionics* **2013**, *243*, 36.

[84] H. Buschmann, S. Berendts, B. Mogwitz, J. Janek, *Journal of Power Sources* **2012**, *206*, 236.

[85] M. Kotobuki, K. Kanamura, Y. Sato, T. Yoshida, *Journal of Power Sources* **2011**, *196*, 7750.

[86] L. J. Miara, S. P. Ong, Y. Mo, W. D. Richards, Y. Park, J.-M. Lee, H. S. Lee, G. Ceder, *Chemistry of Materials* **2013**, *25*, 3048.

[87] D. Rettenwander, J. Langer, W. Schmidt, C. Arrer, K. J. Harris, V. Terskikh, G. R. Goward, M. Wilkening, G. Amthauer, *Chemistry of Materials* **2015**, *27*, 3135.

[88] A. Wachter-Welzl, R. Wagner, D. Rettenwander, S. Taibl, G. Amthauer, J. Fleig, *J Electroceram* **2016**, 1.

[89] H. Buschmann, J. Dölle, S. Berendts, A. Kuhn, P. Bottke, M. Wilkening, P. Heitjans, A. Senyshyn, H. Ehrenberg, A. Lotnyk, V. Duppel, L. Kienle, J. Janek, *Physical Chemistry Chemical Physics* **2011**, *13*, 19378.

[90] B. Wang, J. B. Bates, F. X. Hart, B. C. Sales, R. A. Zuhr, J. D. Robertson, *J. Electrochem. Soc.* **1996**, *143*, 3203.

[91] J. Fu, *Solid State Ionics* **1997**, *96*, 195.

[92] J. Fu, *Solid State Ionics* **1997**, *104*, 191.

[93] S. Wenzel, D. A. Weber, T. Leichtweiss, M. R. Busche, J. Sann, J. Janek, *Solid State Ionics* **2016**, *286*, 24.

[94] T. Thompson, J. Wolfenstine, J. L. Allen, M. Johannes, A. Huq, I. N. David, J. Sakamoto, *Journal of Materials Chemistry A* **2014**, *2*, 13431.

[95] Y. Kim, A. Yoo, R. Schmidt, A. Sharafi, H. Lee, J. Wolfenstine, J. Sakamoto, *Front. Energy Res.* **2016**, *4*, DOI 10.3389/fenrg.2016.00020.

[96] P. E. Stallworth, J. J. Fontanella, M. C. Wintersgill, C. D. Scheidler, J. J. Immel, S. G. Greenbaum, A. S. Gozdz, *Journal of Power Sources* **1999**, *81–82*, 739.

[97] L. Edman, A. Ferry, M. M. Doeff, *Journal of Materials Research* **2000**, *15*, 1950.

[98] X. Huang, *J Solid State Electrochem* **2011**, *15*, 649.

[99] Y. Seino, T. Ota, K. Takada, A. Hayashi, M. Tatsumisago, *Energy & Environmental Science* **2014**, *7*, 627.

[100] J. Janek, W. G. Zeier, *Nature Energy* **2016**, *1*, 16141.

[101] W. D. Richards, L. J. Miara, Y. Wang, J. C. Kim, G. Ceder, *Chem. Mater.* **2016**, *28*, 266.

[102] Y. Zhu, X. He, Y. Mo, *ACS Applied Materials & Interfaces* **2015**, *7*, 23685.

[103] X. Han, Y. Gong, K. (Kelvin) Fu, X. He, G. T. Hitz, J. Dai, A. Pearse, B. Liu, H. Wang, G. Rubloff, Y. Mo, V. Thangadurai, E. D. Wachsman, L. Hu, *Nature Materials* **2017**, *16*, 572.

[104] W. Luo, Y. Gong, Y. Zhu, K. K. Fu, J. Dai, S. D. Lacey, C. Wang, B. Liu, X. Han, Y. Mo, E. D. Wachsman, L. Hu, *J. Am. Chem. Soc.* **2016**, *138*, 12258.

[105] T. Kato, T. Hamanaka, K. Yamamoto, T. Hirayama, F. Sagane, M. Motoyama, Y. Iriyama, *Journal of Power Sources* **2014**, *260*, 292.

[106] S. A. Delp, O. Borodin, M. Olguin, C. G. Eisner, J. L. Allen, T. R. Jow, *Electrochimica Acta* **2016**, *209*, 498.

[107] T. Okumura, S. Nishimura, *Solid State Ionics* **2014**, *267*, 68.

[108] P. . Kelly, R. . Arnell, *Vacuum* **2000**, *56*, 159.

[109] G. Bräuer, B. Szyszka, M. Vergöhl, R. Bandorf, *Vacuum* **2010**, *84*, 1354.

[110] L.-W. Zhang, M. Kobayashi, K. S. Goto, *Solid State Ionics* **1986**, *18–19*, 741.

[111] P. Puspharajah, S. Radhakrishna, A. K. Arof, *Journal of Materials Science* **1997**, *32*, 3001.

[112] K. (Kelvin) Fu, Y. Gong, B. Liu, Y. Zhu, S. Xu, Y. Yao, W. Luo, C. Wang, S. D. Lacey, J. Dai, Y. Chen, Y. Mo, E. Wachsman, L. Hu, *Sci Adv* **2017**, *3*, DOI 10.1126/sciadv.1601659.

[113] B. Liu, Y. Gong, K. Fu, X. Han, Y. Yao, G. Pastel, C. Yang, H. Xie, E. D. Wachsman, L. Hu, *ACS Appl. Mater. Interfaces* **2017**, *9*, 18809.

[114] Y. Hamon, A. Douard, F. Sabary, C. Marcel, P. Vinatier, B. Pecquenard, A. Levasseur, *Solid State Ionics* **2006**, *177*, 257.

[115] S. Zhao, Z. Fu, Q. Qin, *Thin Solid Films* **2002**, *415*, 108.

[116] Z.-W. Fu, W.-Y. Liu, C.-L. Li, Q.-Z. Qin, Y. Yao, F. Lu, *Appl. Phys. Lett.* **2003**, *83*, 5008.

[117] W.-Y. Liu, Z.-W. Fu, C.-L. Li, Q.-Z. Qin, *Electrochem. Solid-State Lett.* **2004**, *7*, J36.

[118] H. Chen, H. Tao, X. Zhao, Q. Wu, *Journal of Non-Crystalline Solids* **2011**, *357*, 3267.

[119] M. Zhang, Z. Huang, J. Cheng, O. Yamamoto, N. Imanishi, B. Chi, J. Pu, J. Li, *Journal of Alloys and Compounds* **2014**, *590*, 147.

[120] Y. Ito, A. Sakuda, T. Ohtomo, A. Hayashi, M. Tatsumisago, *Journal of the Ceramic Society of Japan* **2014**, *122*, 341.

[121] Y. Wang, Z. Liu, X. Zhu, Y. Tang, F. Huang, *Journal of Power Sources* **2013**, *224*, 225.

[122] N. Ohta, K. Takada, M. Osada, L. Zhang, T. Sasaki, M. Watanabe, *Journal of Power Sources* **2005**, *146*, 707.

[123] A. Sakuda, A. Hayashi, S. Hama, M. Tatsumisago, *Journal of the American Ceramic Society* **2010**, *93*, 765.

[124] S. Teragawa, K. Aso, K. Tadanaga, A. Hayashi, M. Tatsumisago, *Journal of Power Sources* **2014**, *248*, 939.

[125] Y. Xiong, H. Tao, J. Zhao, H. Cheng, X. Zhao, *Journal of Alloys and Compounds* **2011**, *509*, 1910.

[126] M. Rawlence, A. N. Filippin, A. Wäckerlin, T.-Y. Lin, E. Cuervo-Reyes, A. Remhof, C. Battaglia, J. L. M. Rupp, S. Buecheler, *ACS Appl. Mater. Interfaces* **2018**, DOI 10.1021/acsami.8b03163.

[127] V. Thangadurai, S. Narayanan, D. Pinzaru, *Chemical Society Reviews* **2014**, *43*, 4714.

[128] A. C. Kozen, A. J. Pearse, C.-F. Lin, M. Noked, G. W. Rubloff, *Chem. Mater.* **2015**, *27*, 5324.

[129] Q. Ling, Z. Yu, H. Xu, G. Zhu, X. Zhang, Y. Zhao, A. Yu, *Materials Letters* **2016**, *169*, 42.

[130] D. Popovici, H. Nagai, S. Fujishima, J. Akedo, *Journal of the American Ceramic Society* **2011**, *94*, 3847.

[131] X. M. Wu, S. Chen, F. R. Mai, J. H. Zhao, Z. Q. He, *Ionics* **2013**, *19*, 589.

[132] R. Inada, K. Ishida, M. Tojo, T. Okada, T. Tojo, Y. Sakurai, *Ceramics International* **2015**, *41*, 11136.

[133] S. Furusawa, H. Tabuchi, T. Sugiyama, S. Tao, J. T. S. Irvine, *Solid State Ionics* **2005**, *176*, 553.

[134] J. S. Park, L. Cheng, V. Zorba, A. Mehta, J. Cabana, G. Chen, M. M. Doeff, T. J. Richardson, J. H. Park, J.-W. Son, W.-S. Hong, *Thin Solid Films* **2015**, *576*, 55.

[135] K. Tadanaga, H. Egawa, A. Hayashi, M. Tatsumisago, J. Mosa, M. Aparicio, A. Duran, *Journal of Power Sources* **2015**, *273*, 844.

[136] I. Garbayo, M. Struzik, W. J. Bowman, R. Pfenninger, E. Stilp, J. L. M. Rupp, *Advanced Energy Materials* **2018**, *8*, 1702265.

[137] C. Loho, R. Djenadic, M. Bruns, O. Clemens, H. Hahn, *Journal of The Electrochemical Society* **2017**, *164*, A6131.

[138] A. Moradpour, O. Schneegans, S. Franger, A. Revcolevschi, R. Salot, P. Auban-Senzier, C. Pasquier, E. Svoukis, J. Giapintzakis, O. Dragos, V.-C. Ciomaga, P. Chrétien, *Advanced Materials* **2011**, *23*, 4141.

[139] J. D. Greenlee, C. F. Petersburg, W. Laws Calley, C. Jaye, D. A. Fischer, F. M. Alamgir, W. Alan Doolittle, *Appl. Phys. Lett.* **2012**, *100*, 182106.

[140] V. H. Mai, A. Moradpour, P. A. Senzier, C. Pasquier, K. Wang, M. J. Rozenberg, J. Giapintzakis, C. N. Mihailescu, C. M. Orfanidou, E. Svoukis, A. Breza, C. B. Lioutas, S. Franger, A. Revcolevschi, T. Maroutian, P. Lecoeur, P. Aubert, G. Agnus, R. Salot, P. A. Albouy, R. Weil, D. Alamarguy, K. March, F. Jomard, P. Chrétien, O. Schneegans, *Scientific Reports* **2015**, *5*, 7761.

[141] X. Zhu, C. S. Ong, X. Xu, B. Hu, J. Shang, H. Yang, S. Katlakunta, Y. Liu, X. Chen, L. Pan, J. Ding, R.-W. Li, *Scientific Reports* **2013**, *3*, 1084.

[142] J. F. M. Oudenhoven, L. Baggetto, P. H. L. Notten, *Advanced Energy Materials* **2011**, *1*, 10.

[143] V. Khomenko, E. Raymundo-Piñero, F. Béguin, *Journal of Power Sources* **2010**, *195*, 4234.

[144] Y. Kato, S. Hori, T. Saito, K. Suzuki, M. Hirayama, A. Mitsui, M. Yonemura, H. Iba, R. Kanno, *Nature Energy* **2016**, *1*, 16030.

[145] D. Choi, D. Wang, V. V. Viswanathan, I.-T. Bae, W. Wang, Z. Nie, J.-G. Zhang, G. L. Graff, J. Liu, Z. Yang, T. Duong, *Electrochemistry Communications* **2010**, *12*, 378.

[146] H.-J. Peng, J.-Q. Huang, M.-Q. Zhao, Q. Zhang, X.-B. Cheng, X.-Y. Liu, W.-Z. Qian, F. Wei, *Advanced Functional Materials* **2014**, *24*, 2772.

[147] J. B. Bates, N. J. Dudney, B. Neudecker, A. Ueda, C. D. Evans, *Solid State Ionics* **2000**, *135*, 33.

[148] J. Li, C. Ma, M. Chi, C. Liang, N. J. Dudney, *Advanced Energy Materials* **2015**, *5*, 1401408.

[149] H.-S. Kim, Y. Oh, K. H. Kang, J. H. Kim, J. Kim, C. S. Yoon, *ACS Appl. Mater. Interfaces* **2017**, *9*, 16063.

[150] S.-X. Zhao, X.-F. Fan, Y.-F. Deng, C.-W. Nan, *Electrochimica Acta* **2012**, *65*, 7.

[151] J. Z. Lee, Z. Wang, H. L. Xin, T. A. Wynn, Y. S. Meng, *J. Electrochem. Soc.* **2017**, *164*, A6268.

[152] Z. Jiang, H. Xie, S. Wang, X. Song, X. Yao, H. Wang, *Advanced Energy Materials* **2018**, *0*, 1801433.

[153] J. K. Feng, B. G. Yan, J. C. Liu, M. O. Lai, L. Li, *Materials Technology* **2013**, *28*, 276.

[154] J. Yang, B. Huang, J. Yin, X. Yao, G. Peng, J. Zhou, X. Xu, *J. Electrochem. Soc.* **2016**, *163*, A1530.

[155] S. Boulineau, J.-M. Tarascon, J.-B. Leriche, V. Viallet, *Solid State Ionics* **2013**, *242*, 45.

[156] K. Suzuki, N. Mashimo, Y. Ikeda, T. Yokoi, M. Hirayama, R. Kanno, *ACS Appl. Energy Mater.* **2018**, DOI 10.1021/acsaem.8b00227.

[157] M. Tatsumisago, A. Hayashi, *Solid State Ionics* **2012**, *225*, 342.

[158] A. Hayashi, T. Matsuyama, A. Sakuda, M. Tatsumisago, *Chemistry Letters* **2012**, *41*, 886.

[159] F. Mizuno, A. Hayashi, K. Tadanaga, T. Minami, M. Tatsumisago, *Solid State Ionics* **2004**, *175*, 699.

[160] F. Mizuno, S. Hama, A. Hayashi, K. Tadanaga, T. Minami, M. Tatsumisago, *Chemistry letters* **2002**, *31*, 1244.

[161] Y. Tao, S. Chen, D. Liu, G. Peng, X. Yao, X. Xu, *J. Electrochem. Soc.* **2016**, *163*, A96.

[162] H. Kitaura, A. Hayashi, K. Tadanaga, M. Tatsumisago, *Solid State Ionics* **2011**, *192*, 304.

[163] Y. Zhang, R. Chen, T. Liu, Y. Shen, Y. Lin, C.-W. Nan, *ACS Appl. Mater. Interfaces* **2017**, *9*, 28542.

[164] M. Kotobuki, K. Kanamura, *Ceramics International* **2013**, *39*, 6481.

[165] Y. Jin, P. J. McGinn, *Electrochimica Acta* **2013**, *89*, 407.

[166] S. Ohta, T. Kobayashi, J. Seki, T. Asaoka, *Journal of Power Sources* **2012**, *202*, 332.

[167] D. Rettenwander, A. Welzl, L. Cheng, J. Fleig, M. Musso, E. Suard, M. M. Doeff, G. J. Redhammer, G. Amthauer, *Inorg. Chem.* **2015**, *54*, 10440.

[168] S. Afyon, F. Krumeich, J. L. M. Rupp, *J. Mater. Chem. A* **2015**, *3*, 18636.

[169] J. Van den Broek, S. Afyon, J. L. M. Rupp, *Advanced Energy Materials* **2016**, *6*, 1600736.

[170] R. Murugan, S. Ramakumar, N. Janani, *Electrochemistry Communications* **2011**, *13*, 1373.

[171] D. J. Kalita, S. H. Lee, K. S. Lee, D. H. Ko, Y. S. Yoon, *Solid State Ionics* **2012**, *229*, 14.

[172] J. Nong, H. Xu, Z. Yu, G. Zhu, A. Yu, *Materials Letters* **2015**, *154*, 167.

[173] S. Lobe, C. Dellen, M. Finsterbusch, H.-G. Gehrke, D. Sebold, C.-L. Tsai, S. Uhlenbruck, O. Guillon, *Journal of Power Sources* **2016**, *307*, 684.

[174] H. Katsui, T. Goto, *Thin Solid Films* **2015**, *584*, 130.

[175] E. Kazyak, K.-H. Chen, K. N. Wood, A. L. Davis, T. Thompson, A. R. Bielinski, A. J. Sanchez, X. Wang, C. Wang, J. Sakamoto, N. P. Dasgupta, *Chem. Mater.* **2017**, *29*, 3785.

[176] R.-J. Chen, M. Huang, W.-Z. Huang, Y. Shen, Y.-H. Lin, C.-W. Nan, *Journal of Materials Chemistry A* **2014**, *2*, 13277.

[177] J. Tan, A. Tiwari, *ECS Solid State Lett.* **2012**, *1*, Q57.

[178] S. Kim, M. Hirayama, S. Taminato, R. Kanno, *Dalton Trans.* **2013**, *42*, 13112.

[179] M. Rawlence, I. Garbayo, S. Buecheler, J. L. M. Rupp, *Nanoscale* **2016**, *8*, 14746.

[180] J.-M. Tarascon, M. Armand, *Nature* **2001**, *414*, 359.

[181] E. Quartarone, P. Mustarelli, *Chem. Soc. Rev.* **2011**, *40*, 2525.

[182] B. Y. Ahn, E. B. Duoss, M. J. Motala, X. Guo, S.-I. Park, Y. Xiong, J. Yoon, R. G. Nuzzo, J. A. Rogers, J. A. Lewis, *Science* **2009**, *323*, 1590.

[183] H. Esmaeilzadeh, E. Blem, R. S. Amant, K. Sankaralingam, D. Burger, in *Computer Architecture (ISCA), 2011 38th Annual International Symposium On*, IEEE, **2011**, pp. 365–376.

[184] K. Sun, T.-S. Wei, B. Y. Ahn, J. Y. Seo, S. J. Dillon, J. A. Lewis, *Advanced Materials* **2013**, *25*, 4539.

[185] P. H. L. Notten, F. Roozeboom, R. A. H. Niessen, L. Baggetto, *Advanced Materials* **2007**, *19*, 4564.

[186] J. H. Pikul, H. Gang Zhang, J. Cho, P. V. Braun, W. P. King, *Nat Commun* **2013**, *4*, 1732.

[187] M. Baba, N. Kumagai, H. Fujita, K. Ohta, K. Nishidate, S. Komaba, B. Kaplan, H. Groult, D. Devilliers, *Journal of Power Sources* **2003**, *119–121*, 914.

[188] N. Kuwata, J. Kawamura, K. Toribami, T. Hattori, N. Sata, *Electrochemistry Communications* **2004**, *6*, 417.

[189] G. Delaizir, V. Viallet, A. Aboulaich, R. Bouchet, L. Tortet, V. Seznec, M. Morcrette, J.-M. Tarascon, P. Rozier, M. Dollé, *Adv. Funct. Mater.* **2012**, *22*, 2140.

[190] Y. Deng, C. Eames, B. Fleutot, R. David, J.-N. Chotard, E. Suard, C. Masquelier, M. S. Islam, *ACS Applied Materials & Interfaces* **2017**, *9*, 7050.

[191] J. B. Bates, N. J. Dudney, G. R. Gruzalski, R. A. Zuhr, A. Choudhury, C. F. Luck, J. D. Robertson, *Journal of power sources* **1993**, *43*, 103.

[192] G. T. Hitz, E. D. Wachsman, V. Thangadurai, *Journal of The Electrochemical Society* **2013**, *160*, A1248.

[193] W. G. Zeier, S. Zhou, B. Lopez-Bermudez, K. Page, B. C. Melot, *ACS Appl. Mater. Interfaces* **2014**, *6*, 10900.

[194] L. Cheng, J. S. Park, H. Hou, V. Zorba, G. Chen, T. Richardson, J. Cabana, R. Russo, M. Doeff, *Journal of Materials Chemistry A* **2014**, *2*, 172.

[195] S. Afyon, F. Krumeich, C. Mensing, A. Borgschulte, R. Nesper, *Scientific Reports* **2014**, *4*, 7113.

[196] X. Ji, K. T. Lee, L. F. Nazar, *Nat Mater* **2009**, *8*, 500.

[197] C. Hänsel, S. Afyon, J. L. M. Rupp, *Nanoscale* **2016**, *8*, 18412.

[198] S. Ohta, S. Komagata, J. Seki, T. Saeki, S. Morishita, T. Asaoka, *Journal of Power Sources* **2013**, *238*, 53.

[199] S. Ohta, J. Seki, Y. Yagi, Y. Kihira, T. Tani, T. Asaoka, *Journal of Power Sources* **2014**, *265*, 40.

[200] Y. Jin, P. J. McGinn, *Journal of Power Sources* **2011**, *196*, 8683.

[201] R. K. Gover, J. R. Tolchard, H. Tukamoto, T. Murai, J. T. Irvine, *Journal of the Electrochemical Society* **1999**, *146*, 4348.

[202] J. B. Goodenough, Y. Kim, *Chemistry of Materials* **2010**, *22*, 587.

[203] G. G. Amatucci, F. Badway, A. Du Pasquier, T. Zheng, *Journal of The Electrochemical Society* **2001**, *148*, A930.

[204] K. M. Colbow, J. R. Dahn, R. R. Haering, *Journal of Power Sources* **1989**, *26*, 397.

[205] S. Scharner, *Untersuchungen zur Struktur, Elektrochemie und Farbe von substituierten Lithiumtitanaten für mögliche Anwendungen in der Elektrochromie*, Shaker, Aachen, **1998**.

[206] A. Kumatani, S. Shiraki, Y. Takagi, T. Suzuki, T. Ohsawa, X. Gao, Y. Ikuhara, T. Hitosugi, *Japanese Journal of Applied Physics* **2014**, *53*, 058001.

[207] M. R. Mohammadi, D. J. Fray, *Journal of Sol-Gel Science and Technology* **2010**, *55*, 19.

[208] J. Deng, Z. Lu, I. Belharouak, K. Amine, C. Y. Chung, *Journal of Power Sources* **2009**, *193*, 816.

[209] A. Kumatani, T. Ohsawa, R. Shimizu, Y. Takagi, S. Shiraki, T. Hitosugi, *Applied Physics Letters* **2012**, *101*, 123103.

[210] D. M. Packwood, S. Shiraki, T. Hitosugi, *Phys. Rev. Lett.* **2013**, *111*, 036101.

[211] S. Ganapathy, M. Wagemaker, *ACS Nano* **2012**, *6*, 8702.

[212] M. Wagemaker, F. M. Mulder, *Acc. Chem. Res.* **2013**, *46*, 1206.

[213] Y. Shi, A. H. Bork, S. Schweiger, J. L. M. Rupp, *Nat Mater* **2015**, *14*, 721.

[214] S. Schweiger, R. Pfenninger, W. J. Bowman, U. Aschauer, J. L. M. Rupp, *Advanced Materials* **2017**, *29*, 1605049.

[215] E. Ferg, R. J. Gummow, A. De Kock, M. M. Thackeray, *Journal of the Electrochemical Society* **1994**, *141*, L147.

[216] T. Ohzuku, A. Ueda, N. Yamamoto, *J. Electrochem. Soc.* **1995**, *142*, 1431.

[217] D. C. Johnston, *Journal of Low Temperature Physics* **1976**, *25*, 145.

[218] G. Larraz, A. Orera, M. L. Sanjuán, *J. Mater. Chem. A* **2013**, *1*, 11419.

[219] R. Pfenninger, E. Sediva, S. Boyn, J. L. M. Rupp, *Unified Measurement Software UMS*, ETH Zürich, 10.3929/Ethz-b-000247100, **2017**.

[220] K. Mukai, Y. Kato, H. Nakano, *The Journal of Physical Chemistry C* **2014**, *118*, 2992.

[221] T.-F. Yi, Y. Xie, Y.-R. Zhu, R.-S. Zhu, H. Shen, *Journal of Power Sources* **2013**, *222*, 448.

[222] I. A. Leonidov, O. N. Leonidova, L. A. Perelyaeva, R. F. Samigullina, S. A. Kovyazina, M. V. Patrakeev, *Physics of the Solid State* **2003**, *45*, 2183.

[223] M. Wilkening, R. Amade, W. Iwaniak, P. Heitjans, *Phys. Chem. Chem. Phys.* **2007**, *9*, 1239.

[224] K. T. Fehr, M. Holzapfel, A. Laumann, E. Schmidbauer, *Solid State Ionics* **2010**, *181*, 1111.

[225] S. Hayashi, H. Hatano, *Journal of the Ceramic Society of Japan* **1994**, *102*, 378.

[226] H. Lindström, S. Södergren, A. Solbrand, H. Rensmo, J. Hjelm, A. Hagfeldt, S.-E. Lindquist, *J. Phys. Chem. B* **1997**, *101*, 7710.

[227] I. Kosacki, C. M. Rouleau, P. F. Becher, J. Bentley, D. H. Lowndes, *Solid State Ionics* **2005**, *176*, 1319.

[228] M. V. F. Schlupp, M. Prestat, J. Martynczuk, J. L. M. Rupp, A. Bieberle-Hütter, L. J. Gauckler, *Journal of Power Sources* **2012**, *202*, 47.

[229] L. Cheng, C. H. Wu, A. Jarry, W. Chen, Y. Ye, J. Zhu, R. Kostecki, K. Persson, J. Guo, M. Salmeron, G. Chen, M. Doeff, *ACS Appl. Mater. Interfaces* **2015**, *7*, 17649.

[230] F. Tietz, T. Wegener, M. T. Gerhards, M. Giarola, G. Mariotto, *Solid State Ionics* **2013**, *230*, 77.

[231] K. (Kelvin) Fu, Y. Gong, B. Liu, Y. Zhu, S. Xu, Y. Yao, W. Luo, C. Wang, S. D. Lacey, J. Dai, Y. Chen, Y. Mo, E. Wachsman, L. Hu, *Science Advances* **2017**, *3*, e1601659.

[232] F. Du, N. Zhao, Y. Li, C. Chen, Z. Liu, X. Guo, *Journal of Power Sources* **2015**, *300*, 24.

[233] Y. Jin, P. J. McGinn, *Journal of Power Sources* **2013**, *239*, 326.

[234] J. van den Broek, J. L. M. Rupp, S. Afyon, *J Electroceram* **2017**, *38*, 182.

[235] L. J. Miara, W. D. Richards, Y. E. Wang, G. Ceder, *Chemistry of Materials* **2015**, *27*, 4040.

[236] T. Thompson, S. Yu, L. Williams, R. D. Schmidt, R. Garcia-Mendez, J. Wolfenstine, J. L. Allen, E. Kioupakis, D. J. Siegel, J. Sakamoto, *ACS Energy Lett.* **2017**, *2*, 462.

[237] H. Yamane, M. Shibata, Y. Shimane, T. Junke, Y. Seino, S. Adams, K. Minami, A. Hayashi, M. Tatsumisago, *Solid State Ionics* **2007**, *178*, 1163.

[238] F. Mizuno, A. Hayashi, K. Tadanaga, M. Tatsumisago, *Adv. Mater.* **2005**, *17*, 918.

[239] E. Yi, W. Wang, J. Kieffer, R. M. Laine, *J. Mater. Chem. A* **2016**, *4*, 12947.

[240] K. (Kelvin) Fu, Y. Gong, G. T. Hitz, D. W. McOwen, Y. Li, S. Xu, Y. Wen, L. Zhang, C. Wang, G. Pastel, J. Dai, B. Liu, H. Xie, Y. Yao, E. D. Wachsman, L. Hu, *Energy Environ. Sci.* **2017**, *10*, 1568.

[241] I. Garbayo, M. Struzik, W. J. Bowman, R. Pfenninger, E. Stilp, J. L. M. Rupp, *Advanced Energy Materials* **2018**, *8*, 1702265.

[242] M. Bitzer, T. Van Gestel, S. Uhlenbruck, Hans-Peter-Buchkremer, *Thin Solid Films* **2016**, *615*, 128.

[243] Y. Matsuda, K. Sakamoto, M. Matsui, O. Yamamoto, Y. Takeda, N. Imanishi, *Solid State Ionics* **2015**, *277*, 23.

[244] R. Pfenninger, M. Struzik, I. Garbayo, A. Nenning, J. L. M. Rupp, *LITHIUM-CONTAINING THIN FILMS*, **2018**, 62/718,838.

[245] R. Pfenninger, M. Struzik, I. Garbayo, A. Nenning, J. L. M. Rupp, *METHODS OF FABRICATING THIN FILMS COMPRISING LITHIUM-CONTAINING MATERIALS*, **2018**, 62/718,842.

[246] L. Liu, V. E. Henrich, W. P. Ellis, I. Shindo, *Physical Review B* **1996**, *54*, 2236.

[247] S. Wu, S. S. Neo, Z. Dong, F. Boey, P. Wu, *The Journal of Physical Chemistry C* **2010**, *114*, 16706.

[248] H. El Shinawi, J. Janek, *Journal of Power Sources* **2013**, *225*, 13.

[249] D. Rettenwander, C. A. Geiger, M. Tribus, P. Tropper, G. Amthauer, *Inorganic Chemistry* **2014**, *53*, 6264.

[250] D. Rettenwander, P. Blaha, R. Laskowski, K. Schwarz, P. Bottke, M. Wilkening, C. A. Geiger, G. Amthauer, *Chemistry of Materials* **2014**, *26*, 2617.

[251] A. Wachter-Welzl, J. Kirowitz, R. Wagner, S. Smetaczek, G. C. Brunauer, M. Bonta, D. Rettenwander, S. Taibl, A. Limbeck, G. Amthauer, J. Fleig, *Solid State Ionics* **2018**, *319*, 203.

[252] H. R. Chandrasekhar, G. Bhattacharya, R. Migoni, H. Bilz, *Phys. Rev. B* **1978**, *17*, 884.

[253] L. Kong, I. Karatchevtseva, D. J. Gregg, M. G. Blackford, R. Holmes, G. Triani, *J. Am. Ceram. Soc.* **2013**, *96*, 935.

[254] H. Xie, J. A. Alonso, Y. Li, M. T. Fernández-Díaz, J. B. Goodenough, *Chem. Mater.* **2011**, *23*, 3587.

[255] M. Kubicek, A. Wachter-Welzl, D. Rettenwander, R. Wagner, S. Berendts, R. Uecker, G. Amthauer, H. Hutter, J. Fleig, *Chem. Mater.* **2017**, *29*, 7189.

[256] Y. Zhang, F. Chen, R. Tu, Q. Shen, X. Zhang, L. Zhang, *Solid State Ionics* **2016**, *284*, 53.

[257] D. O. Shin, K. Oh, K. M. Kim, K.-Y. Park, B. Lee, Y.-G. Lee, K. Kang, *Sci Rep* **2015**, *5*, DOI 10.1038/srep18053.

[258] M. Struzik, I. Garbayo, R. Pfenninger, J. L. M. Rupp, *Advanced Materials* **2018**, *(in press)*.

[259] K. Yoshima, H. Munakata, K. Kanamura, *Journal of Power Sources* **2012**, *208*, 404.

[260] C. Wang, L. Taherabadi, G. Jia, M. Madou, Y. Yeh, B. Dunn, *Electrochemical and Solid-State Letters* **2004**, *7*, A435.

[261] F. Chamran, Y. Yeh, H.-S. Min, B. Dunn, C.-J. Kim, *Journal of Microelectromechanical Systems* **2007**, *16*, 844.

[262] S. Afyon, K. V. Kravchyk, S. Wang, J. van den Broek, C. Hänsel, M. Kovalenko, J. L. M. Rupp, *in review* **2018**.

[263] T. J. Udovic, M. Matsuo, W. S. Tang, H. Wu, V. Stavila, A. V. Soloninin, R. V. Skoryunov, O. A. Babanova, A. V. Skripov, J. J. Rush, A. Unemoto, H. Takamura, S. Orimo, *Advanced Materials* **2014**, *26*, 7622.

[264] W. S. Tang, M. Matsuo, H. Wu, V. Stavila, W. Zhou, A. A. Talin, A. V. Soloninin, R. V. Skoryunov, O. A. Babanova, A. V. Skripov, A. Unemoto, S.-I. Orimo, T. J. Udovic, *Advanced Energy Materials* **2016**, *6*, 1502237.

[265] K. E. Kweon, J. B. Varley, P. Shea, N. Adelstein, P. Mehta, T. W. Heo, T. J. Udovic, V. Stavila, B. C. Wood, *Chemistry of Materials* **2017**, *29*, 9142.

[266] Y. Kihira, S. Ohta, H. Imagawa, T. Asaoka, *ECS Electrochem. Lett.* **2013**, *2*, A56.

[267] J. Wolfenstine, J. L. Allen, *Journal of Power Sources* **2008**, *180*, 582.

[268] A. Logéat, T. Köhler, U. Eisele, B. Stiaszny, A. Harzer, M. Tovar, A. Senyshyn, H. Ehrenberg, B. Kozinsky, *Solid State Ionics* **2012**, *206*, 33.

[269] Y. Li, X. Chen, A. Dolocan, Z. Cui, S. Xin, L. Xue, H. Xu, K. Park, J. B. Goodenough, *J. Am. Chem. Soc.* **2018**, *140*, 6448.

[270] R. Pfenninger, S. Afyon, I. Garbayo, M. Struzik, J. L. M. Rupp, *Advanced Functional Materials* **2018**, *28*, 1800879.

[271] E. Yi, W. Wang, J. Kieffer, R. M. Laine, *Journal of Power Sources* **2017**, *352*, 156.

[272] R. Pfenninger, M. Struzik, I. Garbayo, E. Stilp, J. L. M. Rupp, *in submission* **2018**.

[273] C. Delmas, I. Saadoune, *Solid State Ionics* **1992**, *53*, 370.

[274] C. Julien, *Solid State Ionics* **2000**, *136*, 887.

[275] S. Madhavi, G. V. Subba Rao, B. V. R. Chowdari, S. F. Y. Li, *Journal of Power Sources* **2001**, *93*, 156.

[276] T. Ohzuku, T. Yanagawa, M. Kouguchi, A. Ueda, *Journal of Power Sources* **1997**, *68*, 131.

[277] M.-S. Balogun, W. Qiu, W. Wang, P. Fang, X. Lu, Y. Tong, *J. Mater. Chem. A* **2014**, *3*, 1364.

[278] M. Nishijima, T. Kagohashi, M. Imanishi, Y. Takeda, O. Yamamoto, S. Kondo, *Solid State Ionics* **1996**, *83*, 107.

[279] M. Nishijima, N. Tadokoro, Y. Takeda, N. Imanishi, O. Yamamoto, *J. Electrochem. Soc.* **1994**, *141*, 2966.

[280] E. Panabière, N. Emery, S. Bach, J.-P. Pereira-Ramos, P. Willmann, *Corrosion Science* **2013**, *77*, 64.

[281] G. X. Wang, M. J. Lindsay, M. Ionescu, D. H. Bradhurst, S. X. Dou, H. K. Liu, *Journal of Power Sources* **2001**, *97–98*, 298.

[282] C. V. Ramana, K. Zaghib, C. M. Julien, *Journal of Vacuum Science & Technology A: Vacuum, Surfaces, and Films* **2007**, *25*, 1208.

[283] C. V. Ramana, K. Zaghib, C. M. Julien, *Applied Physics Letters* **2007**, *90*, 021916.

[284] P. J. Bouwman, B. A. Boukamp, H. J. M. Bouwmeester, P. H. L. Notten, *J. Electrochem. Soc.* **2002**, *149*, A699.

[285] T. Matsumura, N. Imanishi, A. Hirano, N. Sonoyama, Y. Takeda, *Solid State Ionics* **2008**, *179*, 2011.

[286] R. Amin, D. B. Ravnsbæk, Y.-M. Chiang, *J. Electrochem. Soc.* **2015**, *162*, A1163.

[287] N. Emery, E. Panabière, O. Crosnier, S. Bach, T. Brousse, P. Willmann, J.-P. Pereira-Ramos, *Journal of Power Sources* **2014**, *247*, 402.

[288] Y. Wang, J. Jiang, J. R. Dahn, *Electrochemistry Communications* **2007**, *9*, 2534.

[289] M. Guilmard, C. Pouillerie, L. Croguennec, C. Delmas, *Solid State Ionics* **2003**, *160*, 39.

[290] J. Lei, F. McLarnon, R. Kostecki, *The Journal of Physical Chemistry B* **2005**, *109*, 952.

[291] J. Cabana, N. Dupré, C. P. Grey, G. Subías, M. T. Caldés, A.-M. Marie, M. R. Palacín, *J. Electrochem. Soc.* **2005**, *152*, A2246.

[292] J. Cabana, C. M. Ionica-Bousquet, C. P. Grey, M. R. Palacín, *Electrochemistry Communications* **2010**, *12*, 315.

[293] E. Panabière, N. Emery, S. Bach, J.-P. Pereira-Ramos, P. Willmann, *Journal of Alloys and Compounds* **2016**, *663*, 624.

[294] A. M. Gaikwad, G. L. Whiting, D. A. Steingart, A. C. Arias, *Adv. Mater.* **2011**, *23*, 3251.

[295] W. Lai, C. K. Erdonmez, T. F. Marinis, C. K. Bjune, N. J. Dudney, F. Xu, R. Wartena, Y.-M. Chiang, *Adv. Mater.* **2010**, *22*, E139.

[296] M. Nathan, D. Golodnitsky, V. Yufit, E. Strauss, T. Ripenbein, I. Shechtman, S. Menkin, E. Peled, *Journal of Microelectromechanical Systems* **2005**, *14*, 879.

[297] H. Ning, J. H. Pikul, R. Zhang, X. Li, S. Xu, J. Wang, J. A. Rogers, W. P. King, P. V. Braun, *PNAS* **2015**, *112*, 6573.

[298] M. Nishizawa, K. Mukai, S. Kuwabata, C. R. Martin, H. Yoneyama, *J. Electrochem. Soc.* **1997**, *144*, 1923.

[299] H.-S. Min, B. Y. Park, L. Taherabadi, C. Wang, Y. Yeh, R. Zaouk, M. J. Madou, B. Dunn, *Journal of Power Sources* **2008**, *178*, 795.

[300] H. Kim, *Journal of Laser Micro/Nanoengineering* **2012**, *7*, 320.

[301] N/A, "Datasheet Biologic SP-150," can be found under http://www.bio-logic.net/wp-content/uploads/20130710-sp50.pdf, **2018**.

[302] N/A, "Datasheet Arbin BT2000," can be found under https://enelec.com/images/PDF/bt2000.pdf, **2018**.

[303] N/A, "Datasheet Arbin BT2000-2X43," can be found under http://www.autolabj.com/construction.files/option.files/Arbin/BT-2X43_rev5.pdf, **2018**.

[304] N/A, "Datasheet Macor 4000 series," can be found under http://www.maccor.com/Products/Series4000.aspx, **2018**.

[305] N/A, "Datasheet Macor 4000 System," can be found under http://www.maccor.com/ProductDocs/Data%20Sheet%20for%20Series%204000%20Test%20System.pdf, **2018**.

[306] N/A, "Datasheet Astrol BATT-SMALL," can be found under http://www.astrol.ch/en/Battery-Cyclers/BAT-SMALL.htm, **2018**.

[307] N/A, "Datasheet Keithley 2612," can be found under http://www.testequipmenthq.com/datasheets/KEITHLEY-2612-Datasheet.pdf, **2018**.

[308] A. J. Smith, J. C. Burns, S. Trussler, J. R. Dahn, *Journal of The Electrochemical Society* **2010**, *157*, A196.

[309] A. J. Smith, J. C. Burns, J. R. Dahn, *Electrochem. Solid-State Lett.* **2010**, *13*, A177.

[310] A. J. Smith, J. C. Burns, D. Xiong, J. R. Dahn, *J. Electrochem. Soc.* **2011**, *158*, A1136.

[311] J. Wold, J. Marcicki, A. Masias, *J. Electrochem. Soc.* **2017**, *164*, A2131.

[312] I. Belharouak, W. Lu, D. Vissers, K. Amine, *Electrochemistry Communications* **2006**, *8*, 329.

Curriculum Vitae

__Personal information__

First name / Surname	Reto Pfenninger
Address	Hausmattrain 7 4600 Olten Switzerland
Mobile	+41 79 720 71 03
E-mail	reto.pfenninger@mat.ethz.ch
Nationality	Swiss
Date and place of birth	14th of February 1989, Olten (Canton of Solothurn)
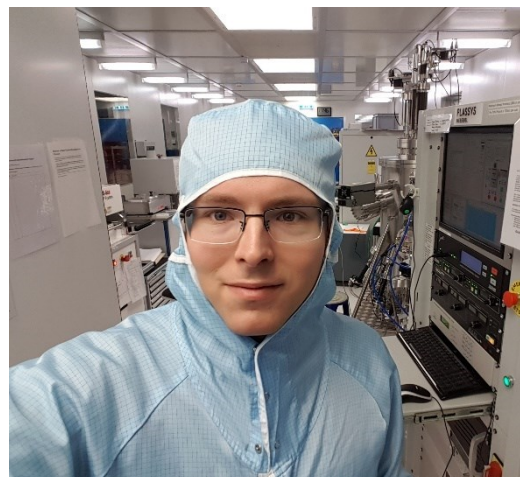
__Education and training__

September 2018	PhD defense at Swiss Federal Institute of Technology (ETH)
April 2017	PhD program continuation on All Solid State Li-ion Batteries at Massachusetts Institute of Technology (MIT) USA in the group of Prof. Jennifer Rupp
July 2014	PhD program on All Solid State Li-ion Batteries at Swiss Federal Institute of Technology (ETH) in the group of Prof. Jennifer Rupp
Since November 2011	Masters Program Material Science (D-MATL) at Swiss Federal Institute of Technology (ETH)
September 2008 - **November 2011**	Bachelors Program Material Science (D-MATL) at Swiss Federal Institute of Technology (ETH)
2007 - 2008	Student at ETH in the Department of Physics
2007	High School Degree with Main Focus on Physics and Mathematics, Kantonsschule Olten
2000 – 2003	Progymnasium Kantonsschule Olten
1995 – 2000	Elementary school | Olten

Work experience

August 2011 - October 2011	Internship at Stryker Company, Selzach Biomechanics Laboratory Assistant

Awards

Hans-Eggenberger Prize 2015 for Interdisciplinary Electronic Engineering for master thesis

"Top 20 invention" of *Spark Award 2019, ETH Zürich*

Project Management

2016 - 2018	Head Project Manager of CCEM Consortium SLIB (No. 911) "Solid State Lithium ion Batteries" Largest "All Solid State Battery" Consortium in Switzerland

Teaching

Supervision of Bachelor thesis:

- Andrew Angern (Student at department of material science D-MATL, ETH Zürich)
- Jonas Freitag (Student at department of material science D-MATL, ETH Zürich)

Supervision of Master thesis:

- Tibor Alec (Low Cost Processing and Deposition Methods for Solid State Battery Electrolytes)
- Teo Jun Hao (Cathode Synthesis Routes for Solid State Batteries)

Military

Member of the ABC Defence Forces in Swiss Military

ABC Abw Ei Kp

Computer knowledge

C, C++, Matlab, Python, Java, PHP, SQL, Labview

2009 - present	Maintainer and Software Architect of the "Platform für Lungenmedizin Schweiz"
2007 - present	Head Developer and Project Maintainer of "Unified Measurement Software UMS" for Lab-Automation

List of Publications

1. **A Low Ride on Processing Temperature for a Fast Li Conduction in Garnet Solid State Battery Films**
Pfenninger R., Struzik M., Garbayo I., Stilp E., Rupp J.L.M.
In press, Nature Energy (2019)

2. **Epitaxial thin films as a model system for Li-ion conductivity in $Li_4Ti_5O_{12}$**
Pagani F., Stilp E., Pfenninger R., Reyes E.C., Remhof A., Balogh-Michels Z., Neels A., Sastre Pellicer J., Stiefel M., Döbeli M., Rossell M.D., Erni R., Rupp J.L.M. and Battaglia C.
In press, ACS Applied Materials & Interfaces (2018)

3. **Simple and Efficient Carbon Dioxide Sensing of $Li_7La_3Zr_2O_{12}$ for Environmental Monitoring**
Struzik M., Garbayo I., Pfenninger R., Rupp J.L.M.
Advanced Materials 30, 1804098 (2018)

4. **Lithium Titanate Anode Thin Films for Li-Ion Solid State Battery Based on Garnets**
Pfenninger R., Afyon S., Garbayo I., Struzik M., Rupp J.L.M.
Advanced Functional Materials, 1800879 (2018)

5. **Unified Measurement Software UMS**
Pfenninger R., Sediva E., Boyn S., Rupp J.L.M.
Software publication (2017) DOI: 10.3929/ethz-b-000247100

6. **Glass-Type Polyamorphism in Li-Garnet Thin Film Solid State Battery Conductors**
Garbayo I., Struzik M., Bowman W., Pfenninger R., Stilp E., Rupp J.L.M.
Advanced Energy Materials, 1702265 (2017)

7. **Interfacial Strain Mapping and Chemical Analysis of Strained-Interface Heterostructures by Nanodiffraction and Electron Energy-Loss Spectroscopy**
Bowman W., Schweiger S., Pfenninger R., Izadi E., Darbal A., *Rupp J.L.M.*, Crozier P.A.
Microscopy and Microanalysis 23 (S1), 1776-1777 (2017)

8. **Designing Strained Interface Heterostructures for Memristive Devices**
Schweiger S., Pfenninger R., Bowman W.J, Aschauer U., Rupp J.L.M. **Advanced Materials, 1605049 (2017)**

9. **Strain controlled oxygen vacancy formation and ordering in $CaMnO_3$**
Aschauer U., Pfenninger R., Selbach S., Grande T., Spaldin N.A.
Physical Review B 88, 054111 (2013)

Patents

METHOD OF FABRICATING THIN FILMS COMPRISING LITHIUM-CONTAINING MATERIALS (US 62/718,842)
Owner: ETH Zurich / MIT
Inventors: <u>Pfenninger R.</u>, Struzik M., Garbayo I., Nenning A., Rupp J.L.M.
Pending (2018)

LITHIUM-CONTAINING THIN FILMS (US 62/718,838)
Owner: ETH Zurich / MIT
Inventors: <u>Pfenninger R.</u>, Struzik M., Garbayo I., Nenning A., Rupp J.L.M.
Pending (2018)

Memberships

Member of Swiss Engineering STV

Akademisches Orchester Zürich (AOZ)

Active Membership Camerata Aksademica Aarau

Active Membership Amateurfunkverein Basel HB9BSL

Active Membership Union Schweizer Kurzwellen-Amateure

Passive Membership Eislaufclub Olten

Member of the Advisory Board Lungenliga Solothurn

Personal skills and competences

Mother tongue | German

Other language(s) | English (fluently), Italian (basic knowledge), French (basic knowledge)

Conference Contributions

The following list of conference contributions is shown in inverse chronological order. The author of this thesis is highlighted in <u>underline</u> markup.

Posters:

- <u>R. Pfenninger</u>, S. Afyon, I. Garbayo, M. Struzik, J.L.M. Rupp, *Lithium Titanate Anode Thin Films for Li-Ion Solid State Battery based on Garnets*
  MRS Fall Meeting 2017, Boston, MA, USA, 11/2017

- <u>R. Pfenninger</u>, S. Afyon, I. Garbayo, M. Struzik, JLM Rupp, *" Novel Li-Titanate Anode Thin Film Structures for Li-Garnet All Solid State Batteries"*,
  IMLB Chicago, IL, USA 08/2016

- S. Afyon, I. Garbayo, <u>R. Pfenninger</u>, M. Rawlence, M. Struzik, J.L.M. Rupp *"All Solid State Li-Garnet-based Batteries: From Materials Development to Thin Film Microstructures"*
  SSI-20, Keystone, CO, USA, 06/2015

- J.L.M. Rupp, S. Afyon, I. Garbayo, M. Struzik, M. Rawlence, <u>R. Pfenninger</u>, *„ All Solid State Li-Garnet-based Batteries: From Materials Development to Thin Film Microstructures"*
  Solid State Ionics 20, Keystone, CO, USA, 06/2015

Oral Presentations:

- M. Struzik, <u>R. Pfenninger</u>, J.L.M. Rupp, "CO_2 sensing of Li-garnets", ISSFIT-13, Minsk, Belarus, 07/2018

- <u>R. Pfenninger</u>, M. Struzik, I. Garbayo, J.L.M Rupp, "*An All Solid State Thin Film Li-Garnet Microbattery: Composed of Li_7MnN_4 Anode, $LiNi_{0.8}Co_{0.15}Al_{0.05}O_2$ Cathode and $Li_{6.25}Al_{0.25}La_3Zr_2O_{12}$ Electrolyte Films*"
  MRS Fall Meeting 2017, Boston, USA, 11/2017

- M. Struzik, <u>R. Pfenninger</u>, A. Nenning, J.L.M. Rupp, *"Li-Garnet Based Potentiometric Sensors for CO_2 Concentration Monitoring"*,
  21st International Conference on Solid State Ionics, Padua, Italy, 06/2017

- M. Struzik, <u>R. Pfenninger</u>, I. Garbayo, S. Afyon, J. L. M. Rupp, *"All Solid State Li-Ion Batteries Based on Li-Garnet Electrolyte"*
  21st International Conference on Solid State Ionics, Padua, Italy, 06/2017

- <u>R. Pfenninger</u>, S. Afyon, M. Struzik, I. Garbayo, J.L.M Rupp, *"Solid State Lithium Thin Film Battery Composed of $Li_4Ti_5O_{12}$ Anodes with a Solid Garnet $Li_{6.25}Al_{0.25}La_3Zr_2O_{12}$ Electrolyte"*
  21st International Conference on Solid State Ionics, Padua, Italy, 06/2017

- I. Garbayo, M. Struzik, W.J. Bowman, <u>R. Pfenninger</u>, E. Stilp, J.L.M. Rupp, *"Li Transfer in Amorphous to Crystalline $Li_7La_3Zr_2O_{12}$ Garnet Thin Films for All-Solid-State Battery Electrolytes"*,
  21st International Conference on Solid State Ionics, Padua, Italy, 06/2017

- <u>R. Pfenninger</u>, M. Struzik, I. Garbayo, J.L.M Rupp, "*An All Solid State Thin Film Li-Garnet Microbattery: Composed of Li_7MnN_4 Anode, $LiNi_{0.8}Co_{0.15}Al_{0.05}O_2$ Cathode and $Li_{6.25}Al_{0.25}La_3Zr_2O_{12}$ Electrolyte Films*",
  21st International Conference on Solid State Ionics, Padua, Italy, 06/2017

- M. Struzik, I. Garbayo, <u>R. Pfenninger</u>, S. Afyon, M. Rawlence, J. L. M. Rupp, *"All-Solid State Li-Garnet Materials and Devices"*
  67th Annual Meeting of the International Society of Electrochemistry, Den Haag, Netherlands, 08/2016

- I. Garbayo, <u>R. Pfenninger</u>, M. Struzik, S. Afyon, M. Rawlence, J.L.M. Rupp *"Materials Development for All Solid State μBatteries: Towards a Thin Film Li-Garnet-based Battery"*
  EMN Meeting on Batteries, Orlando, FL, USA, 02/2016

- I. Garbayo, M. Struzik, <u>R. Pfenninger</u>, J.L.M. Rupp *"All Solid State Li-ion Batteries based on Cubic Garnets: From Bulk Materials to Thin Film Battery Structures"*
  ECS Conference on Electrochemical Energy Conversion & Storage with SOFC-XIV, Glasgow, Scotland, 07/2015

- M. Struzik, I. Garbayo, <u>R. Pfenninger</u>, J.L.M. Rupp *„ All Solid State Li$^+$ Microbatteries: Doping Strategies to Profit on High Li-Diffusivities"*
  Solid State Ionics 20, Keystone, CO, USA, 06/2015

- J.L.M. Rupp, S. Afyon, <u>R. Pfenninger</u>, M. Struzik *„ Materials Development for All Solid State Li-Garnet-based Batteries"*
  EMRS Spring Meeting, Lille, France, 05/2015

- J.L.M. Rupp, S. Afyon, I. Garbayo, <u>R. Pfenninger</u>, M. Rawlence, M. Struzik *"Materials Development for All Solid State Li-Garnet-based Batteries"*
  Bunsen Colloquium 2014, Frankfurt, Germany, 11/2014

Financial Support